This is to certify that the

thesis entitled

COLLOIDAL OPTIMIZATION OF FREEZE-DRIED SiC$_w$ REINFORCED Si$_3$N$_4$ CERAMIC COMPOSITES

presented by

Patrick R. Sneary

has been accepted towards fulfillment
of the requirements for

Masters degree in Materials Science

Melissa

Major professor

Date August 19, 1996

COLLOIDAL OPTIMIZATION OF FREEZE-DRIED SIC$_W$ REINFORCED SI$_3$N$_4$ CERAMIC COMPOSITES

By

Patrick R. Sneary

A THESIS

Submitted to
Michigan State University
in partial fulfillment of the requirements
for the degree of

MASTER OF SCIENCE

Department of Materials Science and Mechanics

1996

ABSTRACT

COLLOIDAL OPTIMIZATION OF FREEZE DRIED SiC_w REINFORCED SI_3N_4 CERAMIC COMPOSITES

by

Patrick R. Sneary

Si_3N_4 is a candidate for many advanced structural engineering applications because of its excellent thermal and wear properties, however, application of Si_3N_4 is limited due to its low fracture toughness. Because the fracture toughness of ceramic materials is highly dependent upon initial flaw sizes, improvement of the fracture toughness of ceramics must begin with green processing. Inefficient packing of powders within a green ceramic compact can lead to an inhomogeneous pore structure making it very difficult to sinter to full density without hot pressing or hot isostatic pressing (HIPing). Optimizing processing of Si_3N_4 components, as well as the addition of a toughening phase such as SiC whiskers, has been shown to improve the fracture toughness of Si_3N_4. This study examines the effect of colloidal optimization on freeze-dried Si_3N_4 monolithic and composite powders consolidated by pressureless sintering. Results are given as a function of SiC_w loading and processing pH.

ACKNOWLEDGMENTS

I would like to thank my advisor Dr. Melissa Crimp, colleague Zhengmao Yeh and the countless number of great friends I have made while at Michigan State. Your patience with me and confidence in me made this thesis possible, and your friendship allowed me to keep my sanity. A special thanks to my parents whose love and support gives me the strength to accomplish anything.

TABLE OF CONTENTS

LIST OF TABLES

LIST OF FIGURES

INTRODUCTION

Dry pressing of ceramic powders remains a popular method for consolidating green bodies for sintering. However, dry processing methods are often ineffective for producing ceramic composites. Dry milling of ceramic components provides limited homogeneity by physically breaking apart agglomerates and mixing of components. Silicon carbide whiskers (SiC_w) are a popular addition to toughen monolithic ceramics, however, dry-milling to achieve adequate homogeneity often results in excessive whisker damage eliminating their toughening effect. Homogeneity can be achieved by mixing composite components in colloidal suspension and adjusting suspension conditions to provide optimum dispersion. Whiskers can then be added to the ceramic matrix in as-received form without sustaining damage. Ball-milling can still be employed to reduce SiC_w aspect ratios to examine the effect of decreasing whisker aspect ratio on density and fracture toughness, but ball-milling is not relied upon for composite homogeneity.

Dispersed composite suspensions are subsequently freeze-dried to remove to remove the supernatant leaving behind a dry composite powder suitable for pressing. The improved homogeneity provided by colloidal processing is especially important for pressureless sintering of SiC_w-Si_3N_4 composites. Pressureless sintering of monolithic Si_3N_4

to assist in porosity removal. In addition, the added pressure supplied by these techniques suppresses the decomposition reaction and allows higher temperatures to be used to increase densification. However, these techniques are expensive and do not lend themselves well to large scale production like pressureless sintering. The purpose of this study is to determine whether colloidal optimization of freeze-dried suspensions provide adequate homogeneity of components to allow full densification by pressureless sintering. A survey of literature indicates nearly all SiC_w-Si_3N_4 composites are produced by hot pressing, and few attempts have been made to produce these composites by pressureless sintering.

REVIEW OF LITERATURE

In general, a colloid is defined by particles in a suspension with a linear dimension between 10^{-3} and $1\mu m$ [1]. Smaller particles would be indistinguishable from solution, and larger particles, common to ceramic processing, would be more highly influenced by gravitational forces. Most of the research in colloidal theory involves examining how small particles of one material are distributed throughout a medium, and whether these particles remain discrete, or agglomerate. Ideas involving surface chemistry and interfacial energies are significant to colloids because of the increased surface area of dispersed particles within the suspension. This dependence on surface area is shown by the classification of colloids as either lyophobic (solvent hating), or lyophilic (solvent loving), or hydrophobic and hydrophilic when referring to aqueous suspensions. Unfortunately, these distinctions define only extremes, and there are many intermediate states. Hydrophilic colloids are thermodynamically stable, meaning there is a strong interaction between the medium and the particle surface. The interactions are strong enough to break-up the dispersed phase causing an entropy increase. Hydrophobic colloids are never thermodynamically stable, therefore, the kinetics of coagulation is extremely important. Some may have a highly reactive surface, but because only a small number of surface atoms can interact with the medium (low wetabililty), there is an increase in Gibb's free energy. Therefore, lyophobic colloids can remain stable only if there are strong repulsive forces to keep individual particles from agglomerating. Consequently, they are always thermodynamically unstable and their stability, relative to ceramic processing times, is purely kinetic. Study of hydrophobic colloids is most pertinent to ceramic processing. Lyophillic colloids are affected by the same forces, but also by strong effects specific to the solvent (medium) which can be difficult to predict. Therefore, we will discuss the behavior of lyophobic colloids and how their behavior can effect ceramic processing. Issues significant to processing include, particle size, flocculation (agglomeration), interparticle forces and stability, as well as estimation of parameters needed to classify and predict stability of composite ceramic colloids. Because of the "cloudy" nature of colloids, the effects of aqueous dispersant on the surface of Si_3N_4 (hydrophilic interactions) should be examined for greater understanding of a system which is not entirely hydrophobic

COLLOIDAL FORCES

There are attractive, repulsive, and steric forces which can act on particles in a colloidal suspension. Steric forces are generated by the physical interaction of adsorbed co-polymers on the surface of the suspended particles.

Because lyophobic particles are thermodynamically unstable, their stability relies on mechanisms that prevent flocculation during collisions with other particles induced by brownian motion. This can be accomplished if suspension particles have same sign electric charges which create a repulsive force, or by adsorbed polymer chains that physically prevent close approach. Steric interactions, however, will not be evaluated because we will be considering systems without additions of surfactants and dispersants. Charges accumulate at the solid liquid interface of colloidal particles upon dispersion with each phase taking on an opposite sign. The sources of these charges are referred to as potential determining ions. For ionic materials, the source of ions is obvious (generally unequal ionic dissolution in suspension medium), but the sources within other materials can be more obscure, usually involving ionization of particle surface groups or adsorption of ions from electrolyte suspension. For aqueous suspensions, H^+ and OH^- are often potential determining ions and the interparticle potential can be controlled by changing the suspension pH [1]. These charges impart an electrical potential on the particles which attracts counter ions from the medium. Some counter ions become bound to the particle surface while others remain only loosely associated with the particle due to thermal motion. This association creates a diffuse electrical double layer around the particle which represents the gradual reduction of potential around the particle. As electrolyte concentration increases (source of counter ions, which ideally do not react with the particles surface and, therefore, have no effect on determining surface potential), the number of available counter ions increases and the double layer becomes more compact, i.e.: repulsive interactions between particles become smaller (potential drops more quickly). Therefore, particles must approach closer for interactions to occur and attractive van der Waals forces become greater at smaller separation distances.

Stability can be viewed in a macroscopic or microscopic manner. The latter involves individual collisions between particles and examining the forces involved to determine whether a collision will result in flocculation. One in every 10^{10} collisions may be considered kinetically stable. Microscopic stability will be examined more closely later, however, it is known macroscopically, that flocculation can result from changes in pH or electrolyte concentration [1].

Colloidal stability is dependent upon the strength of the surface charge (determined by potential determining ions) and the size of the double layer (determined by counter ions). Therefore, even if the surface potential is high, flocculation can still occur if the extent of the double layer is reduced by electrolyte addition. A point of rapid coagulation can be isolated where the addition of electrolyte causes nearly every collision to result in flocculation. This is referred to as the critical coagulation concentration (c.c.c.). The c.c.c. is easy to determine experimentally and is more dependent upon counter ion valency than electrolyte concentration itself [1]. This is referred to as the Schultz-Hardy rule which shows the sensitivity of lyophobic colloids to electrolyte concentration, the rationale for which is called DLVO theory (named after the pioneers in colloidal study Deryaguin, Landau, Verwey, and Overbeek). DLVO theory explains why particles tend to flocculate unless kinetic effects are retarded. The kinetics of flocculation depend on the frequency and energy of particle encounters and whether the thermal energy is great enough to overcome the potential barrier between particles. This balance of attractive and repulsive forces is measured in terms of a potential energy barrier as developed by DLVO theory for the prediction of colloidal stability. To compute the magnitude of the potential energy barrier, formulations for attractive and repulsive forces between particles must first be examined.

Attractive Forces

van der Waals forces are the dominant attractive forces between particles in suspension and can be divided into 3 distinct types of attraction London, Debye, or Keesom. These forces involve the attraction of single molecules, however, it is assumed that colloidal particles can be treated in the same yet additive manner [1]. The potential energy of this attraction can be written as $\Phi = \varepsilon x^{-12} - \beta x^{-6}$, where x is the separation distance, ε represents the repulsion due to the close approach of atoms, and β represents the type of attraction. The potential energy of attraction is always negative. van der Waals attraction arises from the interactions of dipoles within an electric field produced by either a permanent or induced dipole from another particle. London forces are the result of the interaction of mutually induced dipoles and are the dominant attractive force between particles in suspension unless the particles are highly polar. While van der Waals forces are usually considered between single molecules, colloidal particles are treated in an additive manner (cluster of molecules) resulting in long range (tens of nanometers) attraction. Hamaker [2] developed a relation for the attractive forces without retardation between dissimilar spherical colloidal particles with radii a_i and a_j, where H is the separation distance.

$$V_a = -\frac{A}{12}\left[\frac{y}{x^2+xy+x} + \frac{y}{x^2+xy+x+y} + 2\log\frac{x^2+xy+x}{x^2+xy+x+y} \right] \qquad (1)$$

A= Hamaker constant

$x = H/(a_1+a_2)$

$y = a_1/a_2$

The Hamaker constant can be difficult to calculate because it contains many parameters that are hard to find or measure for materials of interest, however, substituting general values of components, the Hamaker constant can be shown to have values around 10^{-13}-10^{-12}ergs [1]. Lifshitz [3] developed a method for determining the Hamaker constant of materials in a vacuum using macroscopic properties such as the dielectric constant or the refractive index. This relation was further simplified by Bleier [4] to

$$A_i(kT) \approx 113.7 \frac{(\varepsilon_i - 1)^2}{(\varepsilon_i + 1)^{\frac{3}{2}}(\varepsilon_i + 2)^{\frac{1}{2}}} \tag{2}$$

where ε is the material dielectric constant. The effective Hamaker constant between particles in suspension is lessened by the fact that particles will attract molecules of the medium located between them. The effective Hamaker constant can be computed knowing the Hamaker constant of the medium by the following formulation [1].

$$A_{eff} = (A_i^{1/2} - A_m^{1/2})(A_j^{1/2} - A_m^{1/2}) \tag{3}$$

Therefore, the dispersion medium has a positive effect on colloidal stability by reducing van der Waals forces responsible for flocculation. In addition, electrostatic forces between particles can create a repulsive force strong enough to prevent flocculation by van der Waals forces.

Repulsive Forces

Repulsive forces between particles are the result of an electrochemical double layer which defines the interface between isolated colloidal particles and the suspension medium. The distribution of charge surrounding a colloidal particle is the result of two different types of ions, potential determining ions (p.d.i.) and indifferent ions. P.d.i.s can adsorb to the surface of particles and affect surface charge while indifferent ions have no effect on particle potential. However, indifferent ions (supplied by the electrolyte) of opposite charge can be found in higher concentration around the charged particle, thus balancing the charge by surrounding the particle. This 'sea' of charges surrounding the particle, as well as the adsorbed p.d.i.s form the double layer. Particle charge can be manipulated by the addition of p.d.is from a common source, such as the addition of HNO_3 and KOH resulting in H^+ and OH^- ions and KNO_3 electrolyte. The charge density and potential drop at the interface of a colloidal particle and the medium can be described by their dependence upon the concentration of ions, their valence, and their specific tendencies to adsorb. Therefore, it must be understood how the potential or density of charge carriers changes as a function of distance from the particle. This was first modeled by Guoy and Chapman as a diffuse double layer [1].

Diffuse Double Layer

Simplifying assumptions must be made in order to mathematically model the diffuse double layer. Ions are treated as point charges in a Boltzmann distribution, therefore, charged particle surfaces are large relative to the ions and can be assumed to be flat. Further simplifications include a uniform dielectric constant throughout a medium containing a single symmetrical electrolyte of charge z. Allowing ψ_0 to equal the potential at the particle surface, and ψ being the potential as a function of distance (x), the number of + and - ions per unit volume can be determined at points where the potential is ψ.

$$n_+ = n_o \exp\left(\frac{-ze\Psi}{kT}\right) \quad \text{and} \quad n_- = n_o \exp\left(\frac{ze\Psi}{kT}\right) \tag{4}$$

n_o= bulk ionic concentration

z = ion charge number
e = electron charge
k = Boltzmann constant
T = temperature

The charge density (ρ) is then defined as $\rho = ze(n_{+}-n_{-})$. Charge density and potential are related by the Poisson equation [5] yielding the following differential equation.

$$\frac{d^2\Psi}{dx^2} = \frac{2zen_o}{\varepsilon}\sinh\frac{ze\Psi}{kT} \tag{5}$$

This can be solved for the following boundary conditions to yield an expression for ψ.

Boundary Conditions include: $\psi=\psi_o$
$x=0$
$\psi=0$ and $d\psi/dx=0$ at $x=\infty$

$$\Psi = \frac{2kT}{ze}\ln\left[\frac{1+\gamma\exp(-\kappa x)}{1-\gamma\exp(-\kappa x)}\right] \tag{6}$$

where

$$\gamma = \frac{\exp(ze\Psi/2kT)-1}{\exp(ze\Psi/2kT)+1} \quad \text{and} \quad \kappa = \left(\frac{2e^2n_oz^2}{\varepsilon kT}\right)^{\frac{1}{2}} = \left(\frac{2e^2N_Acz^2}{\varepsilon kT}\right)^{\frac{1}{2}} \tag{7}$$

N_A=Avagadro's Number
c = electrolyte concentration

While this equation provides valuable insight into the interpretation of κ, as described below, the Debye-Huckel approximation is generally applied for stability prediction because it yields relatively simple equations which allow qualitative examination of the double layer [5]. The above combines an equation derived from Poisson (which implies potentials associated with various charges are additive) and Boltzmann which describes the relationship between charge and potential exponentially. This creates an inherent inconsistency in the equation, therefore, it can only be solved for limiting cases and approximations must be made to smooth out these inconsistencies [1]. This is referred to as the Debye-Huckel approximation. Applying the Debye-Huckel approximation allows for a simplified function of Ψ.

$$\frac{ze\Psi_o}{2kT} << 1 \quad \text{therefore:} \quad \exp\left[\frac{ze\Psi_o}{2kT}\right] \approx 1 + \frac{ze\Psi_o}{2kT}$$

resulting in...

$$\Psi = \Psi_o \exp(-\kappa x) \tag{8}$$

The approximation assumes low potentials ($\approx$25.7mV) and is solved explicitly using $z_i e\Psi = kT$ for monovalent indifferent ions. While the Debye-Huckel approximation is weakened in its application by the limitation of low potentials, it is simpler to understand than more complex models and when these models are limited to low potentials, they produce the Debye-Huckel result [1]. The approximation also qualitatively agrees with the effects of electrolyte concentration and valence produced by more complex models. The Debye-Huckel approximation also allows for interpretation of the parameter κ.

Because κ appears in the dimensionless parameter *exp(-κx)*, it must have the unit of reciprocal length. Therefore, κ^{-1} has been called the double layer "thickness" and all distances pertaining to the double layer are deemed small or large relative to κ^{-1}. κ is also concentration dependent. Equation (7) can be used to calculate the double layer "thickness" with respect to electrolyte strength and concentration. (Table 1).

Table 1 Double layer thickness with respect to electrolyte concentration. Adapted from [1].

Molarity	$z_+:z_-$	κ (m^{-1})	κ^{-1}(m)
0.001	1:1	$1.04\text{x}10^{8}$	$9.61\text{x}10^{-9}$
0.001	2:2	$2.08\text{x}10^{8}$	$4.81\text{x}10^{-9}$
0.001	3:3	$3.12\text{x}10^{8}$	$3.20\text{x}10^{-9}$
0.01	1:1	$3.29\text{x}10^{8}$	$3.04\text{x}10^{-9}$
0.01	2:2	$6.58\text{x}10^{8}$	$1.52\text{x}10^{-9}$
0.01	3:3	$9.87\text{x}10^{8}$	$1.01\text{x}10^{-9}$
0.1	1:1	$1.04\text{x}10^{9}$	$9.61\text{x}10^{-10}$
0.1	2:2	$2.08\text{x}10^{9}$	$4.81\text{x}10^{-10}$
0.1	3:3	$3.12\text{x}10^{9}$	$3.20\text{x}10^{-10}$

The results show a similar thickness to that of the capacitor model [1], however, the diffuse model is superior in its physical description and also shows how κ^{-1} varies inversely with electrolyte strength (z) and with $c^{1/2}$ for a symmetrical electrolyte. These results are shown graphically in Figure 1. Note that the curves are marked where x corresponds to κ^{-1}. Clearly this is not the thickness of the double layer, however, if we examine the idea of electroneutrality at a charged interface for the equation of potential as a function of distance

$$\frac{d^2\Psi}{dx^2} = -\left(\frac{\rho}{\varepsilon}\right) \tag{9}$$

and assume total charge from the particle is balanced by the medium which stretches to ∞, then integration of the charge density yields

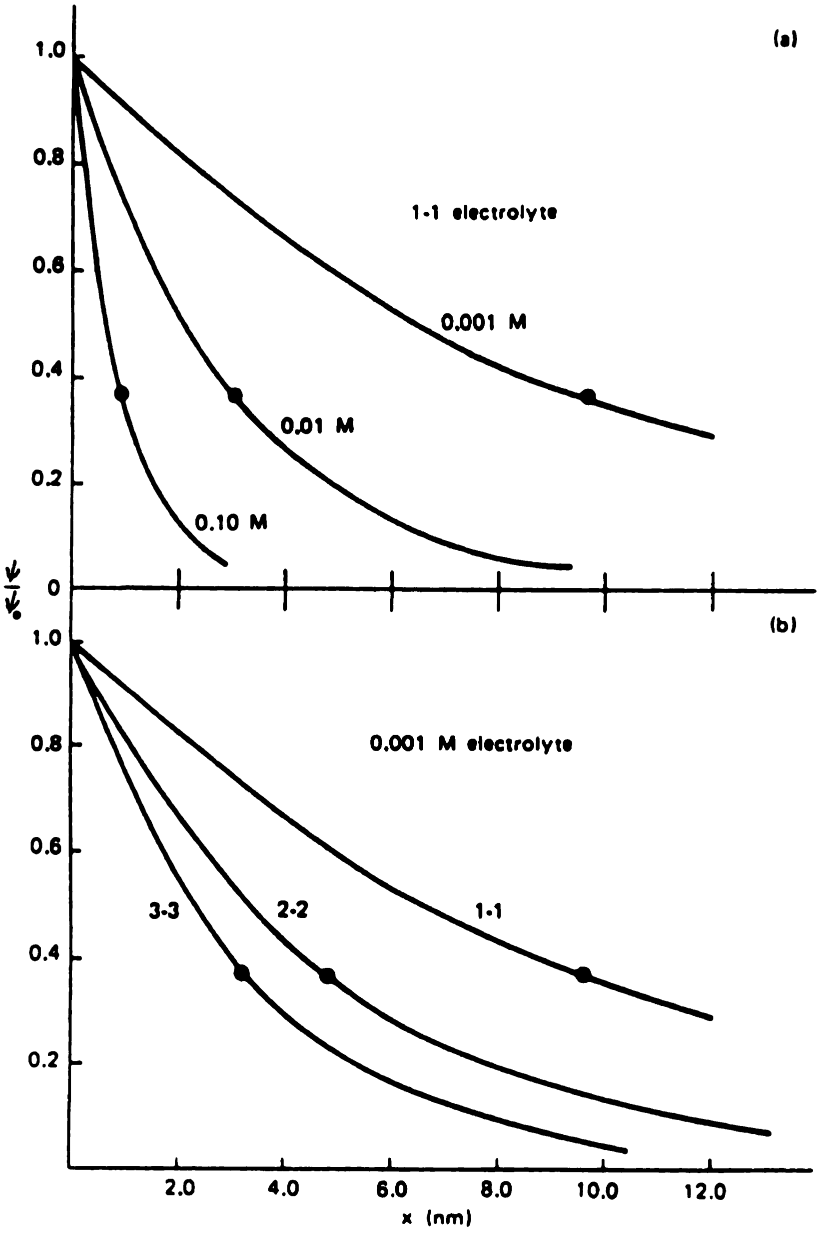

Figure 1 Normalized double layer potential versus interparticle separation according to Debye-Huckel. (a) shows variation with electrolyte concentration (b) shows variation with electrolyte valence for 10^{-3} M symmetrical electrolyte. Adapted from [1].

$$\sigma = \varepsilon\left(\frac{\Psi_0}{\kappa^{-1}}\right) \tag{10}$$

which is the same as treating the charged surface and the diffuse double layer as the plates of a parallel plate capacitor [1] by replacing Ψ_0 with $\Delta\Psi$and d with κ^{-1} where d is the separation distance, hence, κ^{-1} again becomes the double layer thickness.

While inconsistencies exist in the Poisson-Boltzmann equation, they can be shown to be minor under the conditions found in colloidal suspensions, even if the potential is not small [1]. Debye-Huckel shows Ψ varies exponentially with x, Guoy-Chapman reveals that the complex ratio γ varies with x. This expression can be reduced to Debye-Huckel by assuming low potentials and expanding the exponentials. This can also be reduced to the limiting case for high potentials yielding

$$\Psi = \frac{4kT}{ze}\exp(-\kappa x) \tag{11}$$

which along with Debye-Huckel bridge the true potential. Debye-Huckel, however, is the most useful approximation when modeling colloidal ceramic systems due to the assumptions made for greater mathematical simplicity.

Stern Theory

Limitations to the Gouy-Chapman model are realized by examining the expression for charge density.

$$\sigma = \frac{\varepsilon kT\kappa}{2\pi ze}\sinh\left(\frac{ze\Psi_0}{2kT}\right) \tag{12}$$

This relation yields 23 ions A^{-2} for the case of 0.1M solution of 1:1 electrolyte [1]. This is physically impossible and is due to the fact that Gouy-Chapman treats ions as point charges.

Stern addresses this problem by dividing the diffuse double layer into 2 regions, the Stern layer and the diffuse layer [5]. (Figure 2) The Stern layer is composed of specifically adsorbed ions and is separated from the diffuse layer by the Stern plane located approximately one hydrated ion radius from the particle surface. Stern theory allows for finite ion size by applying a Langmuir-type adsorption isotherm to the particle surface and as the surface approaches saturation, the potential drop across the Stern layer becomes constant. This sets up a situation similar to a parallel plate capacitor where the capacities of the Stern layer (C_1) and diffuse layer (C_2) are given by

$$C_1 = \frac{\sigma_o}{\Psi_o - \Psi_d} \; ; \; C_2 = \frac{\sigma_o}{\Psi_d} \qquad \text{Therefore,} \quad \Psi_d = \frac{C_1 \Psi_o}{C_1 + C_2} \tag{13}$$

Outside the Stern layer the double layer is still accurately described by Gouy-Chapman or Debye-Huckel, except Ψ_d rather than Ψ_0 is used. While Stern theory removes the limitation of Gouy-Chapman, it introduces parameters which are difficult to estimate, such as κ, ϕ, and δ [5], but as far as colloidal stability is concerned, we are mainly concerned with the outer layer. Stern actually extends the validity of Debye-Huckel by using the lower Ψ_d potential (therefore, Debye-Huckel remains valid for higher true surface potentials because these cases are represented by the appropriate Stern potential). This becomes a greater advantage in stability prediction, because the potential at the Stern layer can be approximated by the zeta-potential, which can easily be determined experimentally.

Zeta-Potential

The experimentally measured ζ-potential is the potential at the surface of shear (Figure 2). This imaginary plane separates adsorbed ions on the charged surface from the

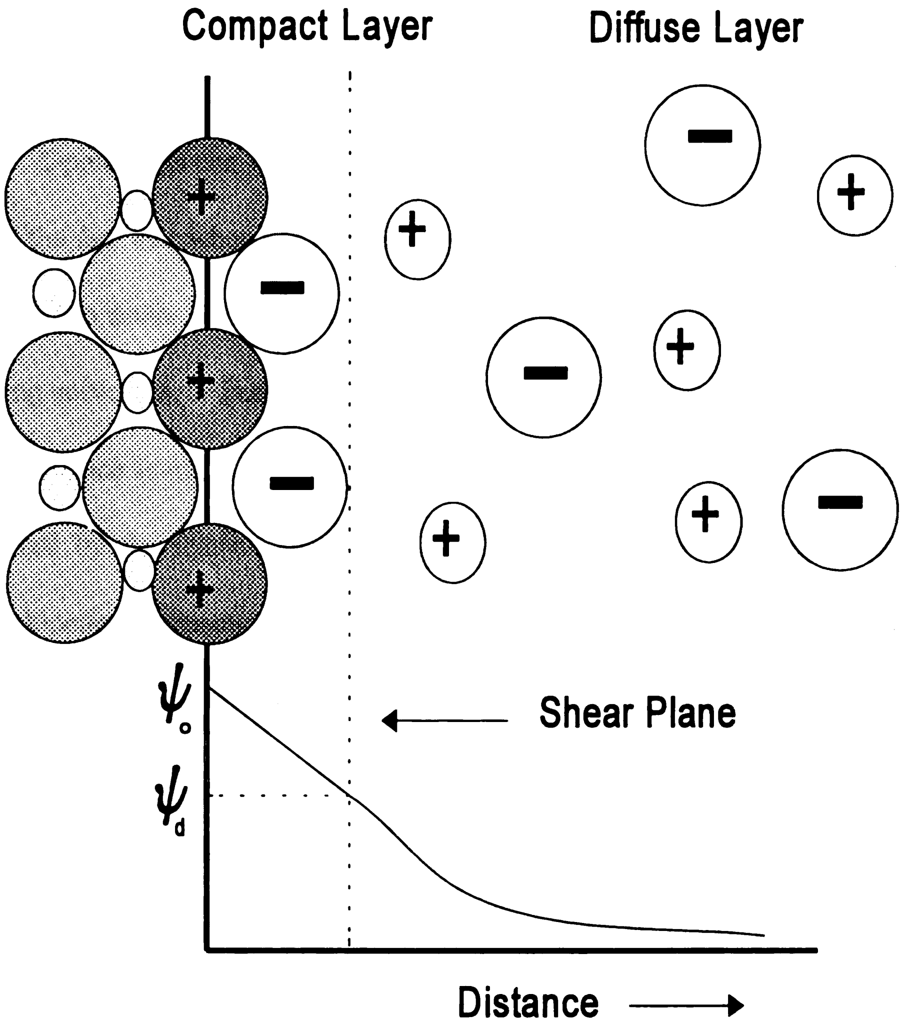

Figure 2 Stern potential Ψ_d is evaluated at the shear plane which represents the charged surface, adsorbed ions, and suspension medium which move as one unit. Charged surface is represented by shaded spheres along the y-axis. Adapted from [5].

electrolyte solution. ζ-potential is assumed to be slightly smaller than ψ_d due to the effect of solvent which may also move with the particle within the surface of shear. This error is ignored for lyophobic colloids and becomes pronounced only at high electrolyte concentrations [5].

ζ-potentials can be measured experimentally by electrokinetic phenomena. This is due to the fact that when the double-layer is subject to an electric field, the charged surface is excited to move in the appropriate direction and mobile counter ions move in the other carrying solvent with them. The opposite is also observed. An electric field is set-up if the charge surface is excited to move relative to the diffuse double layer. ζ-potential can be measured by the relative movement of charged particles in a liquid by many different electrokinetic phenomena including electrophoresis, electro-osmosis, and streaming potential [5]. Because electrokinetic phenomena are directly related to the mobile part of the double layer, it is ideally suited for calculation of the ζ-potential. While this does not directly measure surface potential ψ_0, ζ has an assumed identity with ψ_d which can be used with Stern theory to predict colloidal forces present. ζ-potential is most commonly calculated from the electrophoretic mobility which is determined by elctrokinetic experiment. Mobility is sensitive to double layer characteristics and is calculated by two different relations, the Huckel equation for small κa and the Smoluchowski equation for large κa [5]. Knowing the relationship between ζ-potential and mobility, ζ-potential can be calculated by Electrokinetic analysis (ESA) [6,7]. The ESA effect uses an alternating electric field which generates sound waves due to the induced oscillatory movement of suspended particles in the field. O'Brien [8] first showed how the sound wave signal could be used to interpret dynamic mobility. For $\kappa a>>1$ (particle radius >> double layer thickness), dynamic mobility is related to the static mobility and therefore, the ζ-potential. While this measurement of ζ-potential is involved mathematically, it has been shown to compare well with electrophoretic results using ceramic powders such as Si_3N_4 and Al_2O_3 [6,9]. Thus it is a suitable method for use in stability prediction [10].

HHF Theory

The ideas of spontaneous charge generation by particles in suspension have been outlined. Repulsive forces generated by spontaneous charge formation act to reduce coagulation, while van der Waals forces can result in coagulation of identically charged particles. However, when two different species are in suspension, mutual coagulation can occur by oppositely charged particles. A study by Hogg et al. [12] (HHF) quantitatively explains mutual coagulation. HHF theory predicts surface charges by using DLVO theory coupled with the Debye-Huckel approximation, and ignores chemical interaction between suspended species. The two components must be of similar chemical type and have the same potential determining ions. Debye-Huckel is used to solve for the distribution of potential as a function of distance between particles by defining them as two parallel plates of differing potential. This result is then used to compute V_I, the interaction energy between two flat double layers as a function of surface potential and separation distance between plates. V_I is subsequently used in the formulation presented by Derjaguin [11] for the interaction between two dissimilar spherical particles.

$$V_R = \int_0^\infty 2\pi h V_I dh \tag{14}$$

Where *h* is defined in Figure 3. *h* is then mathematically related to the separation distance *d* and the integral is evaluated to yield equation (15).

$$V_R = \frac{\varepsilon a_1 a_2 \left(\Psi^2{}_{01} \Psi^2{}_{02}\right)}{4\left(a_1 + a_2\right)} \left[\frac{2\Psi_{01}\Psi_{02}}{\left(\Psi^2{}_{01} + \Psi^2{}_{02}\right)} \ln\left(\frac{1+\exp(-\kappa H_0)}{1-\exp(-\kappa H_0)}\right) + \ln\left(1-\exp(-2\kappa H_0)\right) \right] \quad (15)$$

This relation holds for interacting double layers of dissimilar particles and reduces to Derjaguin's result for similar particles [11]. The assumptions made mathematically require Ψ_{01} and $\Psi_{02} \leq 25\text{mV}$ and the double layer thickness be small with respect to particle size. However, experimentation revealed (above equation) to be a good approximation for cases up to 50mV [12] and $\kappa a > 10$ [13].

HHF theory uses the repulsive force (equation 15) and adds this to the attractive van der Waals force (1) to compute a total potential energy of interaction as demonstrated in Figure 4. This curve represents the case where interacting particles have significant (yet still falling within the assumption of "low") same sign potentials. V_t displays a maximum at small separation distances which physically represents an energy barrier that must be overcome for coagulation to occur. When potentials are very small or of opposite sign, there is no energy barrier and coagulation can readily occur. Therefore, V_t plays a significant role in the kinetics of mutual coagulation (stability).

When a barrier to coagulation exists, the rate of coagulation is defined by a factor *W*. Defined by Fuchs [14] and modified by Overbeek [15] for dissimilar particles, W is the number of collisions resulting in coagulation over the total number of collisions.

$$W = \left(a_i + a_j\right) \int_{a_i + a_j}^{\infty} \exp\left(\frac{V_t}{k_t}\right) \frac{dr}{r^2} \qquad (16)$$

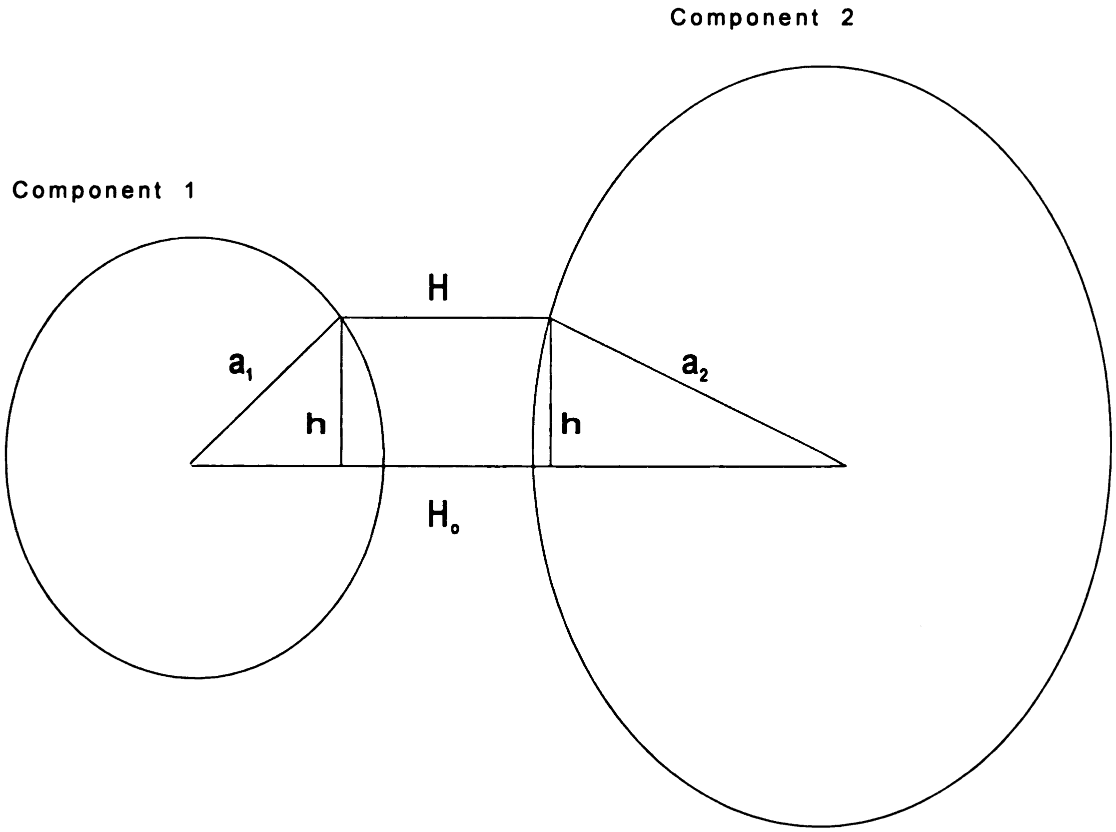

Figure 3 Simplifying parameter h as defined by Derjaguin from equation (14). Adapted from [10].

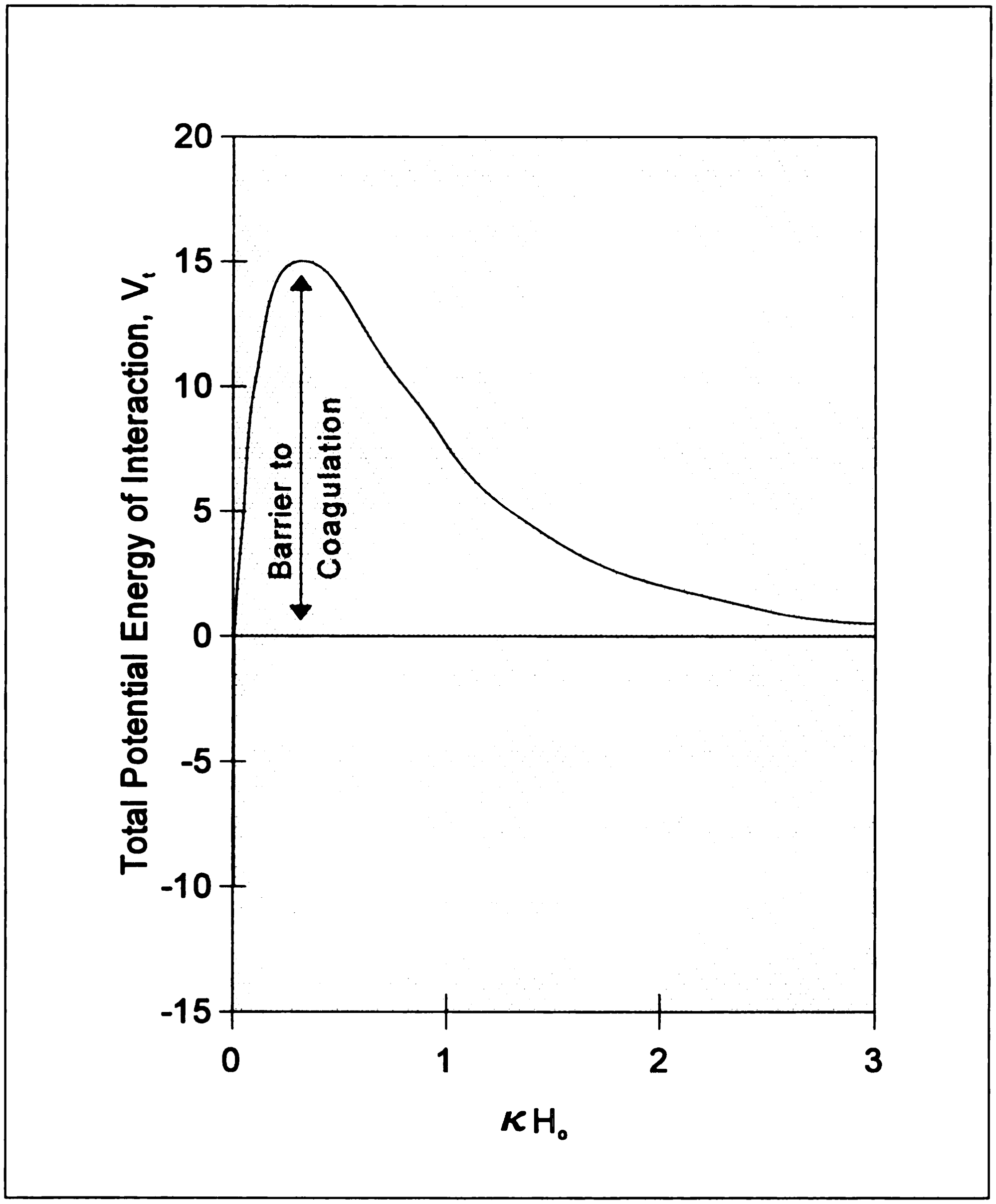

Figure 4 An energy barrier to coagulation is necessary for suspension stability. Plot is the result of adding $V_r + V_a$ for a stable suspension. Adapted from [5].

Provided the number of collisions is dependent only upon the relative number of particles [12]. Three stability ratios are needed to characterize a system of 2 dissimilar particles. W_{11}, W_{22}, for homocoagulation and W_{12} for heterocoagulation, or agglomeration of dissimilar particles. Together, these define an overall stability ratio W_t.

$$\frac{1}{W_t} = \frac{P_{11}}{W_{11}} + \frac{P_{22}}{W_{22}} + \frac{P_{12}}{W_{12}} \tag{17}$$

Where P is the probability a collision of type 11, 22, or 12 will occur. Wilson and Crimp [10] used a modified version of HHF theory in the development of a stability prediction model.

Prediction of Stability

Wilson and Crimp [10] have shown that the theories of stability presented above, can be mathematically modeled to predict conditions under which composite stability occurs using a modified version of HHF theory. The HHF model is well suited for this application because it includes the kinetic aspects of stability and provides quantitative expressions for the stability of non-identical particles. These modifications include using ζ-potential to estimate the surface potential of suspended particles (by applying Stern theory to characterize double layers) and using Bleier's method of determining the Hamaker constant for ease of application to different composite ceramic systems. Wilson and Crimp showed success applying their model, *Suspension Stability*©, to predict the stability of Si_3N_4 and SiC powders in aqueous suspensions.

Once a suspension of appropriate ceramic components has been stabilized, ceramic components must be removed from suspension and formed to near net shape. One method for accomplishing this is freeze-drying.

FREEZE-DRYING

Freeze-drying is used to remove the water from disperse composite suspensions and leaves behind a dry, intimately mixed powder suitable for pressing [16]. Drying of ceramic powders at elevated temperatures can cause changes in powder characteristics (i.e.: surface groups present, oxidation) and can bring about the formation of hard agglomerates which require milling and sieving to remove. Powders containing hard agglomerates rarely press to homogeneous green compacts [16]. Freeze-drying is a simple alternative to this procedure. The freeze-drying process can be divided into 3-steps; (1) pre-freezing (2) primary drying and (3) secondary drying [17,18].

Pre-freezing

Because freeze-drying involves the sublimation of water from the suspension, the suspension must first be adequately frozen to ensure success of the freeze-drying procedure. The major volume of a suspension to be freeze-dried is the supernatant (water and an added amount of acid or base). The acid or base will act to change the freezing point of the water and forms a eutectic mixture. As the water freezes, solute is rejected from the freezing water and forms pockets of liquid with a freezing point lower than 0^{o}C. Pockets of eutectic liquid must all be frozen, or they will instigate melting under the low pressure of freeze-drying conditions. Pre-freezing is usually carried out in a shell freezer [18]. Shell freezing involves freezing a suspension to the walls of a cylindrical vessel which increases the surface area to volume ratio of frozen suspension. This acts to improve the efficiency of primary drying.

Primary drying

After pre-freezing is complete, conditions must be quickly established to promote sublimation of aqueous suspensions before melting begins. Temperature and pressure must be carefully adjusted to keep the suspension within the sublimation range, but not so cold that sublimation occurs too slowly. Efficient freeze-drying takes place just below the triple point, or lowest freezing eutectic, low enough to avoid incipient melting, and high enough to establish a significant vapor pressure above the surface of the frozen suspension. Increasing vapor pressure encourages sublimation from the frozen suspension to the condenser. By keeping the condenser pressure as low as possible, a vapor pressure differential is created and vapor moves from the suspension to the condenser. The flow of water vapor from the suspension to the condenser is greatly improved by placing the entire system under a vacuum. A vacuum pump also acts to remove non-condensable gases from the system.

Because it takes ten times the energy to sublime water as it does to freeze it, energy needs to be added to the suspension to keep the temperature gradient with the condenser as strong as possible. Leaving the cylindrical vessel at room temperature provides enough heating to counteract the evaporative cooling that takes place during sublimation. This becomes most important as the drying front moves through the thickness of the frozen shell. Water molecules must travel through the dried layer above, therefore, driving force must remain high in order for the water to escape to the condenser.

Secondary drying

Secondary drying occurs after the suspension appears dry. Upon completion of primary drying, the material may still contain up to 8% residual moisture [18]. Secondary drying occurs by isothermal desorption of bound water from the ceramic powder. The outside temperature of the vessel is raised while keeping pressure and condenser at the same levels. Secondary drying is carried out for 1/3 to 1/2 the time of primary drying. While freeze-drying offers an effective way of preparing mixed composite powders, little research has focused on the topic.

M.W. Real [16] demonstrated freeze-dried ceramic powders could be pressed to form homogeneous compacts. At water contents of 4:1 by volume and greater, freeze-dried powders form a fragile plate-like structure which breaks down easily by hand into a fine powder suitable for processing of engineered ceramics.

The properties of engineered materials, especially engineering ceramics, is dependent upon its internal flaw structure. This internal structure is indicative of the processing of the material which controls the internal pore structure. The distribution of pores can, in turn, have an effect on grain structure and second phase distribution within a composite. Therefore, control of final properties involves control over grain size along with pore and second phase distribution which all requires knowledge of how pores are removed from a densifying compact. How green structure effects sinterability is addressed in the next section.

LIQUID PHASE SINTERING

Sintering in the presence of a liquid provides enhanced densification at lower temperatures than free sintering [19]. Disadvantages arise from the fact that there are many interfaces and energies of individual components to consider in liquid phase sintering, as well as solubilities of phases involved and viscosity of the accompanying liquid. Therefore, analytical treatments of liquid phase sintering tend to be more qualitative in nature than those associated with solid state sintering, and applications of liquid phase sintering also tend to be less predictable in nature. Liquid is provided by the addition of a second phase material with a lower melting (or glass forming) temperature than the matrix. Liquid phase sintering is characterized by three distinct over-lapping steps [20,21] as shown in Figure 5. When liquid forms, interparticle friction drops and capillary forces accelerate particle rearrangement. Densification by rearrangement is rapid and depends upon particle size, green density and the amount of liquid present. Solution-reprecipitation occurs concurrently, but is overshadowed by rearrangement during the initial stages of sintering. In general, the solubility of a grain is inversely proportional to its size. Therefore, small grains preferentially dissolve in the liquid setting up a concentration gradient and material is precipitated on to larger, less soluble, grains. This is termed "Ostwald ripening" and contributes to densification as well as grain growth. The last stage of persistent liquid phase sintering involves solid state sintering mechanisms. While solid state sintering is occurring throughout the entire process, its effects dominate only upon completion of the first two steps. This stage is characterized by grain coarsening and either pore elimination or growth

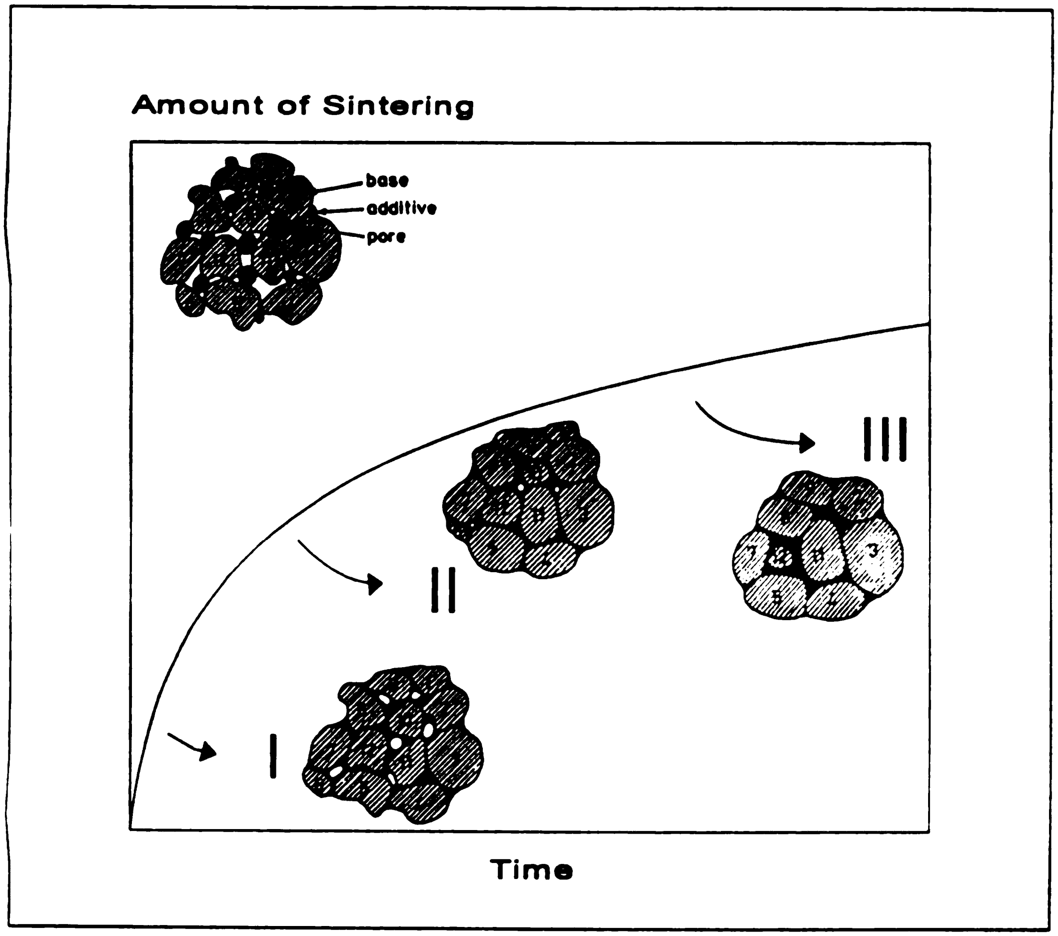

Figure 5 Evolution of a green ceramic compact sintered with the assistance of a liquid phase. I = initial stage, II = intermediate, and III = the final stage of sintering. Adapted from [21].

depending upon entrapped gases within the pore structure. Prolonged final stage sintering may degrade the final properties of liquid phase sintered components [21].

Initial Stages

While this is the shortest of the 3 stages, rearrangement often results in significant densification. Microstructural changes occurring during the first stage include melting and solid-liquid solubility, penetration and fragmentation, and rearrangement. These steps, however, may be more difficult to characterize in a more complex ceramic system where viscosity, interfacial energy, and the amount of liquid are continually changing. Intermediate compounds may also form and change the quality of the liquid present. Despite these shortcomings, the classic models of liquid phase sintering can be used to characterize successful sintering systems.

Melting and Solubility

The solubility ratio between the additive and matrix is an important aspect of initial heating during liquid phase sintering. High solid solubility in the liquid improves rearrangement by surface smoothing thus reducing interparticle friction. A low solubility ratio is characterized by pore formation at the prior additive particle sites. This greatly reduces rearrangement and can cause compact swelling rather than densification. In general, the greater the solid solubility, the greater the final density and the less additive needed to achieve final density [21]. As temperature increases, the liquidus moves closer to the solid composition and the liquid can hold more solid in solution thus increasing the amount of liquid present. Rearrangement can also be enhanced by using smaller additive particle sizes which can improve distribution of the additive within the compact thus forming a more homogeneous liquid phase. Large additive particle sizes are detrimental to final pore removal, and it is common to ball-mill additive and matrix particles together for improved homogeneity, reduced particle sizes, and to break apart hard agglomerates for improved packing [20]. After the initial heating stage where diffusivity and solubility dominate sintering behavior melt formation begins.

During melt formation, the most important characteristic of the liquid is how well it wets the solid. A wetting liquid will spread through the compact by capillary forces and the major portion of densification that can occur by rearrangement will occur within minutes of liquid formation. Of course, this rate is limited by the thickness of the liquid layer and the viscosity of the liquid. Poor wetting liquids are evidenced by liquid exuding from the compact surface [21]. The compact will remain intact while the liquid forms a bead on the exterior. Further densification is dependent upon the solubility between solid and liquid causing particle smoothing and reduced interparticle friction allowing for easier, faster particle rearrangement [21]. Both wetting and high solid solubility are important liquid characteristics and necessary for complete densification.

Penetration and Fragmentation

Penetration describes the movement of liquid through pore and grain structures within a compact driven by either capillary or reactionary forces. This driving force is strong initially because the liquid has not yet achieved an equilibrium composition and, therefore, has a high curvature which aids solubility and allows the liquid to break solid-solid interfaces [21]. Penetration is dependent upon liquid viscosity and reactivity as well as on dihedral angle. This is the angle made when the liquid intersects a solid-solid interface. This angle is dependent upon the ratio of solid-solid to solid-liquid interfacial energy. While dihedral angle is important, this work centers around a current additive system, so good wetting conditions are assumed. Fragmentation can result in a grain structure smaller than the starting particle size when liquid wets grain boundaries and breaks apart agglomerates. Compact swelling can occur during fragmentation, but later aids densification by secondary rearrangement and reducing the overall particle size which, again, improves rearrangement and will aid the solution-reprecipitation process.

Rearrangement

The formation of a wetting liquid creates attractive forces between particles and causes a hydrostatic pressure on existing pores. Influenced by reduced interparticle friction due to particle smoothing, particles repack to a higher coordination. Rearrangement can be broken down into two stages, primary and secondary. Primary rearrangement involves individual particles while secondary rearrangement involves clusters or fragments of individual particles. Secondary rearrangement becomes important when liquid is unevenly distributed throughout the compact. This uneven distribution causes clusters of primary particles which may or may not fragment. As these clusters grow and repack they release liquid to the intercluster region. Kingery [20] showed that time is not a significant factor in rearrangement and later demonstrated this experimentally with oxide and carbide-metal systems [22]. More important factors include volume fraction liquid, particle size, dihedral angle, and green density.

Liquid present in $35^{v}/_{o}$ can facilitate full densification by rearrangement [20], but most systems are kept below $20\ ^{v}/_{o}$ to avoid shape distortion, therefore, other processes such as solution-reprecipitation must be active in order to achieve full density. Rearrangement processes are less efficient with non-spherically shaped particles. Kingery showed [20] that capillary forces vary inversely with particle size. Experimental results confirm that small particle sizes are beneficial for rearrangement [23,24]. High green densities create more mechanical interlocking between particles and have less vapor phase present. Consequently, the capillary force for rearrangement is reduced. In general, high green densities reduce the densification rate, but increase the final density of the compact due to the lower initial porosity. Rearrangement consequently must change this initial pore structure for densification to occur [25].

The pore structure changes in the initial stages of sintering due to the formation of new pores at former additive particles sites, and pore coarsening due to rearrangement. Capillary action draws liquid from the site of the additive particle leaving a pore behind. (Another reason why small additive particle sizes are important.) Pore refilling can occur only if glass composition remains consistent during prolonged sintering [21]. As the liquid spreads and capillary forces activate, new contacts are made which increase the rigidity of the compact. It's at this point the initial stage processes slow and the intermediate stage of liquid phase sintering dominates.

Intermediate Stage: Solution-Reprecipitation

While solutionizing and reprecipitation occur simultaneously with rearrangement, their effects on the compact do not dominate until rearrangement is complete. The intermediate stage of liquid phase sintering is characterized by grain shape accommodation, densification, coalescence and neck growth, and pore filling. There must be an appreciable solubility of the solid in the liquid additive for sintering in the intermediate stage to be successful. Grain growth also occurs concurrently with the intermediate stage, but it is generally treated as the final stage of liquid phase sintering.

Grain shape accommodation

Because most useful liquid phase sintering systems contain small amounts of liquid $\leq 20^{v}/_{o}$, there is still porosity within the compact after rearrangement. Grain shape accommodation acts to reduce this porosity. Grain shape accommodation occurs by dissolution of small particles and dissolution at the contact points of larger particles. Dissolved material reprecipitates away from contact points [21,26], thus altering particle shapes and acting to fill pore space. Grain shape accommodation is a mechanism for both densification and grain growth [27].

Densification

The rearrangement process leaves behind densely packed particles surrounded by a thin layer of liquid. The liquid at contact points causes capillary pressure between particles creating a compressive load within the compact which Kingery [20] has shown increases the solid solubility at those points. This results in material transfer away from the contact points which causes particle centers to approach one another resulting in densification. This is termed contact flattening and is one of three mechanisms used to describe densification of liquid sintered compacts. A second mechanism involves dissolution of small grains and reprecipitation onto larger grains, often resulting in grain shape accommodation [27]. A third mechanism involves solid state diffusion. A compact with small amounts of liquid or a partially wetting liquid [28], may rely on solid state diffusion for additional densification, however, solid state diffusion is much slower than diffusion through a liquid and its effects are apparent only in the later stages of sintering. The effects these mechanisms have on the compact are summarized in Table 2.

Table 2 Effect of sintering mechanism on a powder compact. Adapted from [21].

Factor	Contact Flattening	Dissolution of Fines	Neck Growth
Material Source	contact zone	small grains	grain boundary
Transport Path	liquid	liquid	solid
Transport Rate	rapid	rapid	slow
Shape Accommodation	yes	yes	yes
Grain Coarsening	no	yes	no
Solubility in liquid	is required	is required	not required

There are differing opinions on which of the densification mechanisms is dominant. Observations by Kaysser et al. [29] found densification to correlate with the onset of rapid grain growth. Examination revealed a direct correlation between densification and dissolution of fine grains [27]. According to research on glass phases in ceramics [20,30,31] the liquid width between ceramic grains is only a few atomic diameters. Therefore, contact flattening would not be a dominant densification mechanism for these systems. Regardless of the dominant mechanism, shrinkage is proportional to time$^{1\backslash 3}$ [23,32]. Shrinkage is enhanced in the intermediate stage by high solid solubility, small particle sizes, and longer times in the intermediate range. Temperature effects are most strongly observed through enhanced diffusivity, although it may have an effect on solubility and surface energy, especially in mixed component ceramic systems [21].

Neck growth and coalescence

At the end of the intermediate phase of sintering contacting particles show a stable neck with size dependence on dihedral angle, grain size, and volume fraction solid present. Neck growth occurs by material transfer from either the grain contact point, which results in densification, or the grain surface which results in no densification. Rate of neck growth depends upon the mechanism involved, either coalescence, solid state diffusion, or solution-reprecipitation. Neck growth can be a detriment to densification because if a continuous solid particle structure is formed, densification will slow, ending the intermediate stage.

Coalescence describes the fusing of two dissimilarly sized grains into a single grain, most commonly by grain boundary movement [21]. Coalescence is used as a mechanism to describe grain growth and the reduction in grain number during sintering. Coalescence is a function of the number of grain contacts and is therefore more prevalent in compacts with high green densities. Coalescence of particles can also contribute to densification by filling the neck region between two spherical particles in contact [26].

Pore filling

While grain shape accommodation assists pore filling at the beginning of the intermediate stage of sintering, pores formed at former additive sites may exist throughout most of the intermediate stage. The coarser the additive particle size, the longer the incubation time for filling (i.e.: small pores fill first). Pore filling requires grain growth and accommodation. In order for pore filling to occur, the liquid meniscus radius must exceed the pore radius. Therefore, there is a critical grain size for pore filling [33] and prolonged sintering may be required for grains to grow large enough for the liquid to reach conditions favorable for pore filling. However, as pores fill, the effective liquid content of the system is reduced and it becomes harder to fill succeeding pores.

Final Stage Sintering: Grain Growth

Because densification and microstructural coarsening proceed by similar mechanisms, it is important to understand coarsening in order to achieve full density but maintain microstructural control. Further densification in the final stages of sintering is highly dependent upon pore characteristics and entrapped gasses within the pores. Because pore structure typically scales the particle size, smaller particle sizes should leave behind smaller, easier-to-remove pores. Sintering in a non-soluble gas atmosphere increases the probability of trapping gasses within the pore structure. Pore elimination is further inhibited by the resulting continuous solid structure due to neck formation between solid grains within the compact, typical of final stage sintering.

Continued densification

Densification can continue despite the skeletal nature of the powder compact via continued solution-reprecipitation driving grain shape accommodation for final pore removal. This is possible only if inhibiting factors such as entrapped gasses, decomposition products [34], gross imperfections in packing [35,36], and reaction products with the atmosphere [23] can be avoided. Another source of entrapped gasses is from decomposition of the compact material. Release of vapor from reaction products can produce increasing vapor pressures within the pore structure and cause swelling.

Grain growth

While grain growth is occurring along with densification, the final stage of sintering is characterized by the dominance of grain growth. The driving force for grain growth in liquid phase sintering is the decrease of interfacial energy due to the decrease in particle curvature and subsequent reduction of the solid-liquid interface. Grain growth, as with densification, can be diffusion controlled or reaction controlled and again with multi-component systems tends to be reaction controlled. With either controlling mechanism, the rate of grain growth is increased by increasing the volume fraction solid and raising the temperature [21,37]. Grain growth can also be inhibited by the presence of a second immiscible solid phase such as SiC whiskers in Si_3N_4 [38,39].

Processing Considerations

Together with the sintering mechanisms discussed previously, processing concerns determine the sintering behavior of a powder compact. A major concern of industry involves dimensional control [21]. Shrinkage is high when a liquid phase is present during sintering, but dimensional control is improved for compacts with a high green density. Homogeneity is also important to maintain equivalence of dimensional changes from compact to compact.

Particle characteristics

In general, small particle sizes have an advantageous effect on sintering. A narrow particle size distribution is also beneficial [19]. A large particle size distribution or aggregates within the starting powders can induce exaggerated grain growth [19,21] or create gross packing deformities [35,40] resulting in abnormally large pores. Grain shape can also have an effect on compaction. Spherical particles show better rearrangement because more capillary pressure can be developed between particles and spheres leading to greater compact uniformity. Irregular powders can increase the green strength, but show reduced rearrangement and densification due to greater interparticle friction as well as more non-uniformity in green density [41].

Green properties

High green densities reduce rearrangement due to increased interparticle friction. Green density plays a stronger role in sintered density as the amount of grain boundary liquid decreases. Increased green densities also improve dimensional control, but because shrinkage varies directly with green density, non-uniformities in density can lead to uneven shrinkage. Because initial stage sintering effects are reduced by increasing green densities, effective intermediate stage sintering becomes more important.

Heating and cooling rates

Diffusional homogenization can have a detrimental effect on liquid phase sintering. Homogenization of the liquid composition due to slow heating rates can affect wetting characteristics and in extreme cases, suppress liquid formation altogether [21]. In general, rapid heating rates improve densification, while slower heating rates and isothermal holds, below liquid formation temperatures prove, detrimental [42,43]. However, if heating rates are too rapid, they can lead to entrapped porosity. While cooling rates are rarely optimized, post-sintering treatments can be employed to improve mechanical properties (i.e.: anneals to induce grain boundary crystallization) [44]. The greater the cooling rate, the greater the saturation of solid in the liquid phase and the greater the sintered strength. However, rapid cooling at the solidification temperature can cause solidification porosity [21].

Temperature and Time

Liquid phase sintered materials show a strong temperature sensitivity. As temperature increases, diffusion rates increase, wetting and solubility increase, viscosity decreases, and the amount of liquid increases. Time and temperature must be optimized in order to avoid excessive grain coarsening, harmful decomposition reactions or intermediate compound formation which can reduce the amount and viscosity of available liquid. This is especially important for pressureless sintering of Si_3N_4. Increasing temperatures above 1850°C enhances decomposition and inhibits densification mechanisms [45]. Most densification models for liquid phase sintering show density to be a weak function of time and increased sintering times often lead to degradation of mechanical properties [21].

Atmosphere

The proper sintering atmosphere acts to reduce formation of harmful films, such as oxides, or as is the case with Si_3N_4, suppress decomposition. Insoluble atmospheres can reduce densification rates when gasses become entrapped in the porosity. Densification rates are then controlled by the diffusivity of the gas within the matrix [45]. Sintering in a vacuum can eliminate this problem, but will not suppress decomposition reactions.

LIQUID PHASE SINTERING OF Si_3N_4

Sintering of Si_3N_4 to near theoretical density often requires the assistance of liquid phase sintering along with hot pressing or HIPing [46-49]. Hot pressing and HIPing can produce dense high quality Si_3N_4 components, but lack the versatility pressureless sintering lends to automation and the production of complex shapes [50]. Si_3N_4 is difficult to densify because of its low thermal conductivity and strong covalent bond structure giving it a low self-diffusivity [44]. Self-diffusivity cannot be improved by increasing the sintering temperature because decomposition of Si_3N_4 becomes a problem above 1825°C [34,51]. Therefore, higher temperatures cannot be used to boost the diffusivity without the addition of a high pressure N_2 gas environment [52]. Diffusivity, and thus densification, can be enhanced at lower temperatures by addition of a second phase which forms a liquid at sintering temperatures. Typical additives, or sintering aids, to Si_3N_4 include MgO, Y_2O_3, and Y_2O_3+Al_2O_3. While other sintering aids have been examined (ie:CeO_2, La_2O_3, Sm_2O_3 [44,51]), the former remain the most popular currently in use. MgO was one of the first sintering aids used in pressureless sintering of Si_3N_4 [45]. Work by Mitomo et al. [53] indicated Si_3N_4 could be pressureless sintered to >90% theoretical density with additions of 5% wt. MgO with strengths that rivaled hot pressed Si_3N_4 with the same additions. Studies by Terwilliger [54] yielded similar densities but indicate substantial strength degradation at temperatures above 1000°C. Lange [54] associates this degradation with amorphous grain boundary phases. Reduced crystallinity is due to the lack of Mg solubility within β-Si_3N_4, and Ca impurities which lowers the softening temperature of magnesium silicate along grain boundaries [56]. Additions of Y_2O_3 alone show improvements over MgO, with greater high temperature strengths. Densification of Si_3N_4 with MgO additions is highly dependent upon impurities present within the Si_3N_4, therefore, densification of high purity Si_3N_4 requires hot-pressing to achieve high densities [57,58].

Work by Gazza indicated Si_3N_4 doped with Y_2O_3 could be hot-pressed to high densities (3.26g/cm^3) comparable to those with MgO additions, but with high temperature strengths due to the formation of refractory phases, such as yttrium silicates, which yields less residual glassy phase at grain boundaries [56,59]. Si_3N_4 materials hot pressed with Y_2O_3 can exhibit poor oxidation resistance at intermediate temperatures. Weaver et. al. [60] showed these problems to be associated with high impurity levels in the Si_3N_4 starting powder. Weaver demonstrated high purity Si_3N_4 with <8% wt. Y_2O_3 to have excellent oxidation resistance, mechanical properties, and high temperature strengths, when compared to Si_3N_4 with MgO additives. Both Y_2O_3 and MgO, however, have shown limited success for pressureless sintering of high purity, low O_2 content Si_3N_4.

Much of the present research involves additions of both Y_2O_3 and Al_2O_3 to Si_3N_4. The addition of Al_2O_3 lowers the glass forming temperature making it possible for pressureless sintering of Si_3N_4 to high densities below the decomposition temperature. Work by Loehman and Rowcliffe [59] with Si_3N_4-Y_2O_3+Al_2O_3 results in shrinkage curves that display the three stages of liquid phase sintering defined by Kingery [20] with one exception. Their results show enhanced shrinkage in the intermediate stage of sintering, which they attribute to improved solid-liquid reactivity due to the phase transition from either α or amorphous Si_3N_4 to β-Si_3N_4 during sintering [59]. By drawing upon the mechanisms of liquid phase sintering, and current research on the $Si_3N_4/Y_2O_3+Al_2O_3$

system, the specific characteristics of Si_3N_4 sintering can be examined. These include properties of the main constituent, such as, impurities, and morphology, along with compatibility with sintering aids and effect on decomposition which can be inferred from mass loss during sintering. Addition of SiC_w will also have an effect on sintering behavior. Generalities which effect all sintering systems, such as particle size and degree of agglomeration have been discussed earlier.

Powder Morphology

Si_3N_4 exists in two crystalline forms, α and β. It has been argued that α-Si_3N_4 is not a true nitride, but an oxynitride with composition $Si_{23}N_{30}O$ [61]. However, evidence also exists showing α-Si_3N_4 to be purely Si_3N_4 [62], with $\approx$ 0.05% 0_2 as an impurity. The relationship between α and β is not well understood, partly due to the fact that the $\beta \rightarrow \alpha$ transformation has never been observed. α appears to be stable at low temperatures and in high Po_2 regions, while β appears stable at any temperature. The structure of the two phases is represented by Figure 6, where β consists of repeating AB layers and α consists of ABCD repeating layers. Because AB and CD are mirror images, $\alpha \rightarrow \beta$ transformation must occur by breaking a Si-N bond and occurs only through a gas, or liquid phase [61]. α-Si_3N_4 is especially suited for sintering because of its higher O_2 content and the fact that it is thermodynamically unstable with respect to β-Si_3N_4 at sintering temperatures [64], which improves dissolution of Si_3N_4 in the liquid phase. Ichicawa [63] reports no improvement in densification as a function of α content, but regardless of whether α content improves densification, it has been shown to improve the final strengths of sintered pieces [64]. If β-

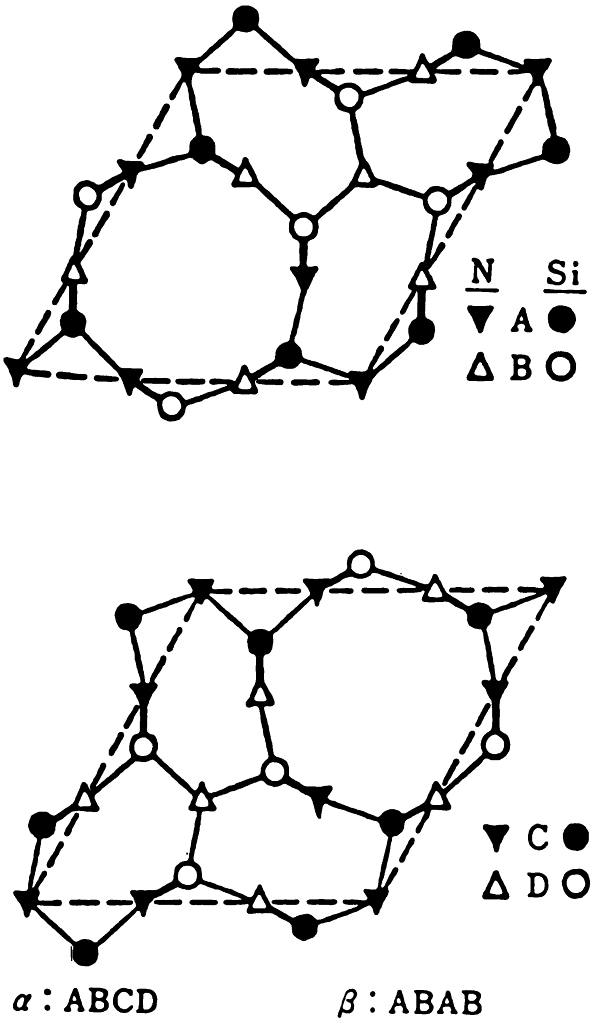

Figure 6 Repeating atomic unit layers for Si_3N_4. Adapted from [63].

grains are present in the starting powder, there will be a continuous growth of globular shaped β at the expense of α, if few or no β grains are present, the liquid phase must first reach a supersaturation to nucleate rod-like β grains.

The mean aspect ratio, $\bar{a}$, of β grains after sintering can be estimated by characteristics of the starting powder ($\bar{a} = 1 + \alpha / \beta$) [55]. High aspect ratio β-grains act as an in-situ form of strengthening the material by crack deflection and additional fracture energy consumption [65-67]. While powders containing pre-existing β, despite their lower green densities, can also be densified, they demonstrate reduced mechanical properties due to their equiaxed microstructure. They are also more sensitive to sintering temperatures as shown in Figure 7.

Impurities in Si_3N_4

Commercial Si_3N_4 is produced by four major processes, nitridation, vapor phase deposition, carbo-thermal reduction, and diimide precipitation [64], each producing a powder with unique sizes, morphology, and impurities. The focus of this study concerns Si_3N_4 powders produced by diimide precipitation. These powders (along with those produced by CVD) have fine particle sizes with very low impurity levels compared to the other powders. Typical grades, such as Ube's E-10, are characterized by submicron equiaxed particles of extremely uniform particle size and morphology [61]. Si_3N_4 produced by diimide precipitation contains trace levels of Cl remaining from the $SiCl_4$ which is not present in the other powders mentioned. Impurities commonly found in Si_3N_4, such as Ca, Na, and K [56], stimulate glass formation at elevated temperatures. Residual levels of carbon act to reduce liquid formation by reacting with oxygen and SiO_2 to form CO or SiO

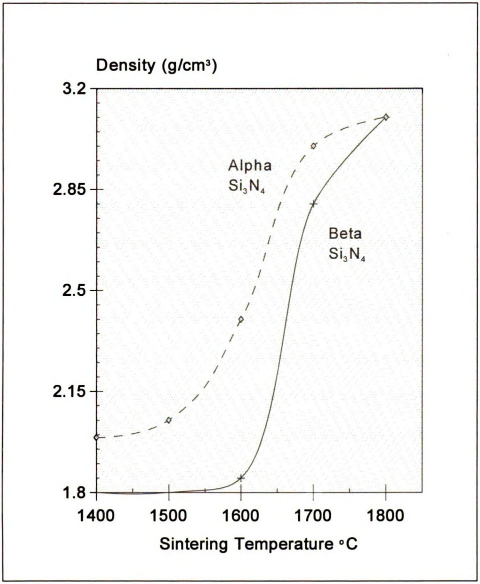

Figure 7 Plot showing the sensitivity of α and β powders to sintering temperature. β powders are more difficult to sinter at low temperatures. Adapted from [64].

which volatilize at high temperatures to reduce sinterability. Other impurities include, Mg, Al, and Fe, which are dissolved by the liquid phase and act to increase the amount and reduce the viscosity of the liquid phase [64]. While these impurities have a positive effect on densification, they have a negative affect on mechanical properties, especially high temperature properties. Therefore, while diimide particles have a lower affinity for liquid production, their mechanical properties should be superior if densification is complete. The most important impurity present in Si_3N_4 is oxygen.

As the amount of sintering aid is reduced, equiaxed powders with high surface areas are needed to produce high densities. Reactions with oxygen present in the form of SiO_2 at the surface and as a solid solution within the α-phase, assist formation of the liquid silicate phase. This is shown in Figure 8. High oxygen contents assist densification of coarser powders, but low oxygen content powders can be sintered to high density as particle surface area is increased [64]. Just as with other impurities, however, the best mechanical properties are found with low O_2 containing powders.

Y_2O_3+Al_2O_3 as Sintering Aid for Si_3N_4

Y_2O_3+Al_2O_3 are the most common sintering aids used with Si_3N_4 because Si_3N_4 is soluble in many of their products and their glassy phases can be crystallized for added high temperature strength [68,69]. Al_2O_3 lowers the softening temperature of oxynitride glasses [59], therefore allowing more effective liquid phase sintering by lowering liquid viscosities and allowing pressureless sintering at temperatures below decomposition. Al is present in the residual glassy phase of sintered specimens, or in solid solution with β- Si_3N_4 as β'-Si_3N_4 which contains Al substitutions for Si and O substitutions for N [44]. Y cannot

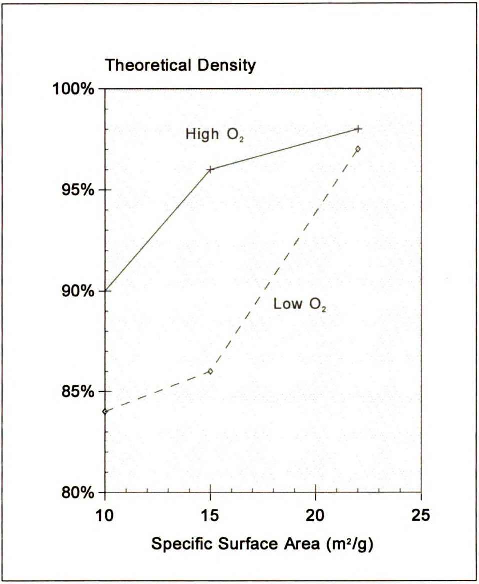

Figure 8 The effect of O_2 content on the densification of Si_3N_4 powders with respect to surface area. Adapted from [64].

replace Si within the β phase, and most of the Y_2O_3 present is found in crystalline grain boundary phases containing no Al. Therefore, Al can be used to lower glass forming temperatures and viscosities, then form solid solutions with β- Si_3N_4 and $YSiO_2N$ thereby reducing the residual glassy phase present after liquid phase sintering.

Oxynitride glasses begin to form within the compact at temperatures as low as 1350°C [59] by reactions of Y_2O_3-Al_2O_3-SiO_2 (SiO_2 found on the surface of Si_3N_4 [70]), as well as N_2 from the sintering atmosphere. At temperatures above 1550°C, Si_3N_4 can dissolve in the molten glasses present and several different second phase glasses and compounds can be formed depending upon the relative amounts of each of the constituents [71].

The dissolution rate of Si_3N_4 is dependent upon particle size and crystallinity. Small (<1 micron) α and β particles dissolve rapidly and reprecipitate in the β form. Due to their relative instability, α particles dissolve more readily forming a supersaturation within the liquid and form idiomorphic rod-like β grains [64]. β present in the starting powder, dissolves under nearly equilibrium conditions and forms spherical β grains [64]. Amorphous Si_3N_4 particles dissolve even more rapidly due to the free energy difference in the amorphous-crystalline transition and they also form rod like β-Si_3N_4 [59]. The driving force for these reactions emanates from free energy differences between reactants and products due to the formation of more stable compounds and reduction of solid-liquid interface.

Because the content of the liquid is continually changing, it is almost impossible to know the composition of the liquid at any given time. Grain boundary phases are difficult to examine after sintering, because they are often too thin to be examined by x-ray or electron probe microanalysis. Loehman [59,71] and Rowcliffe [59] compare relative amounts of sintering additives to a study [71] of oxynitride glasses. By assuming that the oxygen content within the starting Si_3N_4 reflects the SiO_2 content and a moderate residual nitrogen content of 6 at.% [59], predictions can be made about composition and volume percent of second phase present by examining the glass forming region of Y-Si-Al-O-N glasses. Therefore, *relative* levels of additives and O_2 present in the starting powder affects the amount and quality of the liquid phases formed. Increasing amounts of equivalent liquid will increase the densification rate, but generally have little effect on the final density [59]. Cinibulk et al. showed direct addition of YSiAlON glasses allows for more control over residual glassy phases and yielding high sintered densities [44]. Examination of successful Si_3N_4-Y_2O_3-Al_2O_3 sintering systems should provide insight to applying Y_2O_3 and Al_2O_3 to diimide derived Si_3N_4 powders.

Crosbie et al. [42] studied diimide derived Ube E-10 Si_3N_4 with additions of 10 wt.% Y_2O_3 and 2.26 wt.% Al_2O_3 yielding final densities from 2.85-3.19 g/cm^3 (86-96.5% theoretical). They discovered density to be highly dependent upon heating rate from an intermediate hold, as well as on the temperature of intermediate hold. Sintering time proved to be only a minor factor. The highest densities resulted from an intermediate hold at 1700°C with a 600°C/hr. ramp to sinter at 1800°C for 2 hours with a sample mass loss of $\cong$ 0.5% total mass. Ichikawa [63] examined densification of Si_3N_4 as a function of Y_2O_3 and Al_2O_3 content. Sintering at 1750°C for 4 hours and keeping Al_2O_3 content at 2 wt.%, he discovered density to decrease with decreasing Y_2O_3 content for several different powders. The decrease was attributed to a decrease in the amount of liquid causing grain morphology, particle size distribution, and agglomeration to play a more important role in densification. When Al_2O_3 was varied from 1-3wt.%, no changes in density were found. Cinibulk et. al. [44] found optimum densification to occur at 1825-1850°C, but used 1.5 MPa N_2 to minimize decomposition at these temperatures using 5 wt.% Y_2O_3 and 5.5wt.% Al_2O_3 in an effort to form YAG at grain boundaries.

$SiC_{(w)}$ Additions to Si_3N_4

By the same mechanisms acicular β-Si_3N_4 grains in-situ strengthen the matrix, additions of SiC_w can act to strengthen Si_3N_4, but their existence in the starting powder affects sinterability of the composite. Sinterability is reduced by the presence of SiC_w (even if green density problems are avoided) by increasing diffusion distances between solutionizing and reprecipitating Si_3N_4 [72]. Whisker additions have also been shown to inhibit the $\alpha \rightarrow \beta$ transition in Si_3N_4 [58]. Ueno et al. showed this delay to be a function of sintering temperature with the retarding effect becoming smaller with increasing temperature. Therefore, longer sintering times or higher sintering temperatures are required to provide adequate amounts of β to achieve high densities by pressureless sintering. Unfortunately, longer sintering times result in stronger interfacial bonding between matrix and whiskers and toughness is not improved over monolithic values [58].

SiC_w maintain structural integrity during sintering [73] and, therefore, must rearrange to accommodate the shrinking compact. This rearrangement interferes with shrinkage at 20-30 vol.% SiC_w because SiC is insoluble within the liquid phase [74]. Nearly all examples of consolidating Si_3N_4/SiC_w composites involve HIPing or hot pressing along with the addition of liquid sintering additives. Hot pressing of SiC_w composites leads to alignment of whiskers creating an anisotropic material. Densities near theoretical have been reported by hot pressing and HIPing whisker composites [38,39,48]. Grain boundary phases present can have a strong effect on interfacial energies and, therefore, on fracture toughness. Weak interfacial bonding can result in more whisker pullout and crack deflection around whiskers, both of which act to improve fracture toughness. Studies of SiC_w/Si_3N_4 interfaces [48] indicates residual glassy phase can be 5 times thicker around SiC_w than between Si_3N_4 grains. It's suggested that this is due to increased amounts of SiO_2 on the whisker surface which leads to reduced fracture toughnesses due to improved interfacial bonding. Smith et al. [75] showed fracture toughness of whisker toughened alumina was reduced by vacuum hot pressing rather than pressing in Ar due to the presence of O_2 under vacuum conditions. High surface O_2 contents have been shown to degrade high temperature properties of composites during processing or in service unless whiskers were etched or coated to reduce the influence of SiO_2 [48].

Mass Loss (Suppression of Decomposition)

Mass loss is a function of specific surface area and impurities present in the Si_3N_4 powder. Increased surface area provides a greater area over which vaporization reactions can occur. At temperatures $\leq 1850^{o}C$ reactions with SiO_2 and metal oxides account for most of the mass loss in Si_3N_4 [55].

$$Si_3N_4 + 3\ SiO_2 \rightarrow 6SiO\uparrow + 2N_2\uparrow$$

$$Si_3N_4 + 3/a\ M_2O_a \rightarrow 3SiO\uparrow + N_2\uparrow + 2/a\ M_3N_a$$

Mass loss alters the relative amounts of constituents in the liquid phase [55] which can shorten intermediate phase sintering. Mass loss can be reduced by sintering in a powder bed which is more surface active than the Si_3N_4 specimens [49]. Therefore, the preponderance of mass loss will occur at the surface of the powder bed [55]. In general, imide derived powders provide small mass losses due to their high purity and moderate to low oxygen levels. Samples with high mass loss are characterized by open porosity throughout the sintering cycle due to vaporization of constituents from the liquid phase [64].

Sintering Time and Temperature

While the time and temperature trends apparent in liquid phase sintering systems have already been outlined, it is worthwhile to examine specific examples from the Si_3N_4/ Y_2O_3+Al_2O_3 system. Pressureless sintering of Si_3N_4 must occur below 1825°C [34,64] in order to avoid decomposition of Si_3N_4. Some research has shown the benefit of using non-isothermal, [42,43,45] or two stage sintering processes. The two stage process involves a hold above glass forming temperatures before sintering at 1800°C [42,64]. This has been shown to improve densities and reduce mass loss. Few explanations for the success of these criteria have been offered other than extending intermediate stages of liquid phase sintering at the lower hold temperature [42]. This is essential for high purity Si_3N_4 powders because the liquid phase formed will be of higher density (viscosity) and, therefore, sintering will have a greater time dependence.

FRACTURE TOUGHNESS

Determination of K_{IC}

Because ceramics are inherently brittle, their failure is governed by the growth of cracks. A process which is often approximated using linear elastic fracture mechanics [76]. Fracture mechanics is used to determine a materials resistance to fracture relative to the flaw size distribution. Ceramics fracture by the combined effects of acting stresses and flaw severity, which acts to magnify stresses at the crack tip to a point where atomic bonds at the crack tip break [76]. This magnification is measured by the stress intensity factor K_I where the subscript defines the failure mode. Failure occurs at the point where $K_I=K_{IC}$ which is the critical stress intensity factor or fracture toughness. There are many well accepted testing procedures for determination of K_{IC} all with their respective advantages and disadvantages [76]. Measurement of K_{IC} by crack length measurements is a simple and effective method of determining K_{IC} with greater specimen economy. Indentations produced by diamond cone indenters most closely resemble real flaws [76] and yield very reproducible results. A very successful technique for measuring K_{IC} by indentation has been presented by Anstis et al. [77] using Vickers-produced radial cracks.

S. Palmqvist [78] was one of the first to realize indentation cracks could be used to determine hardness and K_{IC} through his work with metal carbides. The idea of measuring K_{IC} for ceramics began with using spherical indenters to induce a hertzian cone crack [76]. The crack front, however, lies entirely underneath the surface of the material and, therefore, is useless for characterization of opaque materials. A Vickers diamond pyramid indenter provides a symmetrical impression for hardness determination and characteristic radial cracks (Figure 9) on ceramic materials which lends itself to reliability and reproducibility [77]. In addition to the radial crack system, a lateral crack is also generated. If indentations are formed with a high load, this crack may begin to interact with the radial system and cause chipping of the indented surface obstructing crack measurement. Therefore, optimal loading should be large enough to produce measurable cracks, but low enough so that chipping is avoided.

Models for the behavior of cracks induced by diamond cone indenters within isotropic homogeneous materials, reveals two components to the forces acting on the crack system, an elastic (reversible) and a residual (irreversible) force. The elastic portion is compressive and the residual portion is tensile. Therefore, cracks grow due to the residual force once the restraining elastic force is removed upon unloading of the indenter. When these cracks are well developed (c>>a) they can be modeled as center loaded half-penny cracks which results in a residual stress intensity factor of

$$K_r = \frac{\chi_r P}{c^{3/2}} \tag{18}$$

where χ_r is a constant which can be approximated by [77]

$$\chi_r = \oint_{R,V} \left(\frac{E}{H}\right)^{1/2} \tag{19}$$

where $\oint_{R,V}$ is a material independent constant for Vickers induced radial cracks and H is the hardness. H is determined by the geometry of the indent and the load applied.

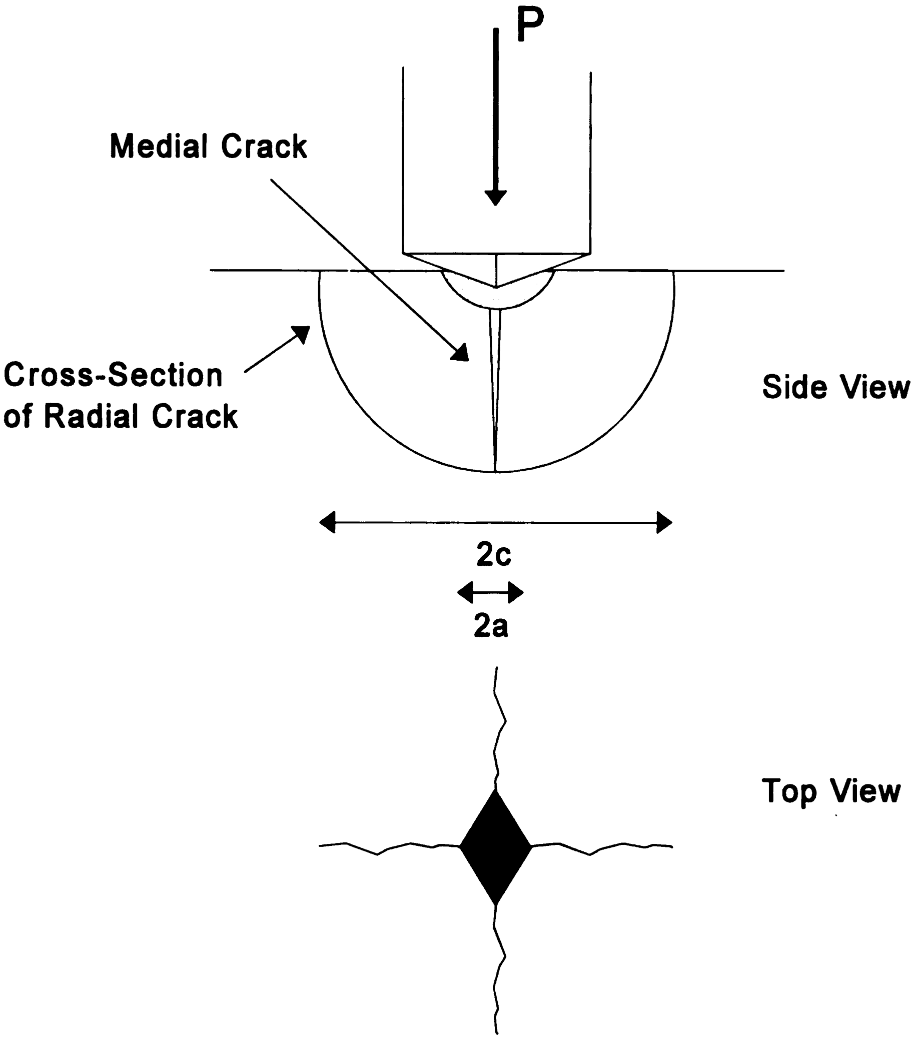

Figure 9 Schematic of Vickers indent technique. Radial cracks result upon unloading and are subsequently measured and related to ceramic hardness and fracture toughness. Adapted from [77].

$$H = \frac{P}{\alpha_o a^2} \qquad (20)$$

Where α_0 =2 for Vickers indenters, and a is taken as the half-diagonal length of the indent. $\oint_{R,V}$ was "calibrated" [77] using existing fracture toughness data for a wide range of materials resulting in $\oint_{R,V}$ =.016+/-.004. By combining these equations K_{IC} can be calculated assuming the radial cracks remain stable in their post-indentation equilibrium configuration; $c=c_0$.

$$K_c = 0.016\left(\frac{E}{H}\right)^{1/2}\left(\frac{P}{c_o^{3/2}}\right) \qquad (21)$$

In the case of many ceramics, however, equilibrium conditions do not prevail. Slow crack effects [77] extend radial cracks beyond c_0 reducing the residual stress intensity factor and diminishing the result below the true K_{IC} value. Therefore, the model above under predicts fracture toughness for most ceramics. Using a similar methodology, Singh et al. [81] developed a formula for calculating K_{IC} for whisker toughened Si_3N_4.

$$K_{IC} = 0.057H\sqrt{a}\left(\frac{E}{H}\right)^{2/5}\left(\frac{c}{a}\right)^{-3/2} \qquad (22)$$

Equation (22) provided results similar to identical specimens tested by double torsion, therefore, the formulation is considered accurate for whisker toughened ceramics.

Other factors can also affect crack stability, such as low H/E values, and materials with open networked structures such as silicate glasses. Material under the indenter may densify, thus reducing the elastic response. Microstructure will also effect indentation results. Fluctuations in c_0 can result from inhomogeneity on a scale >1micron, and as the grain size increases to sizes comparable to the indent size, the fracture pattern can be disrupted by local grain-failures [79].

There has been debate about whether the assumption of half-penny cracks can be made when evaluating fracture from a Vickers induced flaw. In a review of indentation induced cracking in ceramics and glasses by Cook and Pharr [80], they demonstrate a substantial diversity in crack configurations between materials. While the final crack morphology of most "normal" ceramics is that of a half-penny, Cook and Pharr argue that half-penny cracks could not only be formed by radial cracks propagating downward (as Anstis et al. would suggest) but also could coalescence with the median crack formed from beneath the plastic zone under the indenter [80]. In a study by Kaliszewski et al., indents were made through a lead acetate solution to strain the radial and median cracks for SEM study. Examination of Y_2O_3 stabilized ZrO_2 with various toughnesses revealed radial cracks turning toward one another and eventually forming half-penny cracks when a critical load was exceeded [81]. This lends additional validity to the models presented by Anstis et al. and Singh et al.

Experimental application of indentation methods reveals silicate glasses are subject to substantial errors if crack lengths are not measured immediately after indentation. Unlike the silicate glasses, ceramics showed no slow crack growth. This could be due to the fact that ceramics show higher crack velocities relative to K_{IC} than glasses, therefore, crack growth due to factors other than the residual driving force may have already occurred before cracks could be examined.

Overall, indentation methods require knowledge of E, H, and crack-length-to-load data. H and crack-length-to-load data is collected by microscopic evaluation and E can be computed for SiC_w reinforced Si_3N_4 by

$$E = E_o e^{-3.06p} \tag{23}$$

where p is the porosity and E_0 is 297, 310, 323, and 335 GPa for 0-30 v/o SiC_w respectively [82,83]. Testing requires fewer specimens and offers more variability in specimen size, however, the surface must be polished to an optical finish. Materials tested should have a well behaved indentation response, most glasses, softer ceramics, and coarse grained materials should be avoided. Cracks should be well developed ($c \geq 2a$) (therefore, indentation methods don't lend themselves to testing high toughness ceramics, because cracking is by nature less well developed) with no evidence of chipping (lateral crack interaction). Lastly, the test surface should contain no pre-existing stresses prior to indentation.

WHISKER TOUGHENING MECHANISM

SiC whiskers have been added to several CMC systems in an effort to improve fracture toughness [48,66,82,84]. Whiskers are single crystals with a high aspect ratio. When incorporated within a ceramic matrix, whiskers can interact with propagating cracks to slow or alter their progress. The crack requires more energy to propagate, therefore, more energy is required for failure and toughness is subsequently improved. SiC whiskers have seen wide spread application in CMC's and seem to perform better than other materials in service, despite their oxidation at high service temperatures [48]. Experimental studies of whisker toughened ceramics indicate five toughening mechanisms that may operate to increase fracture toughness [48]. These include; crack deflection [66,76,85,86], crack bowing [87], microcracking [67,76,84,88,89], whisker pullout [48,66,90,91] and crack bridging [67,76,92]. While advanced fracture mechanics has been applied to account for toughening due to these mechanisms, there are still arguments over which mechanisms are responsible for the toughening. It is often reasonable to assume that several mechanisms operate in conjunction with one another and the prevalent mechanism is material dependent.

Microcracking

Microcracking can act to improve K_{IC} by relaxing stresses at the crack tip. Relaxation occurs by a reduction in the elastic modulus and by creating a dilatational strain in the microcracked zone surrounding the crack tip [84]. Microcracking is driven by microstructural residual stresses caused by thermal contraction mismatch between randomly oriented grains and between matrix grains and second phase additions. In a study by Evans and Fu [88] they showed toughening due to modulus reduction was maximized in small grain sizes while toughening due to dilatational strains should be maximized at a larger critical grain size. Beyond the critical grain size, some microcracks form thermally, and do not contribute to toughening because they are not a part of the stress-strain hysteresis, in other words, they act to reduce the initial modulus, not the modulus at a propagating crack tip. Experimentation showed toughening at larger grains sizes, but toughening at small grain sizes was not realized. Evans concluded that a discrete microcrack zone could not be sustained at small grain sizes. Another possible explanation involves the grin size dependence on fracture toughness for non-cubic materials such as Si_3N_4 [76]. Non-cubic materials exhibit thermal expansion anisotropy (TEA) which can give rise to local stress that may, in turn, lead to microcracking at grain facets when subject to applied tension. However, these non-cubic systems exhibit toughening over only a narrow distribution of grain size (≅1/2 the critical size needed for spontaneous microcracking) for optimum toughening due to microcracking. Microcracking may work in conjunction with other mechanisms and can result in R-curve behavior as the microcrack zone develops [67,76,89]. Microcracking that occurs upon external loading has been shown to improve fracture toughness by 10% [89]. However, pre-existing microcracks, such as those produced during processing by high cooling rates or grain sizes above those necessary for spontaneous microcracking, show no significant toughening [89].

Crack Bowing

Crack bowing originates from the interaction of a propagating crack with a strong dispersed second phase. The crack front is lengthened by the interaction of two or more second phase particles with the crack there by increasing fracture energy and the strength of the material. However, crack bowing has not been widely reported as a strengthening mechanism in whisker toughened ceramics which may be due to the fact that whiskers are weak when subjected to shear stresses [87].

Crack Bridging

Bridging is distinct from bowing, deflection, and microcracking in that toughening doesn’t occur by interaction with the crack tip, but at a large distance from the tip along opposing crack faces. Toughening due to crack bridging occurs by friction and mechanical interlocking of rough opposing fracture surfaces and ligamentary bridges created by whiskers and elongated grains connecting the fracture surfaces. Bridging is believed to be the major mechanism responsible for $K_{IC} > 12MPam^{1/2}$ in SiC_w reinforced Al_2O_3 composites [93]. This has been confirmed by SEM studies of whisker toughened alumina [87,94]. These bridges of unbroken material act to shield the crack tip from applied stresses. Increased grain size and aspect ratio should increase the degree of toughening due to bridging. The number of bridging sites will also influence toughening and the degree of R-curve behavior expected [76]. Because of this R-curve behavior, whisker toughened ceramics cannot be classified with a single value of fracture toughness. Resistance to crack growth increases as crack length increases due to an increase in the number of traction sites. Therefore, strength is no longer uniquely related to initial flaw size, but is subject to stable crack growth over a range of flaw sizes (below a critical size) as determined by the R-curve and load configuration [67].

Whisker Pullout

While whisker pullout and debonding lengths are smaller than those associated with fibers, toughening from whisker pullout can be estimated from Thouless and Evans' relations derived from fiber reinforced CMCs [90]. How pullout affects toughness is highly dependent upon Weibull Modulus, but is always proportional to pullout length. Typical whisker pullout lengths are from 1-2 micron [94,95]. Pullout lengths, and thus toughening, can be improved by preventing strong bonding between whiskers and the surrounding matrix. Using smooth whiskers to prevent mechanical interlocking along with control over elements present on whisker surfaces, can have a positive effect on pullout. Carbon coatings were shown to improve K_{IC} of 20% SiC_w/Al_2O_3 by 50% [48], but SiO_2 on the surface of SiC whiskers can strengthen interfaces and reduce pullout [96]. Most whisker composites do not appear to show significant whisker pull-out, however, most whisker toughened ceramics do show obvious evidence of crack deflection [66].

Crack Deflection

Crack deflection mechanisms in whisker toughened ceramics arise from residual strain due to elastic modulus or thermal mis-match between phases, or from weak interfacial bonding between phases [86]. Enhancing crack deflection can result in up to a 40% increase in K_{IC} [76]. Crack deflection is evidenced by tilting and twisting of the propagating crack front which effects the strain energy release rate and subsequently toughens the material [66,84]. This effect has been modeled for both 3-D random whisker configurations [86] and 2-D [66] situations where whiskers show preferred alignment, as in hot pressing or slip casting. The 3-D model examined the effect of rod-shaped particles with large aspect ratios (3-12) on the tip of a tilted or twisted crack. It was determined that the crack front twist angle has a much greater effect on deflection toughening than does the tilt angle of the crack tip. The 2-D model predicts greater toughening due to improved crack deflection when the direction of crack propagation is normal to the whisker plane, thus insinuating that whisker alignment imparts greater toughening than a random distribution. Both models also indicate that toughening becomes volume fraction invariant above 20 $^{v}/_{o}$ whisker reinforcement. Therefore, no further toughening can be imparted by crack deflection with greater whisker loadings. Studies by both Faber et al. [86] and Carter et al. [85] show increased fracture toughness as median crack deflection angles increase. The increased degree of crack deflection is also evident by a roughening of the fracture surface [76]. Crack deflection is not due solely to the presence of whiskers. Monolithic ceramics exhibit crack deflection which is dependent on grain shape. This makes the SiC_w contribution to crack deflection difficult to determine for Si_3N_4 because Si_3N_4 already exhibits a great deal of crack deflection due to elongated β-grains [86]. Therefore, if the β-grain aspect ratio were reduced by decreased sinterability from SiC_w additions, toughness could theoretically decrease.

EXPERIMENTAL PROCEDURE

Starting Materials

Particle sizes and impurities as well as other useful information is listed in Table 3.

Table 3 Purity, particle size, and surface area of starting ceramic powders.

Components	Si_3N_4	SiC_w (99.0%)	Y_2O_3 (99.99%)	Al_2O_3
N	>38.0%wt	N/A	N/A	**Si** $\leq$ 40 ppm
O	1.35%wt	N/A	N/A	**Na** $\leq$ 10 ppm
Cl	<100(ppm)	N/A	N/A	**Mg** $\leq$ 10 ppm
Fe	<100(ppm)	0.05%	<0.005	**Cu** $\leq$ 10 ppm
Ca	<50(ppm)	0.05%	<0.005	**Fe** $\leq$ 20 ppm
Al	<50(ppm)	0.08%	<0.005%	N/A
% Crystal	>99.5	N/A	N/A	N/A
% $\beta/(\alpha+\beta)$	<5.0	100	N/A	100% α
SSA (m^2/g)	11.6	2-4	N/A	6-10
Aspect Ratio	1	10-40	1	1
Diameter (mm)	0.5	0.3-0.6	1.0-3.0	0.3
Length (mm)	N/A	5-15	N/A	N/A
Density (g/cm^3)	3.22	3.20	5.01	3.98

Starting ceramic powders were selected from various manufacturers. Si_3N_4 from Ube Industries, grade SN-E10, SiC whiskers from Tokai Whisker, grade TWS-100, were the major constituents that made up the composite, and Y_2O_3 from Rhone-Poulenc, and Al_2O_3 from Sumitomo Chemical, grade AKP-50, were used as sintering aids.

Particle Sizing

Testing began with a particle size analysis of the as-received Si_3N_4 and SiC whisker to confirm manufacturer's reported particle sizes and to determine relative particle sizes as a function of pH. The Andreason Pipette method was chosen to determine particle sizes [97]. This method is based upon Stoke's Law, the principal law of sedimentation of particles in a fluid, which states that larger (heavier) particles will sediment (fall through a fluid medium) faster than smaller particles under the force of gravity. Slurries of Si_3N_4 and SiC whisker were prepared in 10^{-4}M KNO_3 electrolyte (prepared with deionized water) to simulate processing conditions. Each suspension was ultrasonicated for three, 5 minute cycles to disperse any pre-existing agglomeration. This was repeated for each slurry over a pH range of 2-11. The pH values were adjusted by adding appropriate amounts of HNO_3 (acid) and KOH (base). All acids, bases and salts used were of reagent grade or better. The slurry was subsequently placed in a 500ml graduated glass cylinder and shaken by hand for two minutes. The suspension was then allowed to sediment. Samples of 15ml were extracted from the slurries at 3, 10, 60, 120, 240 minutes and for longer periods when needed, into weighed and marked 50ml glass beakers. The beakers were placed into a furnace at 120°C for 24 hours to evaporate the water, and the beakers weighed a second time. Maximum particle diameters were determined as a function of suspension medium viscosity and density, settling distance of particles over a given time, density of particles, and acceleration of gravity using Stoke's Law.

$$d = \sqrt{\frac{18h\eta}{g(D_1 + D_2)t}} \tag{24}$$

where:

d= diameter of coarsest particles which remain in suspension at a depth below h (cm) and at a time t (sec)
η= liquid viscosity (η_{water}= 0.00818 poise)
h= height (cm)
D_1= density of the particles (g/cm^3)
D_2= density of liquid (D_{water}=0.996 g/cm^3)
g= acceleration of gravity = 980 cm/s^2
t= time (sec)

Representative particle sizes from each pH tested were determined from the time when 50% of the particles in suspension were under sized. This was calculated by the following relationship.

$$\%Undersized = \frac{W_1 V_2}{W_2 V_1} * 100\% \tag{25}$$

where:

W_1= weight of solids in sample withdrawn
W_2= weight of total solids in cylinder at time of sample drawing
V_1= volume of the sample drawn
V_2= volume in the cylinder at the time of drawing

A correction factor for the asymmetric effects of the SiC_w falling through an aqueous medium under the effects of gravity [98] was included in the calculation of an equivalent spherical diameter to characterize the whisker agglomerate size. Once particle size values were determined as a function of pH, further sedimentation experiments were conducted to characterize the behavior of Si_3N_4 and SiC_w suspensions as a function of pH.

Sedimentation

A 400ml suspension of either Si_3N_4 or SiC_w was prepared at 10^{-4}M KNO_3, brought to pH 2 and ultrasonicated for 3 five minute cycles to simulate processing conditions. Upon which, 20ml was drawn off and placed into a test tube. The tube was shaken by hand for 2 minutes and then allowed to sediment for several days. Suspension densities were subsequently measured to estimate the degree of agglomeration as a function of pH. This experimental stability was then compared to stability estimates from ζ-potential data. ζ-potential curves were generated from data determined by Electrokinetic Sonic Amplitude (ESA) testing.

ESA Testing

ESA curves were determined using 220ml slurries of 0.5 $^v/o$ solids in 10^{-4}M KNO_3 electrolyte. The pH of each suspension was lowered to pH 2 with HNO_3 and ultrasonically dispersed for five 3 minute cycles to remove any pre-existing agglomeration. ESA curves were generated using a computer controlled Matec 8000 ESA system equipped with an autotitrator, overhead stirrer and probes for pH, temperature, and conductivity. This system uses O'Brien's [8] theory of electro-acoustic effects in dilute suspensions of spherical particles to calculate the suspension ζ-potential from the measured ESA signal. These theories are valid if; (1) the suspension is $<10^v/_o$, (2) the electrical double layer is thin relative to the particle radius ($\kappa a>50$), and (3) the standard deviation of the particle size is < 20% the mean particle size. SiC_w do not meet the final criteria, therefore, electrochemical data collected from the whiskers will be more subjective.

A 1 MHz electrical field is applied to the suspension which generates a sound wave at the electrode surface. The pressure amplitude of the wave (electrokinetic sonic amplitude) and the phase angle relative to a standard of known polarity (10 $^v/_o$ Ludox) were measured. For suspensions meeting the three criteria stated above, the ESA signal is proportional to the density difference between solid particles and the liquid phase, solid volume fraction, and the dynamic (frequency dependent) electrophoretic mobility [8]. Under these conditions, dynamic mobility is approximately equivalent to the electrophoretic mobility and is therefore related to the potential at the shear plane, or ζ-potential. Using this technique to characterize the behavior of ceramic powders has been validated in a number of studies [6,8]. Slurries were subjected to base titration over a range from pH 2-11. The ESA data for Si_3N_4 powder and SiC whisker was collected by two different methods. The first method using the manufacturer's reported particle size over the entire pH range, and the second method was a point-to-point determination of the ESA using the varying particle sizes determined by the Andreason Pipette method. Both techniques yielded similar curves with identical i.e.p.s (iso-electric points). The point-to-point method resulted in nearly the same curve with increased intensity of the zeta potential values due to a higher size correction factor caused by the increased agglomerate size. It was decided to use the conventional ESA curve with a singular particle size because more is known about how to interpret these curves (i.e.: homostability at approximately 25mV) [99] and the additional agglomerate size information didn't change the inherent shape of the curve. ESA testing was conducted on Al_2O_3 and Y_2O_3 sintering aids to estimate their homostability as a function of pH. ζ-potential results could not be collected for Y_2O_3 however, due to solubility in acidic solutions. This has a substantial effect on processing conditions which will be discussed in more detail later. The calculated ESA and particle size values along with Hamaker constants for Si_3N_4 and SiC were input into *Suspension Stability*©, a computer program developed by Wilson and Crimp [10] to predict the stability of composite colloidal suspensions by applying the modified version of DLVO/HHF theory discussed earlier.

Stability Calculations

Hamaker constants for each component were determined by a simplified Lifshitz method developed by Bleier [4] for particle interactions in a vacuum. Because these ceramic components are interacting in an aqueous medium, an effective Hamaker constant is determined which subtracts out the effects of molecules from the medium altering the interactions of the composite particles. Results from *Suspension Stability*© revealed three different regions of relative stability between Si_3N_4 and SiC_w at pH 3, 6, and 11. Colloidal CMC processing began by comparing how these changes in pH affected suspension parameters and green densities.

Suspension Preparation

Sample processing was carried out by freeze-drying composite colloidal suspensions followed by consolidation and sintering of the green bars. Ceramic suspensions were produced by first preparing a 10^{-4}M solution of KNO_3 and adjusting that solution to the desired pH with either HNO_3 or KOH. The appropriate amount of Si_3N_4 was added to the electrolyte and the pH adjusted to return the suspension to the processing pH. SiC_w were added in varying percentages (10 and $20^{v}/_{o}$) and the pH again corrected. Some

Si_3N_4 slurries were ball-milled for 24 hours before the addition of SiC_w to reduce the number of hard agglomerates present in the as-received powder [100]. Ball-milling was carried out in 250ml Nalgene bottles containing alumina grinding media. Total ceramic powder additions to the process slurries form a 5:1-7:1 ratio of electrolyte to solids. This has been shown to be an optimum range for freeze-drying ceramic powders [16]. Y_2O_3 and Al_2O_3 are added to the composite suspensions to promote liquid phase sintering [42,64] at weight percentages of (4%, 2%), (6%, 2%), and (8%, 2%) respectively. Sintering aids were added to Si_3N_4 suspensions prior to the ball-milling step to improve mixing with the Si_3N_4 and to reduce particle size of the Y_2O_3. Addition of sintering aids offered no change to suspension pH at pH 11, however, Y_2O_3 is soluble in aqueous acid solutions [101] and will consume the acid additions to the suspension until it is completely dissolved in the suspension. Composite suspensions of Si_3N_4/SiC_w were ultrasonically dispersed for 3 cycles at five minutes each and pH adjusted at the end of each cycle. Ultrasonication was performed in an ice bath to ensure that changes in pH were due to forming of new surface area from splitting soft agglomerates and not due to temperature changes. After the slurries were ultrasonically dispersed, they were poured into 300ml glass vessels to be freeze-dried.

Freeze-drying

The vessels were stoppered and placed on rollers in a methanol bath at $-40^{o}C$ for 30 minutes. Shell freezing the suspension to the walls of the vessel for more efficient freeze-drying [18]. The frozen suspension is then introduced to a vacuum of < 2kPa and the condenser is dropped to $-50^{o}C$ to promote sublimation of the frozen water from the suspension. The freeze-drying process is complete when the exterior of the vessel reaches room temperature (approximately 12 hours). Secondary drying was not carried out. Freeze-drying has a distinct advantage over mechanical mixing of powder and whiskers because of the added control of agglomeration invoked by colloidal manipulation. Soft agglomerates formed during freeze-drying were removed by agitation (30 minutes either by hand, or by very low speed ball mill) in a Nalgene bottle containing 3 alumina cylinders used as grinding media in the previous ball-milling step. Once soft agglomerates were removed (visual inspection), the powder was uni-axially pressed to form specimen bars.

Uni-axial Pressing

Near-net shaping of freeze-dried Si_3N_4/SiC_w composite powder was accomplished by first cold uni-axially pressing the dry powder in a steel double action die (65mm x 6mm x 15mm) at 15MPa. The die cavity was filled with powder and vibrated for 15 seconds to promote uniform settling of the powder within the die. The level of powder in the die was then topped off and subjected to vibration a final time. Force was applied to the die by a Model C Carver Laboratory Press. Further consolidation of the green specimens was accomplished by cold isostatic pressing (CIPing).

CIPing

Specimens were relatively fragile after low pressure uni-axial pressing and require further consolidation for greater green strength. This was accomplished by CIPing at 250MPa (35,000psi). The CIP used was a model produced by Iso-Spectrum. Specimens were vacuum sealed in latex bags to protect them from the pressurizing fluid. Bagged specimens were placed in a basket and immersed in a mixture of water and anti-freeze within the pressure vessel. Pressure is applied by an air driven pump which delivers more fluid into the vessel thus raising the pressure within. Top pressure was held for 2 minutes and released over the course of 30 seconds by hand. Upon completion of CIPing, specimen bars were subsequently weighed and dimensioned using calipers to calculate green densities.

Sintering

Composite green specimens were sintered in an Astro 1000-S 4560 graphite resistance furnace by Thermal Technologies in an atmosphere of flowing nitrogen. Flow was monitored by the consistent flow of emission gasses through silicon oil. Sintering began from room temperature to 1100°C under vacuum conditions. A N_2 pressure of 70 kPa was maintained in the furnace chamber above 1100°C. Furnace temperature was controlled by two methods. The furnace is equipped with a computerized controller attached to a BGT-2 thermocouple (graphite vs. boron-doped graphite) supplied by Thermal Technologies. Temperature was also monitored with an optical pyrometer sighted through a quartz window port to ensure accuracy of temperature measurement. Specimen bars were packed in a 70 vol.%BN/30 vol.%Si_3N_4 powder bed to minimize weight loss during sintering [49]. Specimens were then sintered under varying schedules to evaluate how changes in sintering time and temperature affect density, microstructure, and relative α/β content.

Density Measurements

Densities of sintered ceramic specimens were determined by ASTM C 373-88 [102]. This method is similar to Archimedes principle in that it involves the comparison of wet and dry weights, but employs techniques that allow for more successful detection of surface porosity. A digital balance was used to weigh specimens, and evaluate specimens suspended in water.

Microstructural Evaluation

Specimens were prepared for microstructural evaluation by first removing 0.5mm from the surface with a high-speed diamond saw. The exposed surface was then polished with either a series of graded SiC polishing papers and varying sizes of alumina suspensions down to 0.05 micron or diamond slurries of 10, 6, and 1μm respectively. Polished surfaces were examined by optical microscope, and subsequently gold coated for examination by SEM. Gold coatings were applied by DC sputtering to all specimens under a partial pressure of argon. Each specimen was coated for 3 minutes yielding an approximately 30nm thick coating of gold on the polished surface. The specimens were examined in an Hitachi 4500-S SEM.

Characterization of Crystallinity

X-ray diffraction with a Scintag model 2000 XDS diffractometer was used to determine the crystalline phases present in densified samples. Cu k_α radiation was used in 0.03° steps through 20-50° 2θ to create X-ray diffraction peaks for characterization of α/β ratio in Si_3N_4 and crystallinity of sintering aids. Samples were either sectioned or surface layers were ground to prevent surface layers from effecting results. Relative amounts of α and β can be calculated from the following relationship [52],

$$F_\alpha = (1.898)\frac{I_{\alpha(102)} + I_{\alpha(210)}}{1.898\left(I_{\alpha(102)} + I_{\alpha(210)}\right) + \left(I_{\beta(102)} + I_{\beta(210)}\right)} \tag{26}$$

however, peak heights can be used instead of computing integrated peak intensities for use in equation (26) [103]. This simplification is valid for Si_3N_4 ceramics because peak broadening is small for brittle materials and also appears to be constant over the appropriate range of 2θ for Si_3N_4 [103].

Determination of K_{IC}

Fracture toughness values were evaluated by the previously described indentation technique [82]. Sintered samples were sectioned and polished to 1μm diamond paste and indented using a Buehler Vickers indenter. Indents were made using varying loads from 100-200N. Indents were positioned to create cracks along both the longitudinal and transverse axis of the specimens. The Buehler indenter is equipped with an optical microscope for immediate evaluation of crack lengths and the measuring apparatus is sensitive to 0.1μm. Indented surfaces and fracture surfaces (created in a three-point-bend fixture) were subsequently prepared for SEM examination to characterize toughening mechanisms.

RESULTS

Colloidal Optimization

As the pH of a particle suspension changes, surface characteristics of the powder in suspension may also change giving rise to either an increase or a decrease in surface potential. This change in potential will alter the attractive and repulsive forces between the particles in suspension and determine the stability of the suspension. When attractive forces dominate, individual particles agglomerate to form larger particle bundles which settle out of suspension. Therefore, when Si_3N_4, or any ceramic powder, is in suspension at any pH other than its stable pH, it will behave as a system of agglomerates much larger than the reported particle size.

Particle Sizing

The average particle size, or observed agglomerate size, was determined for Si_3N_4 as a functicn of pH using the Andreason pipette method (Figure 10). Results indicate observed particle sizes vary with changes in pH. The largest agglomerates were formed at pHs from 2-8 with sizes well above the reported manufacturers particle size of 0.3μm. Therefore, the flocculation of Si_3N_4 in aqueous suspension is clearly effected by the suspension pH. Only at pH 2 and 9-11 is it possible for Si_3N_4 to be present in suspension with little or no agglomeration.

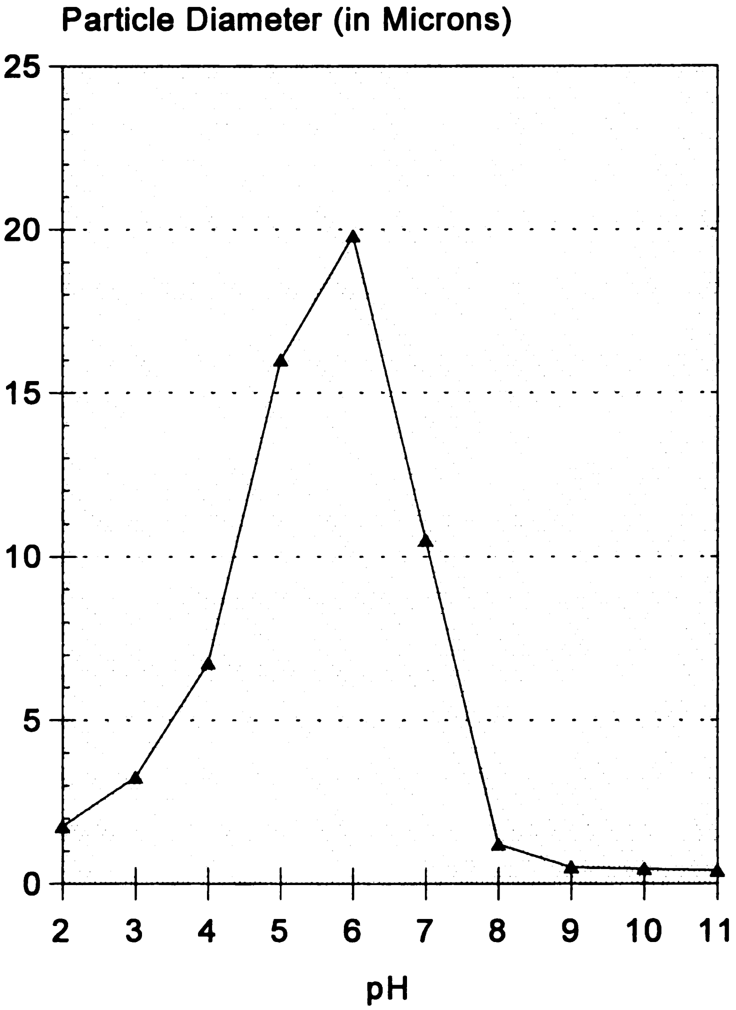

Figure 10 Average agglomerate size vs. pH for as-received ultrasonicated Si_3N_4 powders as determined by Andreason Pipette Method.

Sedimentation

Sedimentation of both Si_3N_4 and SiC_w powders revealed improved powder packing with increased suspension stability (Figure 11). With an increased degree of stability, the effective particle size in suspension is reduced (as shown previously). Therefore, when suspensions of varying pH are allowed to sediment, those suspensions that are the most stable will sediment slower and to a higher density than unstable suspensions. The pH at which the highest sedimentation densities occur is pH 2-3 and 10-11 with Si_3N_4 showing a 4-fold increase in density and SiC_w a 2-fold increase at pH 11 and a small increase in density at pH 2.

Sedimentation and agglomerate size results provide physical evidence against which to compare theoretical results obtained through ζ-potential testing and stability prediction calculations performed using DLVO/HHF theory.

ESA Testing

ζ-potential results obtained by ESA as a function of pH, for Si_3N_4 and SiC_w are shown in Figure 12. As defined by Stern theory, ζ-potential data can be used to approximate the surface potential of particles in suspension and thus the repulsive forces responsible for suspension stability. Because van der Waals forces (attractive forces) will not change as a function of pH, ζ-potential can be used to estimate stability. Hunter [99] estimates the minimum potential required for stability in most systems to be between ± 25-50mV. Using the lower bound for the results in Figure 12, Al_2O_3 should be stable in an acidic environment, while Si_3N_4 and SiC_w are very near the minimum potential for stability. It is important to mention that this estimate does not account for any variation in particle

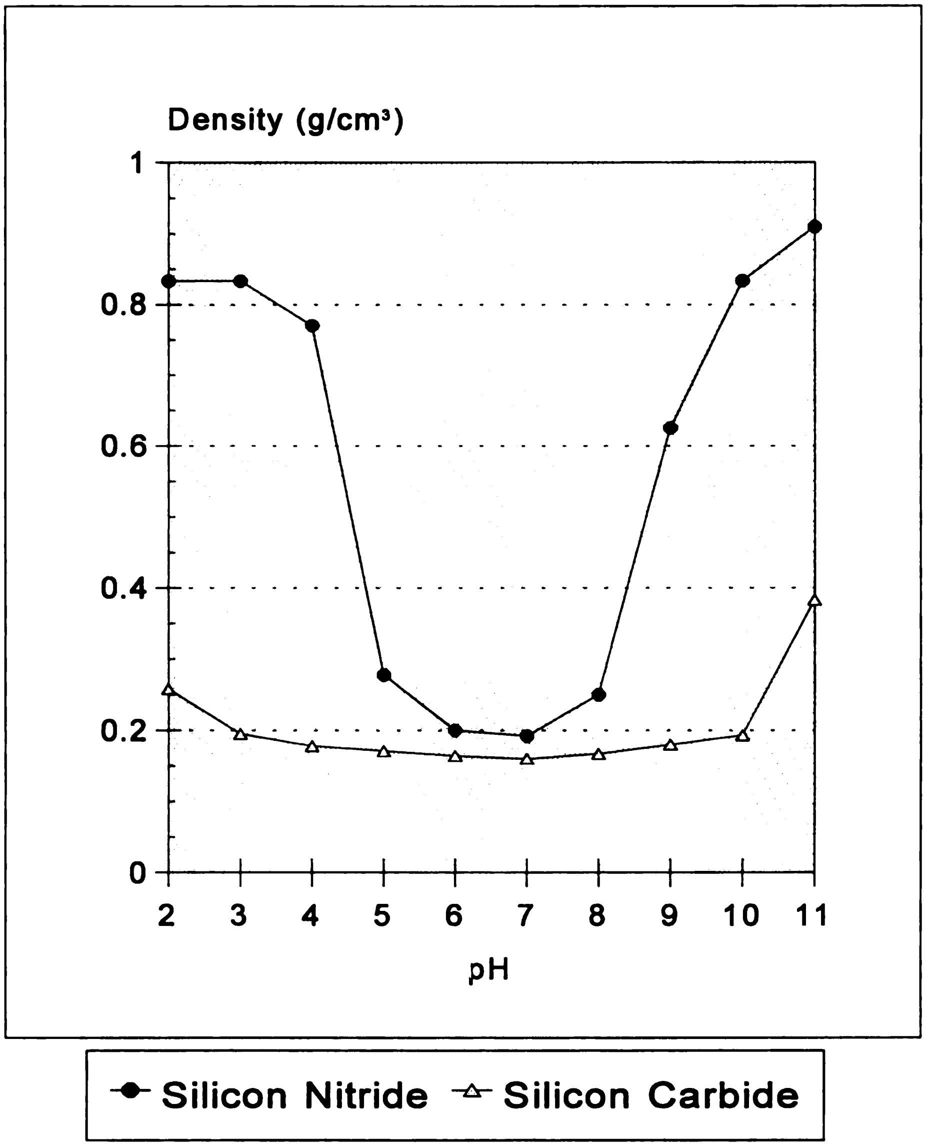

Figure 11 Sedimentation density vs. pH for as-received ultrasonicated Si_3N_4 and SiC_w.

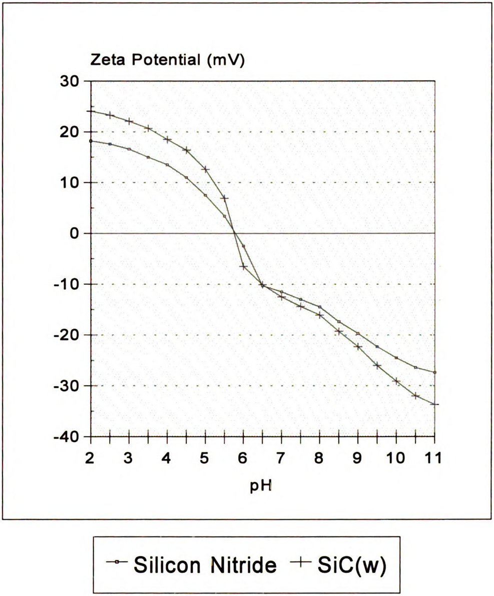

Figure 12 Zeta-potential vs. pH for as-received ultrasonicated Si_3N_4 and SiC_w as determined by ESA.

size. If a particle is large (>1 μm), the charge is spread over greater area, the force of gravity on the particle is greater, and because van der Waals forces are treated in an additive manner, the attractive forces will be stronger. Therefore, it is more likely that Si_3N_4 will be stable at pH 2 compared to SiC_w due to the larger size of the SiC_w and increased surface area. The basic side of Figure 12 indicates Si_3N_4 and possibly SiC_w could be homostable (i.e.: stable with respect to itself) while the homostability of Al_2O_3 is unlikely. At a neutral pH, applying the approximation indicates that neither of the components would be homostable and all three components would agglomerate. While ζ-potential data is a convenient way to estimate homostability, it alone is not enough to estimate interparticle interactions between different components. DLVO/HHF theory can be applied using the ζ-potential results to estimate stability between different components in suspension.

Stability Calculations

Stability calculations were modeled using *Suspension Stability*©, as developed by Wilson and Crimp [10]. Stability calculations were completed for interactions between Si_3N_4/SiC_w, the results of which are shown in Figure 13. Hunter [104] defines the behavior of colloids with $\boldsymbol{W}$ values from 1-20 as marginally stable. Therefore, a conservative measure of stability could include values of $\boldsymbol{W} > 20$ as stable. Table 4 indicates relative stability between components as predicted from the stability plot of Figure 13 by assuming $\boldsymbol{W} > 20$ is indicative of relative stability.

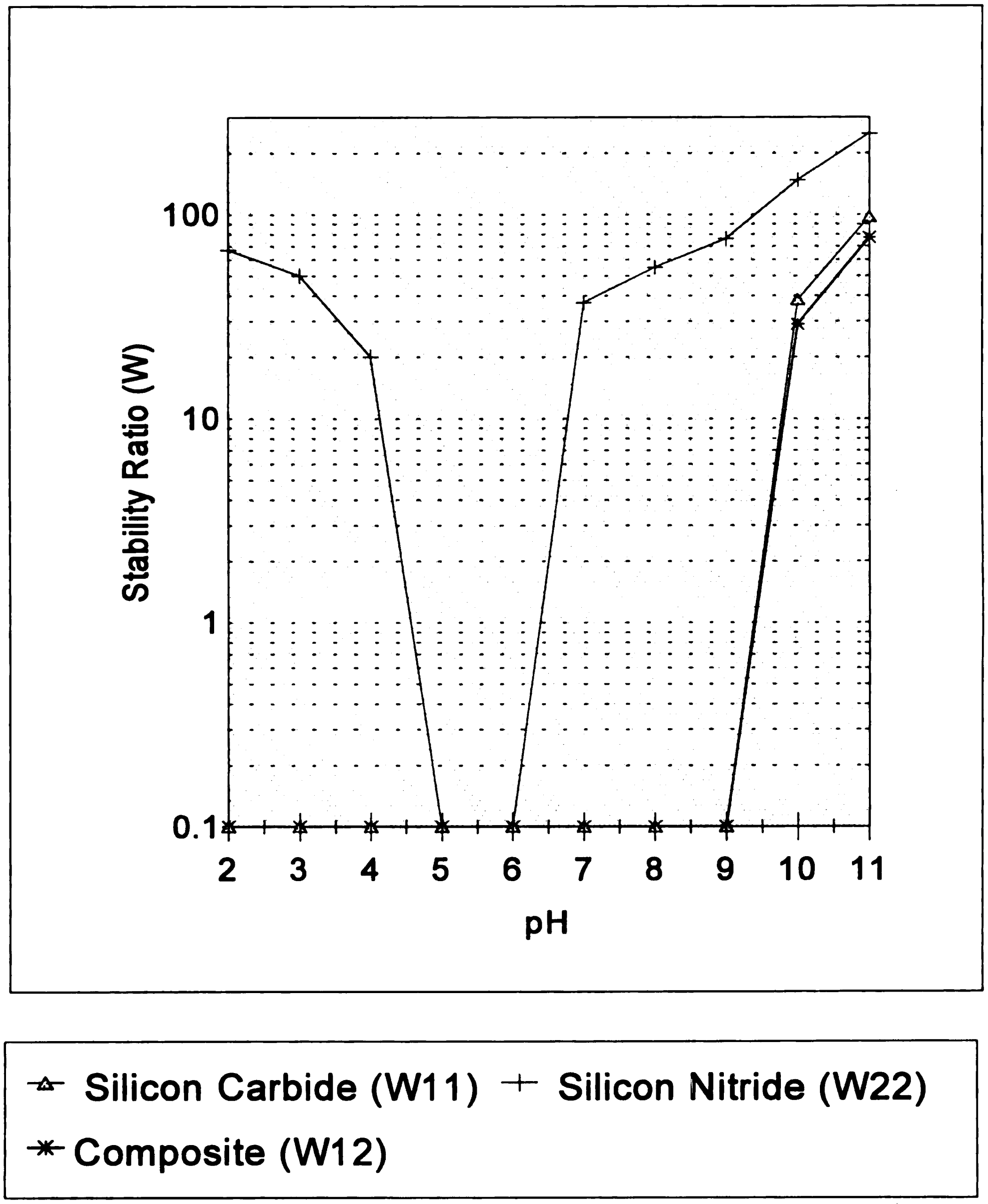

Figure 13 Stability Ratio vs. pH for as-received ultrasonicated Si_3N_4 and SiC_w.

Table 4 Range of homostability and heterostability for SiC_w/Si_3N_4 composite system as predicted by Suspension Stability©.

Stability Ratio ***W***	Si_3N_4/Si_3N_4 Interactions	SiC_w/SiC_w Interactions	Si_3N_4/SiC_w Interactions
Range of Predicted Stability	pH 2-4 and pH 7-11	pH 10-11	pH 10-11

Freeze-dried powders

While colloidal forces determine the relative particle sizes in suspension, the final agglomerate sizes of freeze-dried powders is quite different. Large soft agglomerates form upon freeze drying yielding particle sizes much larger than the colloidal agglomerate sizes, usually ≥ 50 μm (Figures 14-19). SEM micrographs and tap densities reveal the effect of pH and ball-milling on freeze dried powders. Processing without the addition of acid or base (pH 7.5) yields finer freeze-dried particle size as revealed by SEM analysis (Figures 14-16) and by tap densities Table 5.

Table 5 The effect of processing pH and ball-milling on the tap densities of freeze-dried powders. Powders include 8% wt. Y_2O_3 - 2% wt. Al_2O_3 as sintering aids. Values listed are in g/cm^3.

Si_3N_4 Suspension	pH=3	pH=7.5	pH=11
Ultrasonicated	0.70	0.92	0.85
Ultrasonicated & Ballmilled	0.88	1.03	1.00
Ultrasonicated & Ballmilled with 10 $^v/_o$ SiC	0.63	0.85	0.945

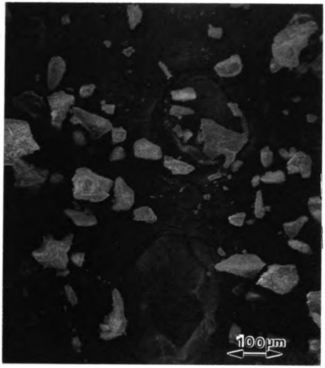

Figure 14 Freeze-dried, ultrasonicated and ball-milled Si_3N_4 powders processed at pH 3 with sintering aids.

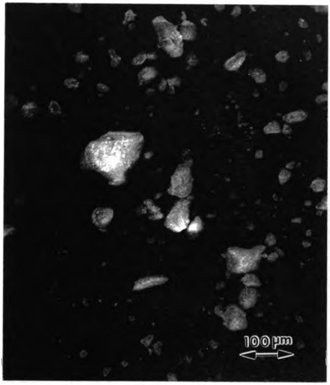

Figure 15 Freeze-dried, ultrasonicated and ball-milled Si_3N_4 powders processed at "natural" pH (7) with sintering aids.

Figure 16 Freeze-dried, ultrasonicated and ball-milled Si_3N_4 powders processed at pH 11 with sintering aids.

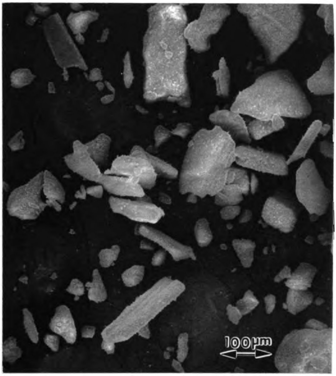

Figure 17 Freeze-dried and ultrasonicated Si_3N_4 powders processed at pH 11 with sintering aids.

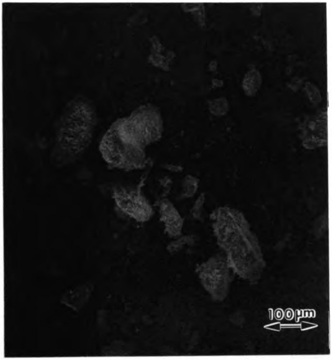

Figure 18 Freeze-dried, ultrasonicated and ball-milled $20^v/o$ SiC_w/Si_3N_4 powders processed at pH 11 with sintering aids.

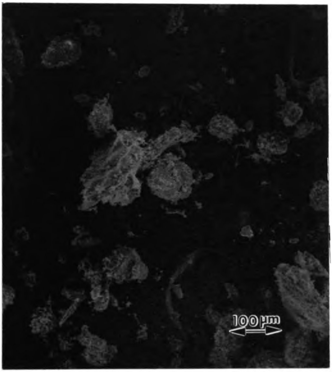

Figure 19 Freeze-dried ultrasonicated and ball-milled $20^{v}/_{o}$ SiC_w/Si_3N_4 powders processed at pH 11 with sintering aids. SiC_w added after milling.

Although colloidal studies show pH 7.5 to be a region of agglomeration, the effect of the dissolution of Y_2O_3 must also be considered. The dissolution of any constituent phase into the suspension could effect the surface charge on particles in suspension and hence the stability.

SEM micrographs show ball-milling to have a small effect on particle size and morphology. Particles appear smaller on average with a more rounded shape and a tighter size distribution as shown in Figures 16 and 17 for monolithic powder dispersed at pH 11. This may be due to a smaller size distribution of primary particles created by ball-milling. As a function of pH, particle sizes appear smallest at pH 7.5 with ball-milling. This is confirmed by tap density measurements where pH 7.5 yields the highest tap density. While pH 7.5 yields the highest tap density for monolithic Si_3N_4, pH 11 shows the highest tap densities for the composite powder (Table 5). This is due to the instability of SiC_w at $pH \leq 10.5$ as demonstrated by the stability prediction in Figure 13. Processing at pH 3, on the other hand, shows poor tap densities with the addition of SiC_w. While SiC_w should be relatively stable at pH 3, Y_2O_3 is chemically unstable and will dissolve in suspension [101,105] during ultrasonication and ball-milling. Subsequent precipitation of metallic Y^{3+} complexes on the Si_3N_4 surface [101] yields a harder powder upon freeze-drying.

Pressing characteristics of all powders were relatively consistent with the exception of powders containing $\geq 20\ {}^{v}/_{o}$ SiC_w loading. These powders tended to delaminate after uni-axial pressing and pH 3 powders produced extremely warped specimens upon CIPing. This is due to the hard agglomerates formed during processing at pH 3.

Selected component milling of pH 11 powders revealed reductions in tap density with whisker loading (Table 6). Composite powders were processed at pH 11 due to their higher tap densities and consistent powder quality. Milling of all components yielded the best tap densities, while milling of Si_3N_4 alone improved densities more than milling of whiskers alone. Therefore, deagglomeration of Si_3N_4 is important for improving the packing of freeze-dried powders. This is further demonstrated by the fact that the 10 $^v/_o$ SiC_w ball-milled powder shows a higher tap density than does unmilled monolithic Si_3N_4. The addition of 20 $^v/_o$ SiC_w had a major effect on tap densities (Table 6). The increased interparticle friction will act to lessen green densities and reduce rearrangement during liquid phase sintering thus reducing the sintered density. Figures 17 and 18 show increased surface roughness of freeze-dried powders with 20 $^v/_o$ SiC_w. The advantage of ball-milling SiC_w can be seen by a reduced surface roughness of the powder.

Table 6 The effect of whisker loading and selected component ball-milling on tap densities of powders freeze-dried at pH=11 with sintering aids. Values listed are in g/cm^3.

Si_3N_4 Suspension	Monolithic Si_3N_4	10 $^v/_o$ SiC-Si_3N_4	20 $^v/_o$ SiC-Si_3N_4
All Components Ballmilled	1.00	0.94	0.76
Only Si_3N_4 Ballmilled	1.00	0.89	0.70
Only SiC_w Ballmilled	0.85	0.75	--

Green Density

Green densities were measured as a function of both whisker loading and pH. Green specimens were first prepared without sintering aids from ultrasonicated suspensions. The resulting green densities of uni-axially pressed specimens were determined as a function of pH. Results show the highest green densities for composite specimens at pH 11 where there is heterostability and homostability of both constituents in the composite suspension (Table 7). The trend in green density results is due to whisker stability, good at pH 11, fair at pH 3, and poor at pH 6, as shown by sedimentation as well as ζ-potential and ***W*** results. Monolithic specimens show the highest density at pH 3 and 11 where Si_3N_4 is stable. CIPing at 350MPa resulted in an increase in green densities, but the relative difference in green density as a function of pH did not change. Green density as a function of $^v/_0$ whisker content was also analyzed. In general, green densities decrease with whisker loading as whiskers increase interparticle friction and reduce rearrangement during cold pressing [106]. Scatter in the data is at a maximum for specimens with 10 $^v/_0$ whiskers. This is due to the fact that delamination of

Table 7 Green density as a function of pH and whisker loading (g/cm^3).

Whisker Loading	Processed at pH 3	Processed at pH 6	Processed at pH 11
0%	1.33 +/- .005	1.27 +/- .005	1.32 +/- .005
10%	1.21 +/- .015	1.22 +/- .015	1.28 +/- .015
20%	1.24 +/- .016	1.15 +/- .01	1.27 +/- .008
30%	1.11 +/- .013	1.14 +/- .013	1.18 +/- .01

the green specimens [107] begins to occur at 20 $^{v}/_{o}$ SiC_w, therefore, only the best specimens are suitable for evaluation, thus seeming to reduce inconsistencies in the data. Specimens at 30 $^{v}/_{o}$ SiC_w were difficult to produce at all pHs. CIP densities are not presented for specimens without sintering aids due to inconsistencies in pressing pressure during testing. These results demonstrate the dependence of green density on colloidal stability. Freeze-dried powders pack to higher densities when they are produced from more stable suspensions for both the monolithic and composite systems. This is due to improved homogeneity and smaller mean agglomerate sizes under suspension conditions.

Tables 8 and 9 show how green densities were affected by the addition of sintering aids. Composites were not processed at pH 3 or 7 without ball-milling due to incomplete sintering of specimens reinforced with as-received whiskers. Green densities without ball-milling seem to follow the same trends seen before the addition of sintering-aids with green density being the highest at pH 3 and 11 and decreasing with whisker loading. Table 9 shows the effects of ball-milling on green density. Ball-milling of suspensions increases

Table 8 Green densities of specimens CIPed at 250MPa with 8 wt.% Y_2O_3 / 2 wt.% Al_2O_3 added as sintering aids.

Whisker Loading	Processed at pH 3	Processed at pH 7	Processed at pH 11
0%	1.74 ± .01	1.69 ± .00	1.83 ± .01
10%	--	--	1.73 ± .01
20%	--	--	1.68 ± .02

Table 9 Effect of ball-milling on green densities of specimens CIPed at 250MPa with 8 wt.% Y_2O_3 / 2 wt.% Al_2O_3 added as sintering aids.

Whisker Loading	Processed and milled at pH 3	Processed and milled at pH 7	Processed and milled at pH 11
0%	Unmeasurable	1.76 ± .01	1.83 ± .01
10%	1.73 ± .01	1.72 ± .02	1.77 ± .015
20%	--	--	1.72 ± .01

green densities for all processing pH and whisker loadings. Ball-milling in combination with ultrasonication removes hard agglomerates from suspension and improves suspension homogeneity. Suspensions ball-milled at pH 3 produced green specimens that were too warped to measure the volume by calipers. Freeze-dried powders produced from ball-milled suspensions at pH 11 produced the highest green densities. Green densities of ball-milled pH 11 powders with 20 $^{v}/_{o}$ SiC_w were comparable to those of monolithic specimens without ball-milling. In addition to increasing the green densities, ball-milling of pH 7 and pH 11 suspensions produced a dark-gray hydrophobic residue on the surface of the suspensions. This residue was difficult to remove and was therefore still present in powders freeze-dried at these pHs. This residue was collected and characterized along with as-received and freeze-dried powders by X-ray diffraction.

X-Ray Analysis of Green Powders

X-ray analysis began with as-received powders. These results were then used to characterize the green specimens. Figures 20 - 23 show diffraction peaks for as-received α-Si_3N_4, β-SiC_w, Y_2O_3, and α-Al_2O_3 powders respectively. All data match the expected

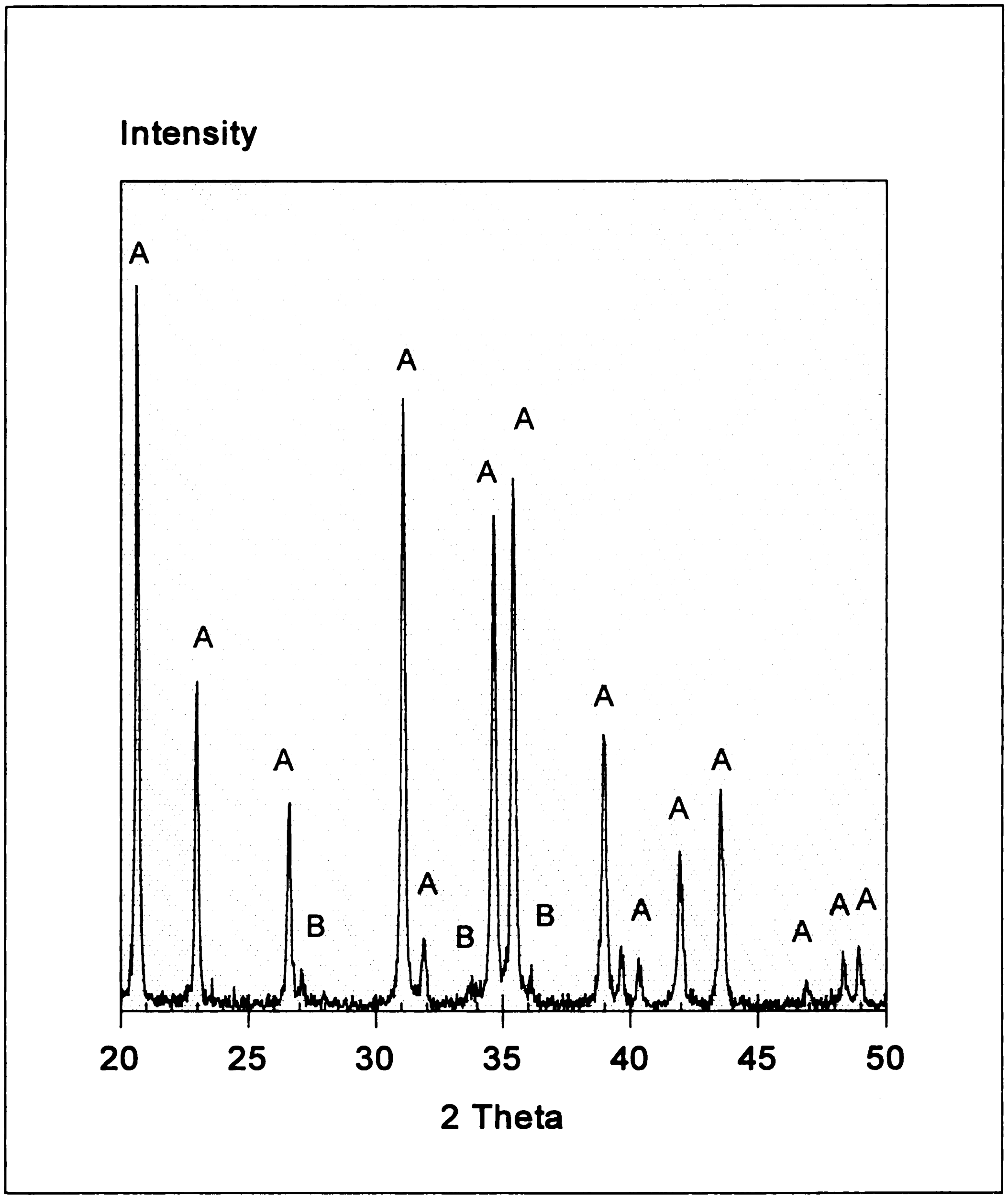

Figure 20 X-ray diffraction results for Ube Sn-e-10 as-received Si_3N_4. A = α- Si_3N_4 and B = β-Si_3N_4.

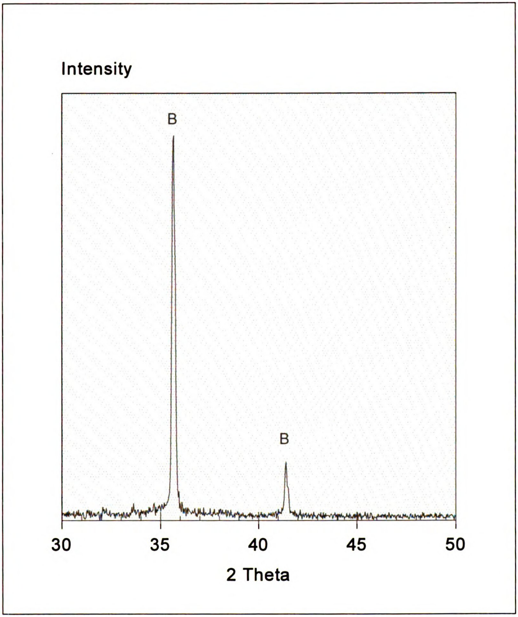

Figure 21 X-ray diffraction results for Tokai Whisker TWS-100 as-received β-SiC whiskers.

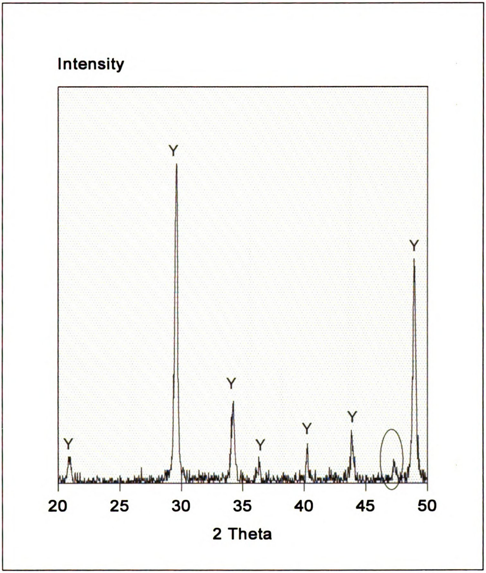

Figure 22 X-ray diffraction results for as-received Y_2O_3 powder. Circled region indicates undefined peak.

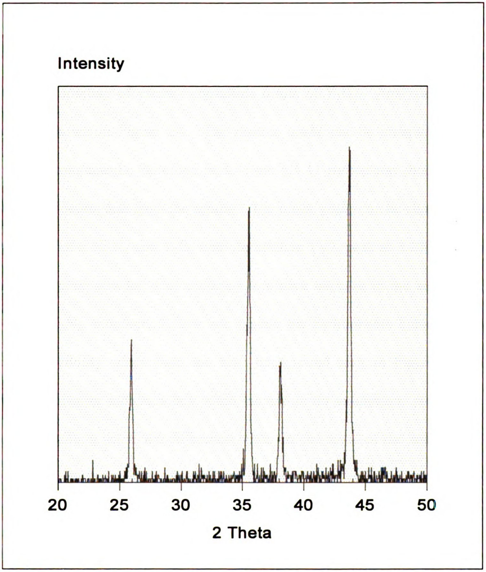

Figure 23 X-ray diffraction results for as-received α-Al_2O_3 powder.

spectrum (from JCPDS--the Joint Committee on Powder Diffraction Standards) with the exception of Y_2O_3 which showed an additional peak at ≈ 47.5° 2θ along with the shifting of smaller peaks from their standard positions. This may indicate the as-received Y_2O_3 powder is a mixture of various crystalline forms of Y_2O_3. Analysis of the ball-milling residue is shown in Figure 24. The residue could not be completely separated from suspension components, therefore, peaks from pH 11 suspension should be present along with the diffraction data from the residue. The major peaks can be characterized indicating the presence of α-Si_3N_4 and Y_2O_3 with the relative Y_2O_3 peak at 3.060 being much higher than in the green powder. This indicates a relative increase in the amount of Y_2O_3 with respect to Si_3N_4, however, it does not explain the hydrophobic behavior of the residue. Another possibility arises from the high background seen in Figure 24. Background correction software indicates this could be due to an amorphous phase that is forming during ball-milling where the diffraction peaks are the result of the inability to separate the suspension from the residue. Regardless, this skin forms on all suspensions ball-milled at neutral or basic pHs and is a part of all freeze-dried powders prepared by ball-milling in this pH range.

X-ray analysis was carried out on green specimens to evaluate the chemical state of the composite prior to sintering. Ball-milled green powders were chosen because if there are any chemical changes in the suspension components, they should be more noticeable in the ball-milled powders due to longer processing times and increased particle surface areas and interactions. Suspensions containing 10 $^{v}/_{o}$ SiC_w were also examined to see if the whiskers played a role in green chemistry. X-ray diffraction results for composite green

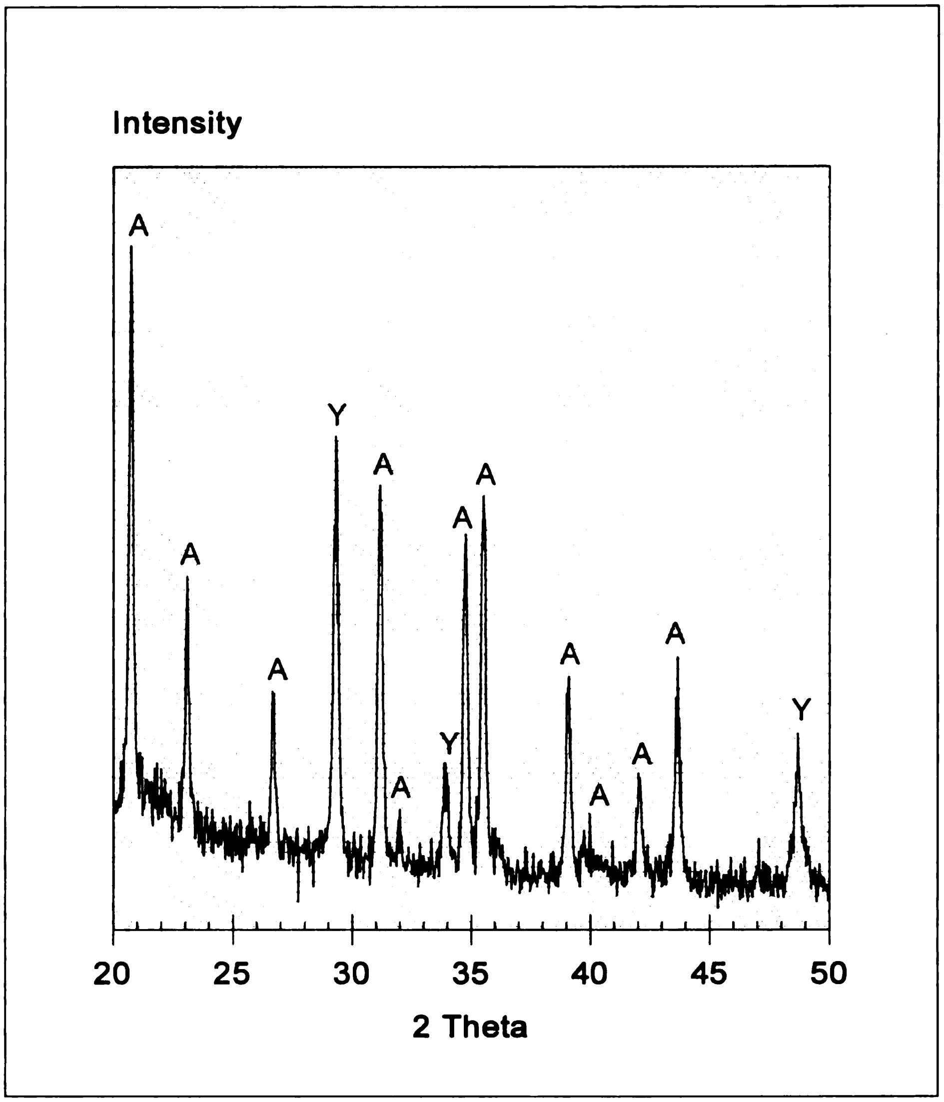

Figure 24 X-ray diffraction results for ball-milling residue from powders ball-milled at pH 7.5 and 11. A = α-Si_3N_4, Y = Y_2O_3. High background may indicate the presence of an amorphous Y-containing phase.

powders are shown in Figures 25 - 30. Results for pH 7 and 11 are nearly identical (Figures 25 - 26). Both show the presence of α-Si_3N_4, Y_2O_3, and β-SiC_w with no other crystalline phases present. Results for 10 $^v/_o$ β-SiC_w are also identical for pH 7 and 11 (Figures 27 - 28). Both show increased relative Y_2O_3 peaks over their monolithic counterparts. This is probably due to the relative increase in Y_2O_3 content to Si_3N_4 content with the addition of SiC_w. Composite suspensions prepared at pH 3 resulted in similar results, but with much smaller Y_2O_3 peaks (Figure 29 - 30). This is due to the fact that Y_2O_3 is soluble in nitric acid solutions [105]. Diffraction results of monolithic Si_3N_4 ball-milled at pH 3 showed no evidence of Y_2O_3. It is believed all the Y_2O_3 was dissolved in suspension during ball-milling and reprecipitated during freeze-drying into another crystalline compound. This is evidenced in Figure 22. These unknown peaks could not be characterized as an Yttria containing nitrate, nitrite, nitride, hydroxide, or ammonia containing compound. Therefore, it is unclear what chemical state the Y_2O_3 is in before sintering of pH 3 processed freeze-dried powders.

Sintered Density

Small amounts of some chemical species was evolved during sintering and deposited on crucible and furnace graphite walls. These were not evaluated as mass losses were low and decomposition did not appear to be prevalent. Sintered densities were first evaluated as a function of whisker loading for specimens processed at pH 11. All sintered results are from specimens containing 8% Y_2O_3 / 2% Al_2O_3 by weight. Results are shown in Figure 31 for ball-milied Si_3N_4 reinforced with both as-received and ball-milled SiC_w and sintered for 4 hours at 1800°C. Ball-milled SiC_w provide enhanced

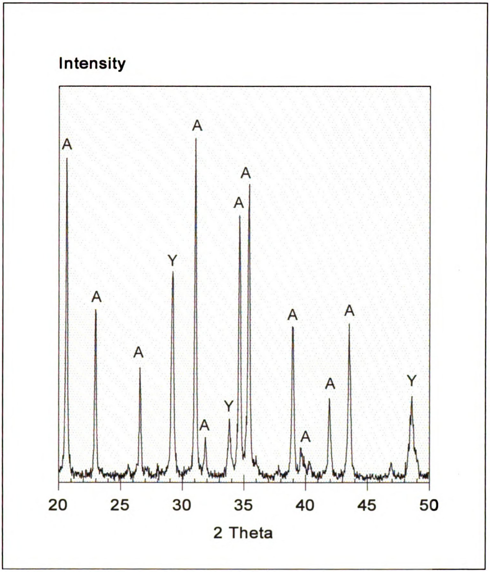

Figure 25 X-ray diffraction results for monolithic Si_3N_4 ball-milled at pH 7. A = α-Si_3N_4, Y = Y_2O_3.

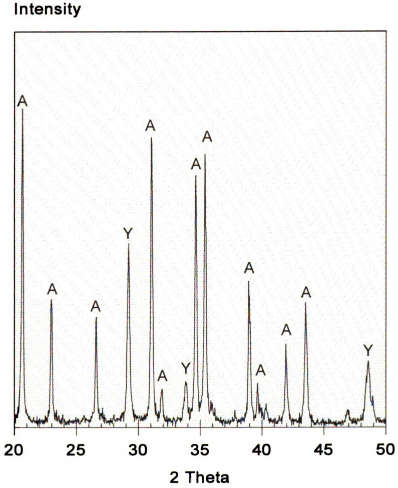

Figure 26 X-ray diffraction results for monolithic Si_3N_4 ball-milled at pH 11. A = α-Si_3N_4, Y = Y_2O_3.

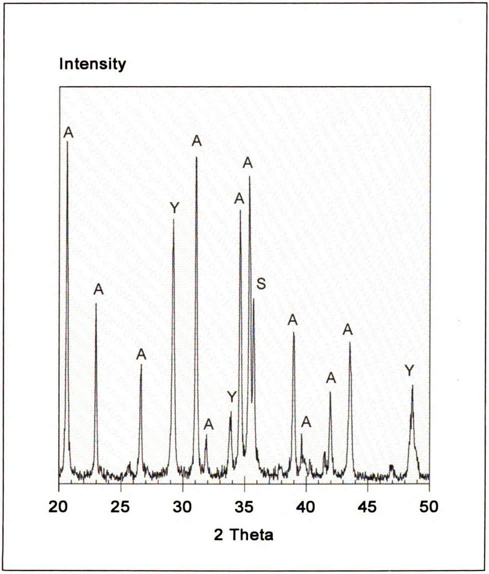

Figure 27 X-ray diffraction results for 10 $^{v}/_{o}$ SiC_w-Si_3N_4 ball-milled at pH 7. A = α-Si_3N_4, Y = Y_2O_3, S = SiC_w.

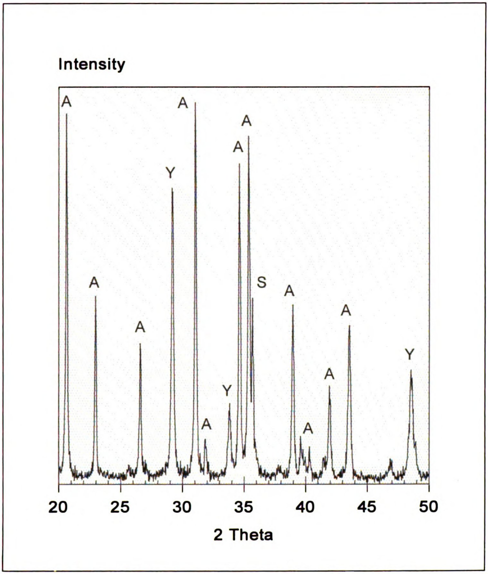

Figure 28 X-ray diffraction results for 10 $^v/o$ SiC_w-Si_3N_4 ball-milled at pH 11. A = α-Si_3N_4, Y = Y_2O_3, S = SiC_w.

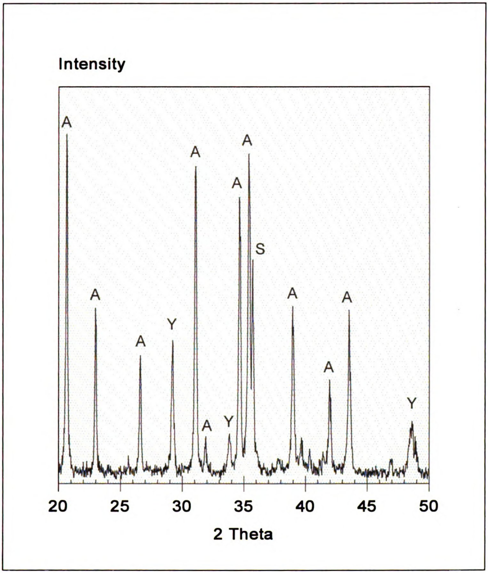

Figure 29 X-ray diffraction results for 10 ^{v}/o SiC_w-Si_3N_4 ball-milled at pH 3. A = α-Si_3N_4, Y = Y_2O_3, S = SiC_w.

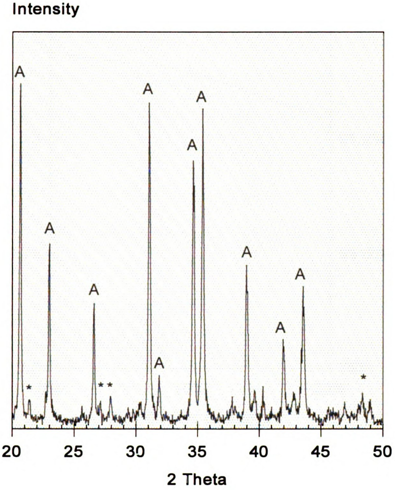

Figure 30 X-ray diffraction results for monolithic Si_3N_4 ball-milled at pH 3. A = α-Si_3N_4, Y = Y_2O_3. Note the Y_2O_3 peaks are missing. The new uncharacterized crystalline phase is indicated by *.

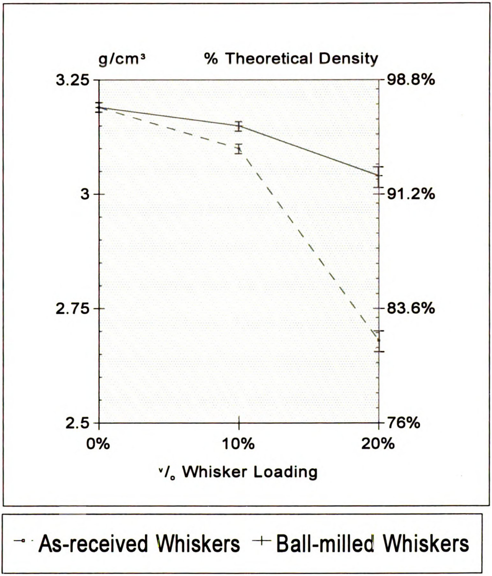

Figure 31 Density as a function of whisker loading for ball-milled Si_3N_4 specimens sintered 4 hours. Results show higher densities for composites with ball-milled (reduced aspect ratio) SiC_w in addition to milling of Si_3N_4.

densification of the composite by improving homogeneity and reducing the aspect ratio of the SiC_w. SiC_w can act to reduce rearrangement during liquid phase sintering and decrease the final sintered density and/or increase the time to full density. This is shown more clearly in Figure 32 for powders containing 10 $^v/_o$ SiC_w. The highest densities are achieved when either all components are milled, or only when SiC_w are milled. However, when all components are milled, the densification rate increases. When only the Si_3N_4 matrix is milled, rearrangement is hampered and intermediate phase sintering must occur over a longer time to achieve full density. This is shown in Figure 32. The slope of a plot of density versus sintering time for powders with only matrix milling show the highest sintering rate from 1-2 hours. This is due to the fact that more liquid is necessary to allow for initial rearrangement to occur. Sintering then continues at nearly the same rate as materials with reduced aspect ratio whiskers. Therefore, it is expected that powders with milled Si_3N_4 and as-received whiskers could achieve the same densities as the other milled powders with increased sintering time. Powders that received no ball-milling showed minimal densification after 4 hours.

Monolithic powders achieve higher densities more quickly than those reinforced with ball-milled whiskers, as shown in Figure 33. As whisker loading increases, even with reduced aspect ratio whiskers, final density after 4 hours sintering decreases. However, because the 20 $^v/_o$ composite still shows an appreciable sintering rate after 4 hours, the final density difference between 10 $^v/_o$ and 20 $^v/_o$ should lessen with increased sintering time.

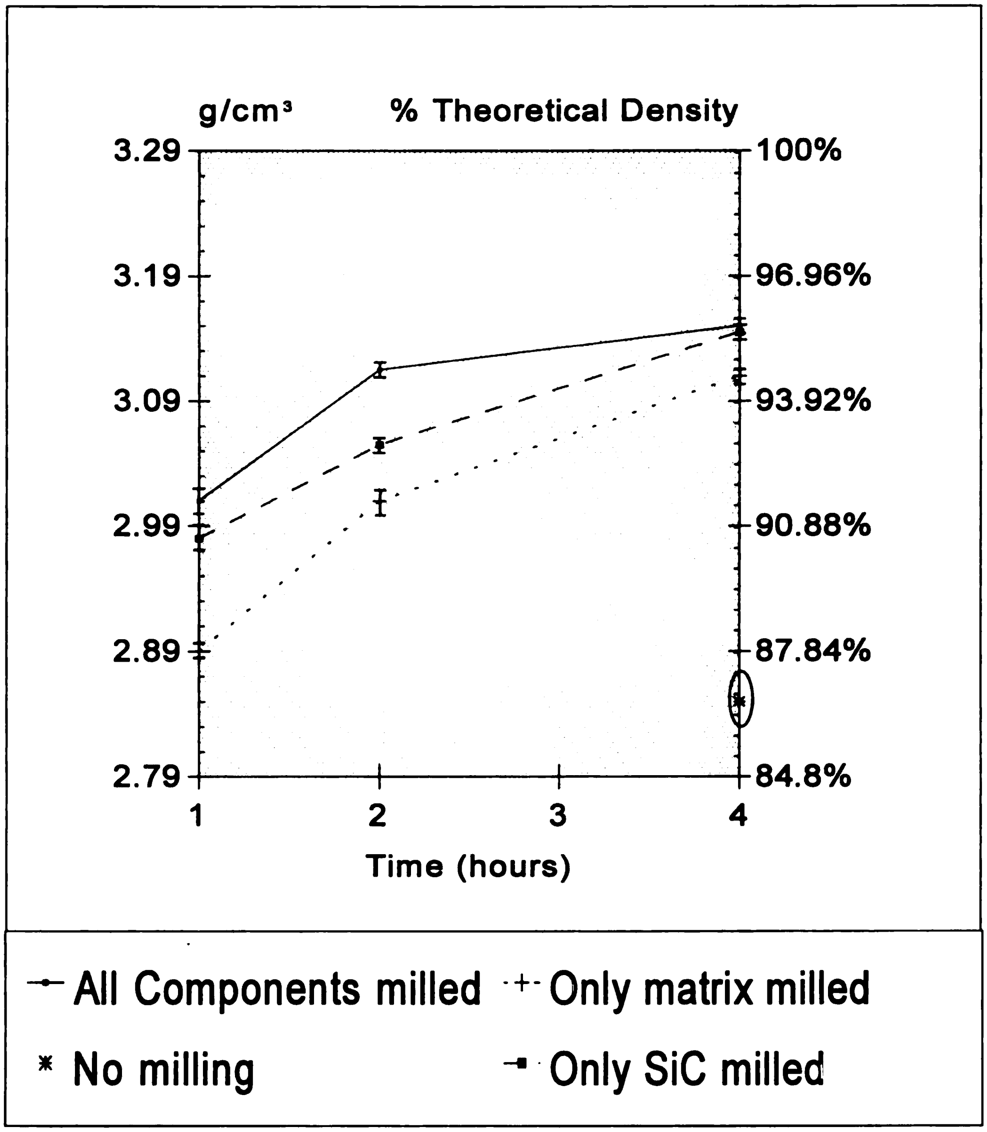

Figure 32 Density as a function of time for selected component ball-milled powders. High density is achieved more quickly when all components are milled. Milling SiC_w is more important for high density than milling Si_3N_4 alone. After 4 hours, compacts containing unmilled components showed only limited densification. This point is circled for clarity.

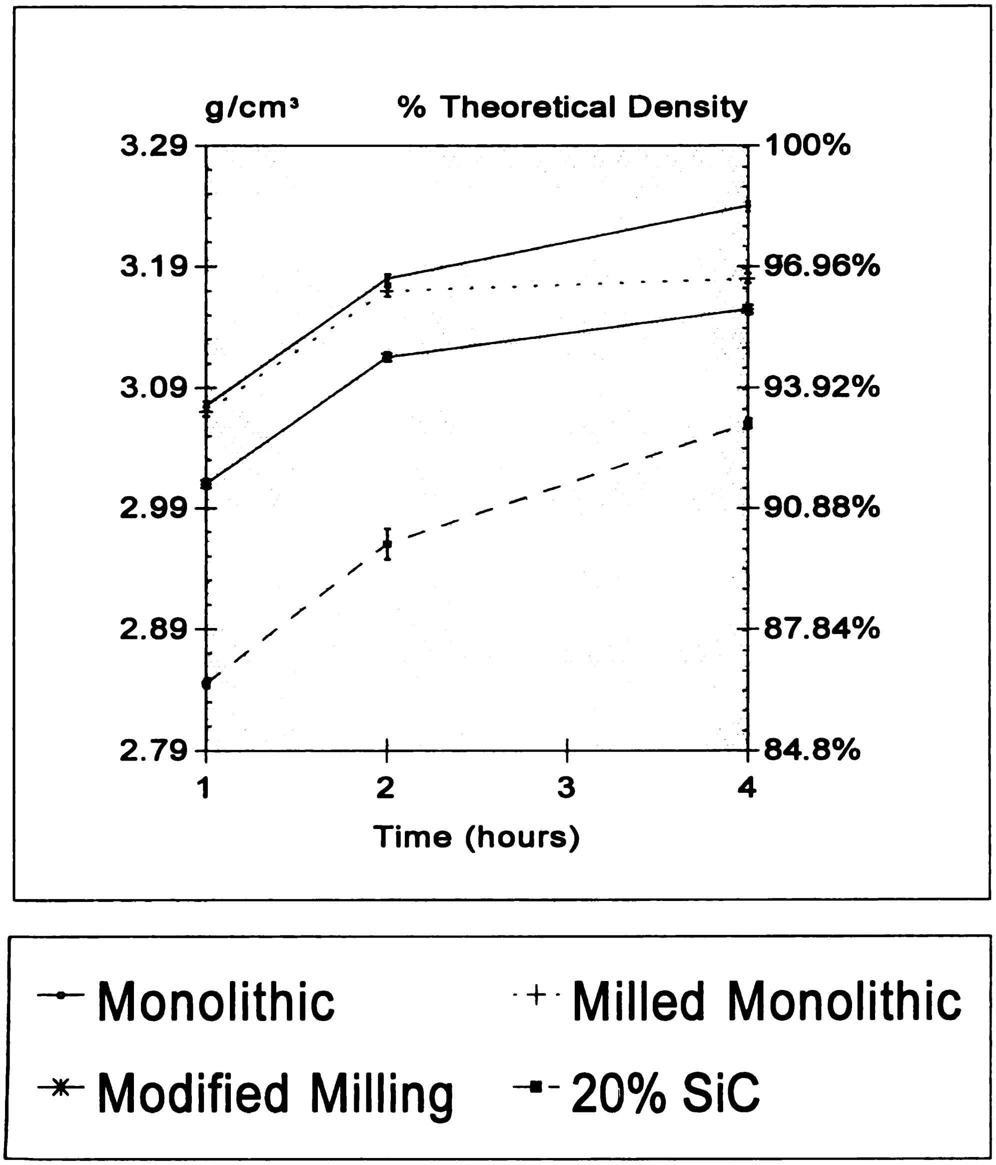

Figure 33 Density as a function of time and whisker loading for powders where all components were ball-milled. Final density decreases as whisker loading increases. Compared to unmilled monolithic powder, ball-milled monolithic powder shows a lower final density and lower densification rate.

Final density as a function of processing pH is shown in Figure 34 for monolithic compacts with and without ball-milling, and 10 $^{v}/_{o}$ SiC_w compacts sintered for 4 hours at 1800°C. Examining unmilled monolithic powders reveals the highest sintered densities at pH 3. This follows logically from green density results, where pH 3 yielded the highest green densities for monolithic unmilled powders. Examining ball-milled monolithic powders, an entirely different trend is revealed. Powders processed at pH 7 give the highest sintered density, while the final density of powders processed at pH 3 and 11 go down with respect to their unmilled densities. This may be due to the effects of ball-milling on the green chemistry at these pH. At pH 3 there is a complete solutionizing of Y_2O_3, and reprecipitation into another crystalline form, while at pH 11 there is a substantial amount of skin formed on the ball-milled suspensions which is incorporated into the powder during freeze-drying. These changes in the chemical state of the sintering aids seems to have a major effect on the sintered density of ball-milled monolithic specimens. These chemical changes, however, do not have the same effect on sintered density for the composite specimens.

Composites of 10 $^{v}/_{o}$ SiC_w show the highest sintered densities with powders processed and ball-milled at pH 3 and 11. This is due to the high degree of agglomeration of SiC_w and Si_3N_4 that occur at pH 7. Whisker agglomerates have been shown to substantially decrease sinterability of composite green compacts [58]. Although processing the composites at pH 3 and 11 should substantially reduce whisker agglomeration, the highest densities of 10 $^{v}/_{o}$ SiC_w were still considerably lower than the lowest densities for monolithic specimens with identical sintering additives and

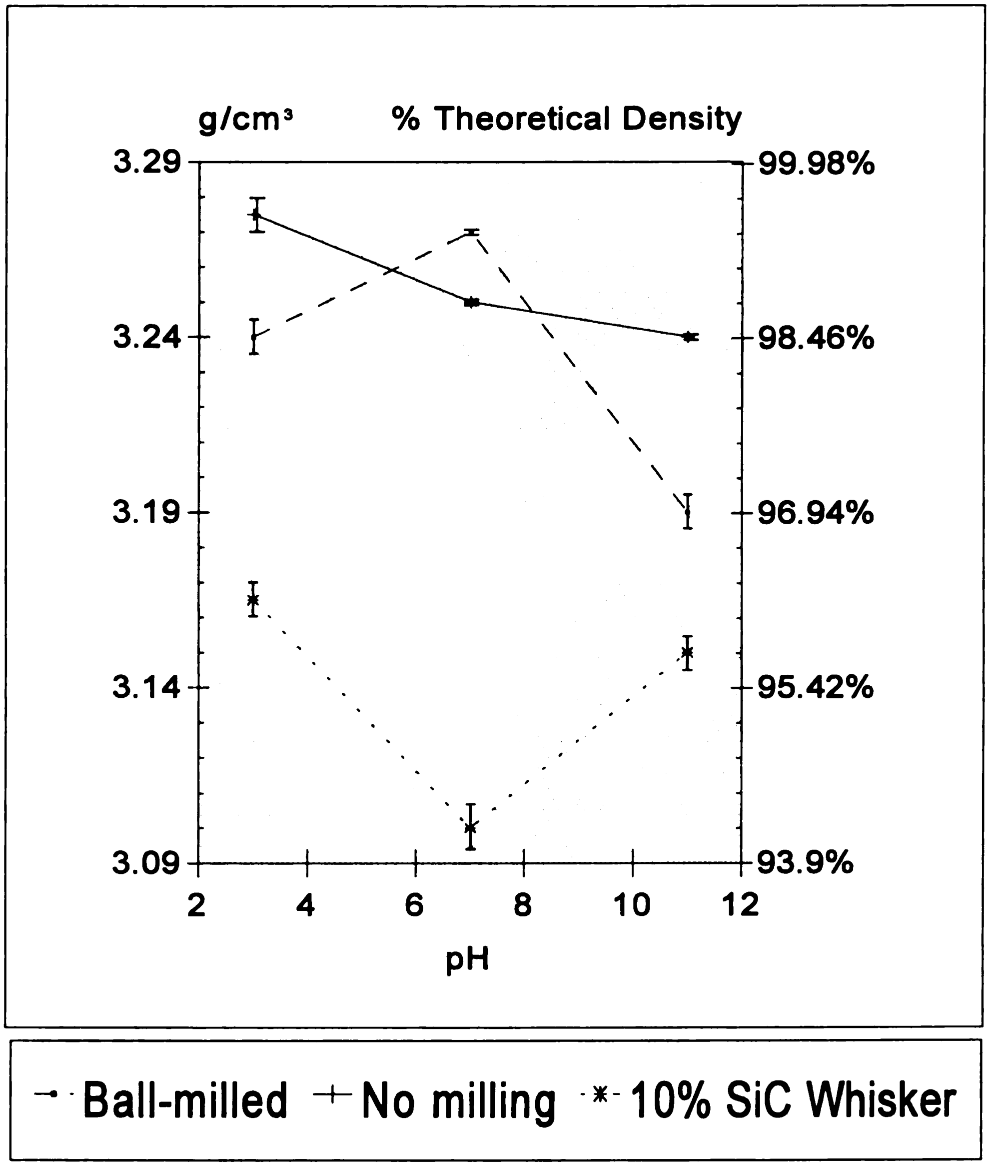

Figure 34 Density as a function of pH for ball-milled and unmilled monolithic and ball-milled 10 $^v/_o$ SiC_w-Si_3N_4.

processing conditions. This is due to the fact that whiskers impede rearrangement during the initial stages of liquid phase sintering and, in addition, increase diffusion distances during intermediate stages of liquid phase sintering. This slows the $\alpha \rightarrow \beta$ transformation and the driving force for liquid phase sintering of Si_3N_4. SiC_w have also been shown to have a rough surface finish due to a high number of stacking faults in β-SiC_w. This roughness increases surface area of the SiC_w and thereby increases the thickness of glassy phase surrounding the whisker after sintering [108]. Therefore, more liquid phase is required to densify the composite as compared to the monolithic compact and because sintering aid additions were equal for all specimens, whisker reinforced compacts could not achieve the same densities as the monolithic compacts, unless there was a surplus of liquid phase for the monolithic specimens during sintering. Another possible reason for the lower densities could be the chemical state of the Y_2O_3 at pH 3 and 11. If the effects described above have a negative effect on sintering in monolithic specimens, they may also have a negative effect on the sinterability of the composite. Examining the crystalline phases present in the sintered compacts may help to answer this question.

X-Ray Analysis of Sintered Components

X-ray diffraction patterns for selected specimens processed at pH 11 are shown in Figures 35 - 41 . Results indicate Si_3N_4 is present only in the β form for all specimens after sintering for as little as 1 hour (Figure 41). Diffraction peaks were evaluated using d-spacings from a crystallography catalog and compared with a study by Chen et al. [109] who studied x-ray diffraction (XRD) data for Y_2O_3/Al_2O_3 assisted Si_3N_4/SiC_w sintered composites. Patterns were also compared to XRD data from the initial starting powder

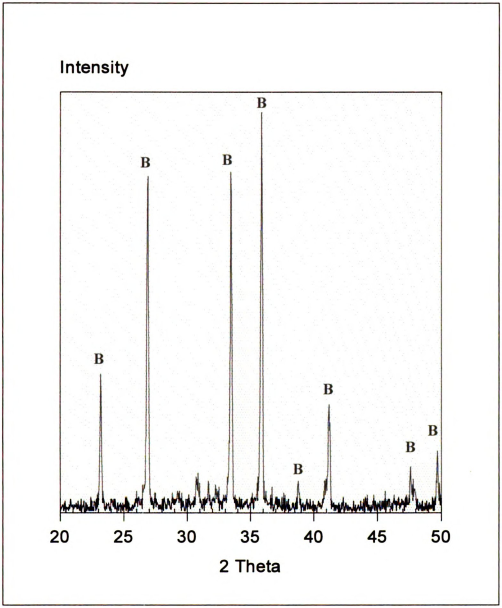

Figure 35 X-ray diffraction results for ball-milled monolithic Si_3N_4. Sintered 4 hours. B = β-Si_3N_4.

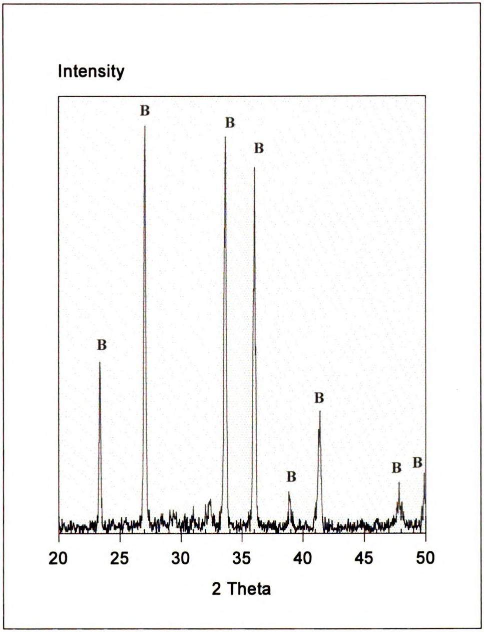

Figure 36 X-ray diffraction results for unmilled monolithic Si_3N_4. Sintered 4 hours. B = β-Si_3N_4.

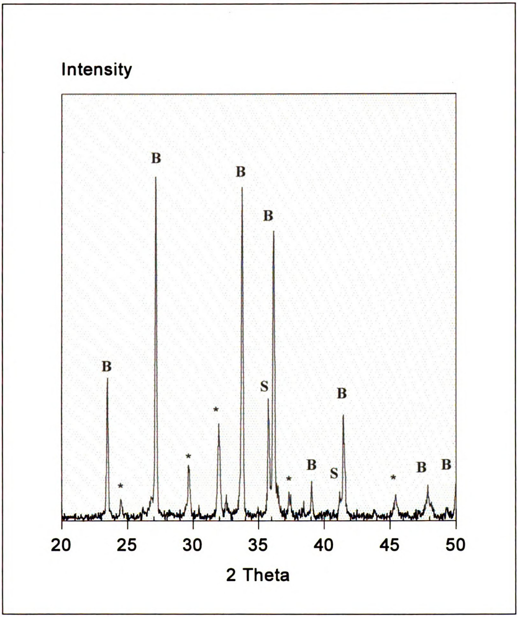

Figure 37 X-ray diffraction results for ball-milled Si_3N_4 with 10 $^v/o$ SiC_w. Sintered 4 hours. B = β-Si_3N_4, S = β- SiC_w * = $Y_2O_3 \bullet Si_3N_4$.

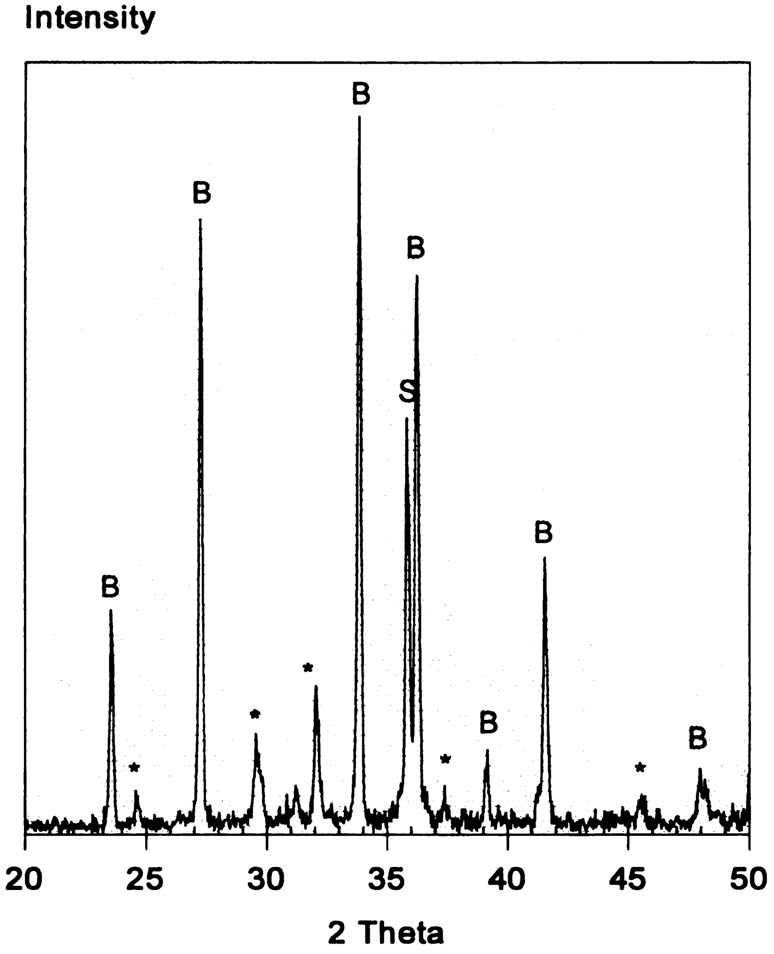

Figure 38 X-ray diffraction results for ball-milled Si_3N_4 with 20 ^{v}/o SiC_w. Sintered 4 hours. B = β-Si_3N_4, S = β- SiC_w * = Y_2O_3•Si_3N_4.

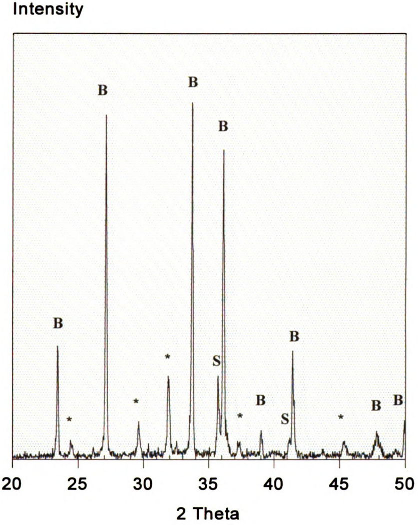

Figure 39 X-ray diffraction results for ball-milled Si_3N_4 with 10 $^v/o$ SiC_w added after milling. Sintered 4 hours. B = β-Si_3N_4, S = β- SiC_w, * = $Y_2O_3 \bullet Si_3N_4$.

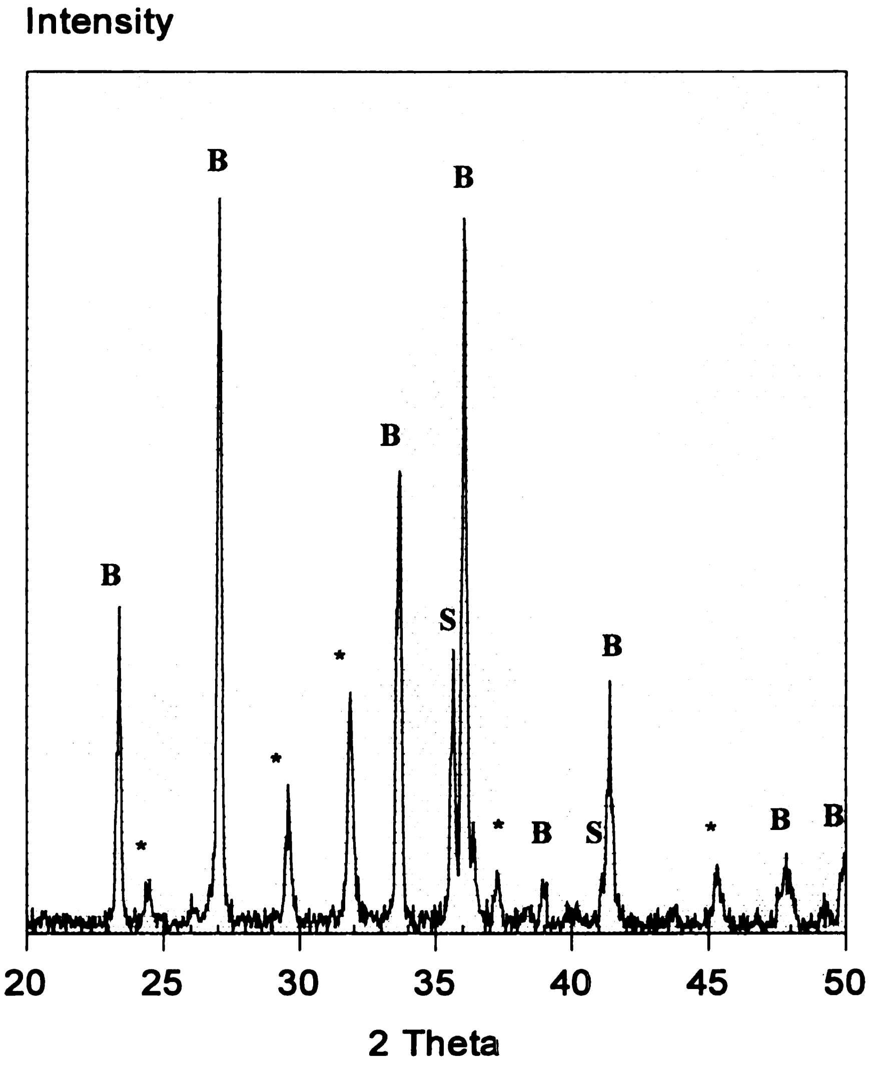

Figure 40 X-ray diffraction results for ball-milled Si_3N_4 with 20 $^v/o$ SiC_w added after milling. Sintered 4 hours. B = β-Si_3N_4, S = β- SiC_w, * = $Y_2O_3 \bullet Si_3N_4$.

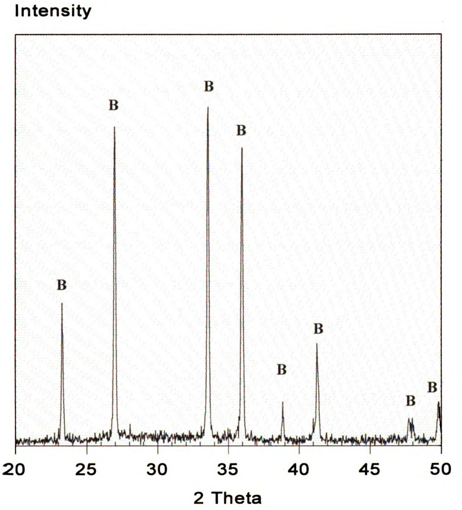

Figure 41 X-ray diffraction results for monolithic Si_3N_4 ball-milled at pH 11. Sintered 1 hour. B=β-Si_3N_4.

which was predominately α. β-SiC was retained within whisker reinforced sintered specimens, but the degree of degradation of β-SiC was not evaluated. However, literature indicates SiC whiskers are inert at the sintering temperatures employed in this study, therefore, we would expect degradation to be minimal as demonstrated by Chen et al. [109]. Whitehead et al. [73] demonstrated β-SiC whiskers resist recrystallization up to 2050°C and effects on the morphology at 1850°C in Ar and N_2 atmospheres were insignificant (Figure 42) showing only the formation of a sinter-boundary after 2 hours. β-SiC_w polytype is stable even with large morphology changes, such as whisker spherodization at high temperatures. However, temperatures above 2050 °C would be required for this to occur. β-SiC_w will degrade in oxidizing atmospheres, or may become more unstable in the presence of an oxynitride silicate glass [49]. Possible reactions include;

$$2SiC + SiO_2 + N_2 \Leftrightarrow Si_3N_4 + 2CO\uparrow$$

or

$$3SiC + 3SiO_2 + 2N_2 \Leftrightarrow Si_3N_4 + 3SiO + 3CO\uparrow$$

with the later reaction occurring over the former when whisker surface contact with the liquid is high. However, if equilibrium lies to the right of the equation, the Si_3N_4 matrix could become unstable. Zheng et al. [49] studied the suppression of these reactions by the use of various powder beds during sintering. It was determined that a powder bed of 50% BN and 50% Si_3N_4 minimized weight losses. Whitehead et al. [73] indicates recrystallization of SiC_w at 1600°C in the presence of liquid Silicon. Therefore, the glass composition of sintered composites could effect whisker stability. Boron carbide, a known sintering aid for SiC, could also effect whisker stability in the sintered compact. However,

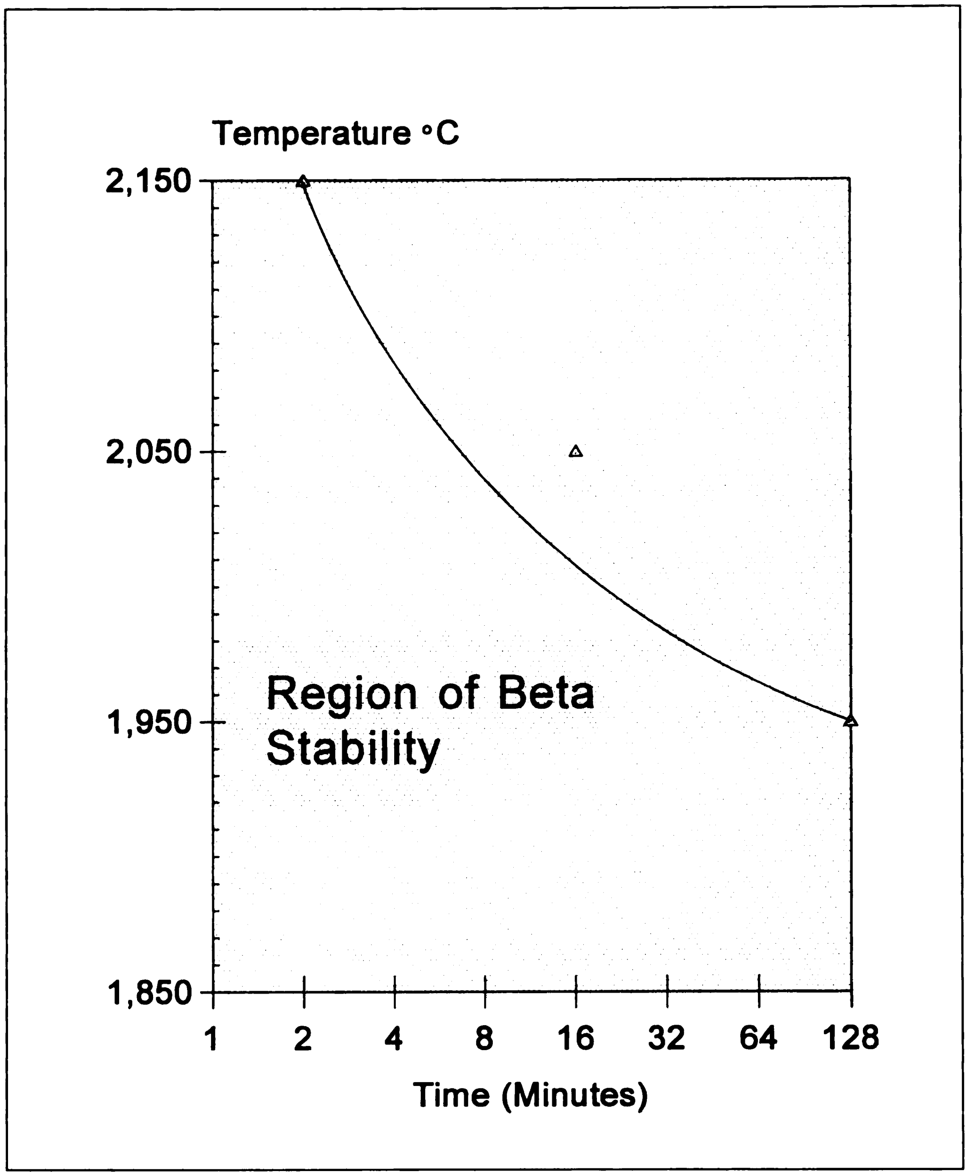

Figure 42 Plot showing stability of SiC_w with respect to time and temperature. Adapted from Whitehead et al.[73].

x-ray results indicate polytype stability and show no evidence of BC. Morphological changes would be evidenced by spherodization of SiC_w which would be obvious during SEM analysis of fracture surfaces. No evidence was found to suggest such degradation. Therefore, it is believed that the effect of the liquid phase on the SiC_w during sintering is minor. Whitehead also notes that color change of whiskers can indicate degradation. It is believed that SiC_w get their green color from N_2 impurities. Loss of N_2 during sintering is indicated by a color change from green to gray. All sintered composite specimens maintained a bright green color, indicative of nitrogen retention and whisker stability [73].

Grain boundary phases remained glassy in monolithic Si_3N_4 as evidenced by diffraction patterns shown in Figures 35 - 36. However, the presence of a third crystalline phase in the whisker reinforced specimens is clear from XRD data (Figures 37 - 40). These five additional diffraction peaks coincide with $Y_2O_3 \bullet Si_3N_4$ as characterized by JCPDS standard powder diffraction file. $Y_2O_3 \bullet Si_3N_4$ is shown in the Y_2O_3 -Si_3N_4-SiO_2 phase diagram [110] in Figure 43. Shih et al. [111] reports a very similar diffraction pattern for Si_3N_4-SiC_w composites with Y_2O_3-Al_2O_3 additives reporting a $YSiO_2N$ or K-phase as the additive crystalline phase. While there are many crystalline Y_2O_3 -Si_3N_4-SiO_2 compounds with similar diffraction patterns, measurement of relative intensities from the composite x-ray peaks indicates the $Y_2O_3 \bullet Si_3N_4$ compound. Because $Y_2O_3 \bullet Si_3N_4$ is a relatively low O_2 compound (Figure 44), this coincides with the fact that the starting Si_3N_4 is low in O_2.

X-ray results for specimens processed at pH 3 and 7 are shown in Figures 45 - 50. Composite specimens processed at these pHs also show evidence of a third crystalline phase, however, it is of different composition than that characterized in pH 11 specimens

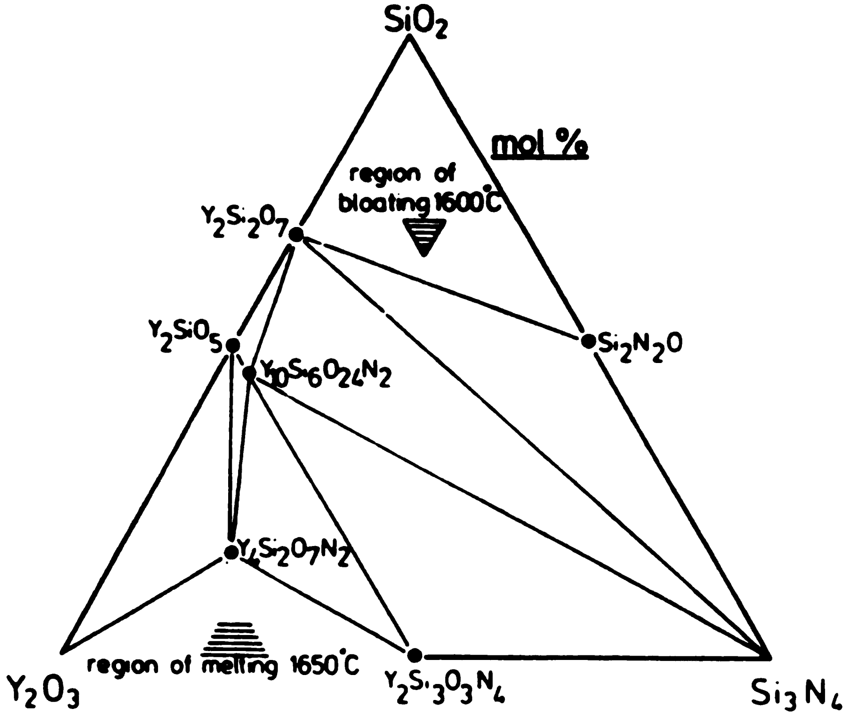

Figure 43 Y_2O_3-SiO_2-Si_3N_4 phase diagram. Adapted from Jack et al. [110].

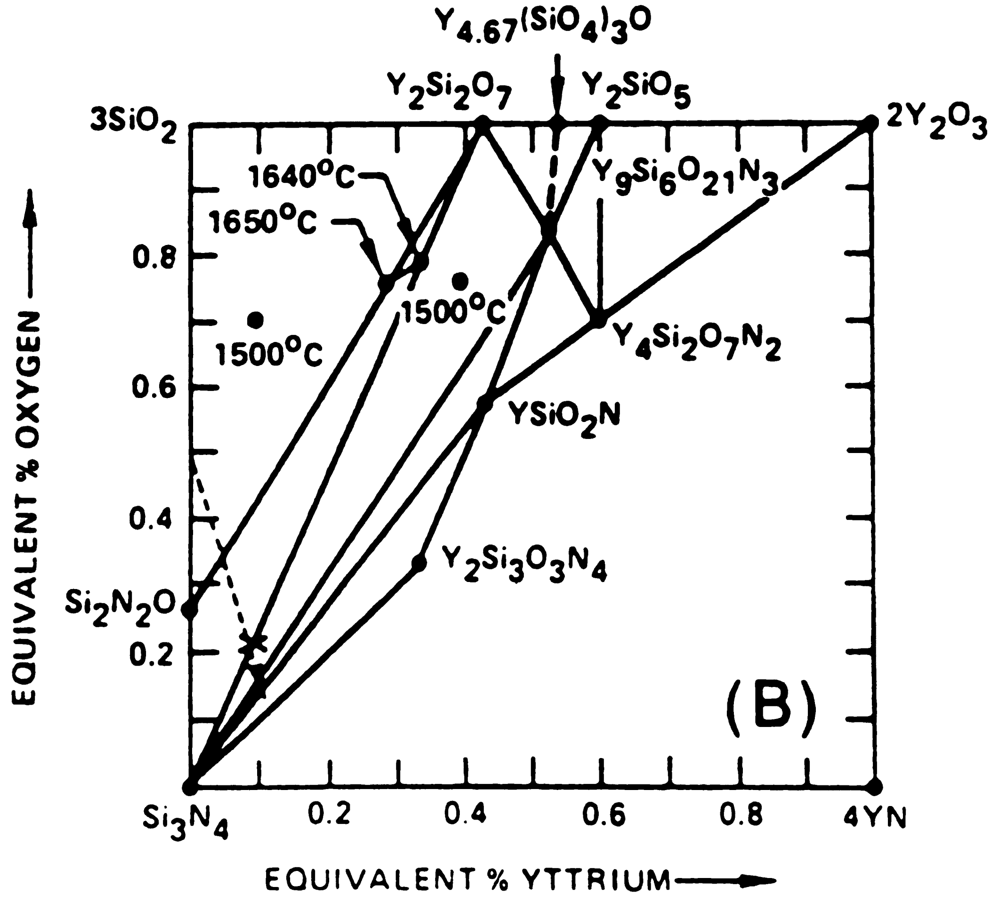

Figure 44 O_2 equivalents phase diagram. Adapted from [55].

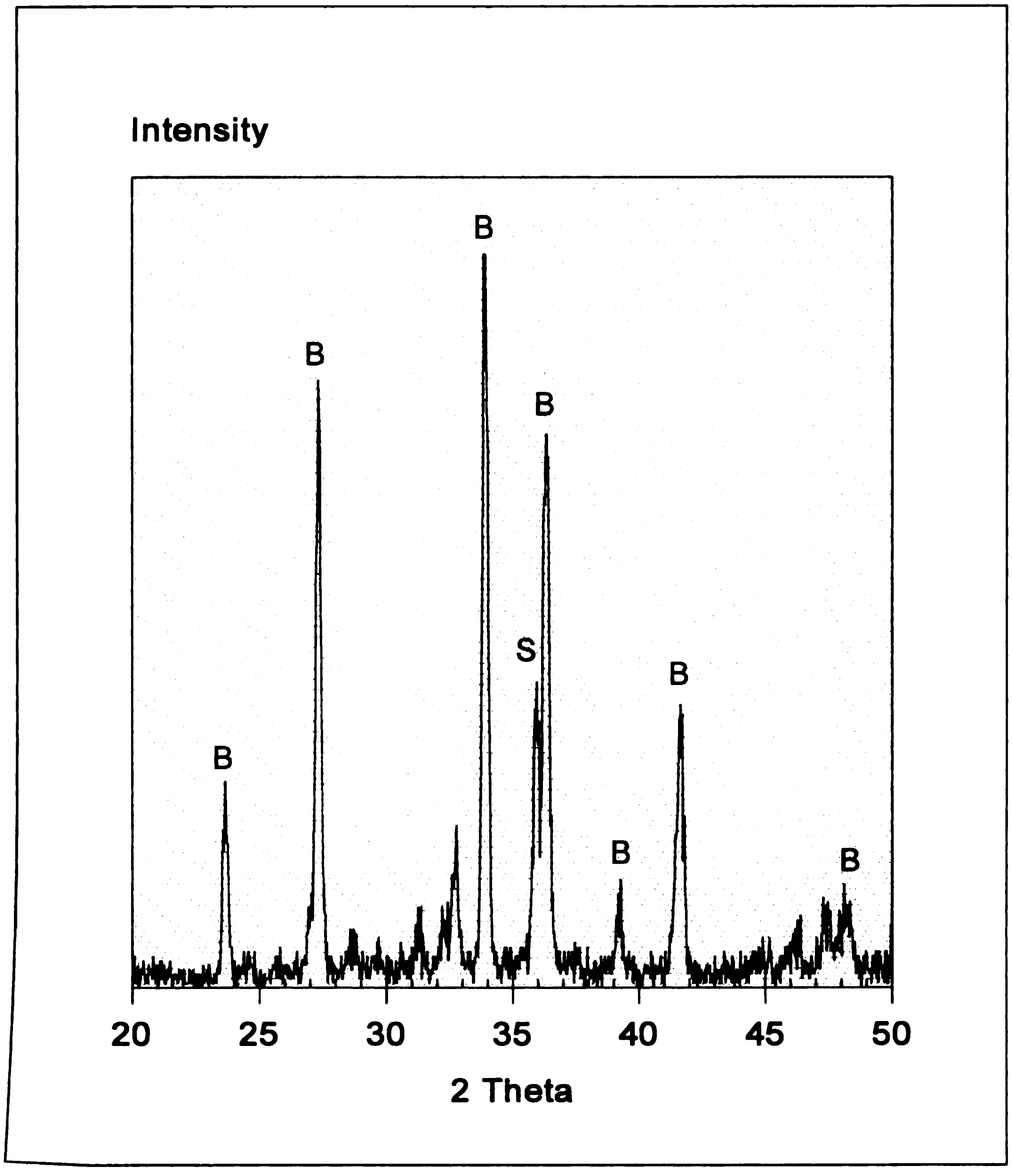

Figure 45 X-ray diffraction results for ball-milled Si_3N_4 processed at pH 3 with 10 $^v/o$ SiC_w. Sintered 4 hours. B = β-Si_3N_4 S = β- SiC_w.

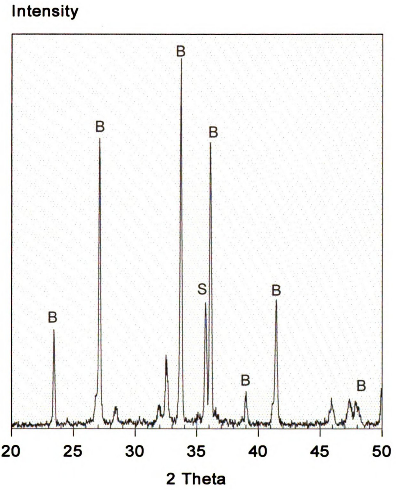

Figure 46 X-ray diffraction results for ball-milled Si_3N_4 processed at pH 7 with 10 $^v/_o$ SiC_w. Sintered 4 hours. B = β-Si_3N_4, S = β-SiC_w.

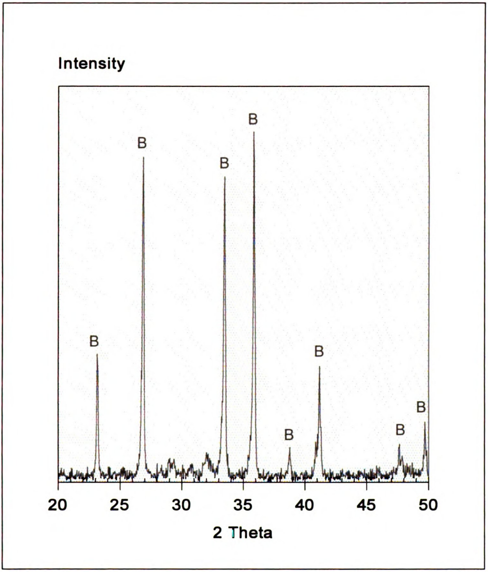

Figure 47 X-ray diffraction results for unmilled monolithic Si_3N_4 processed at pH 3. Sintered 4 hours. B = β-Si_3N_4.

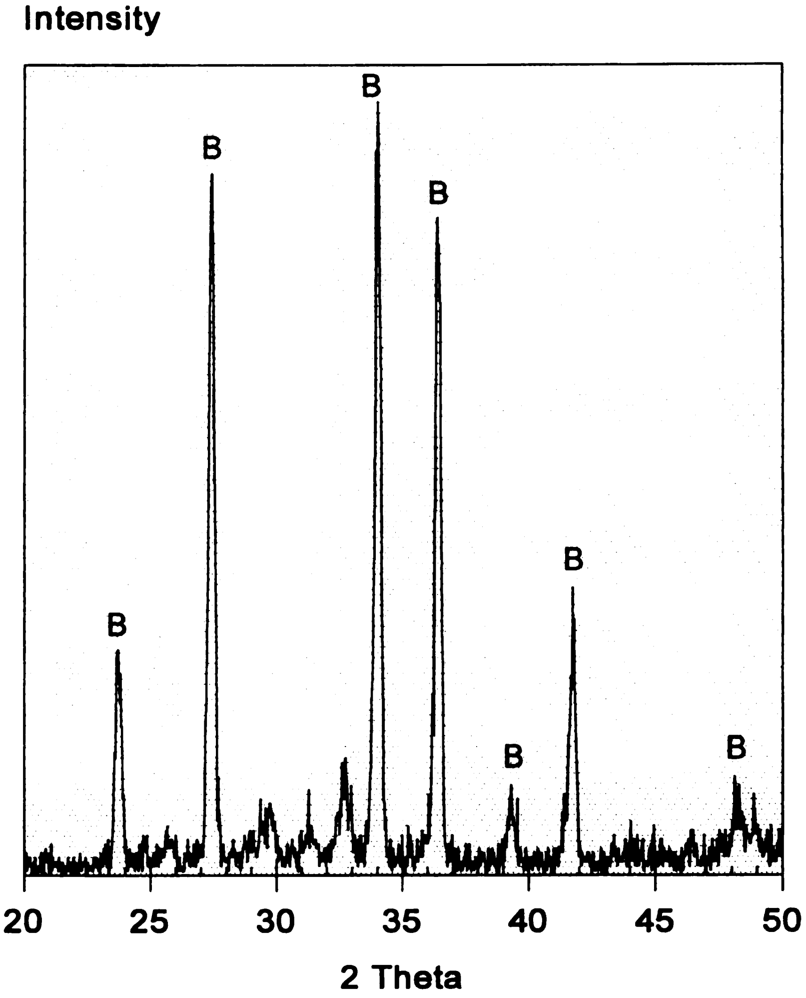

Figure 48 X-ray diffraction results for unmilled Si_3N_4 processed at pH 7. Sintered 4 hours. B = β-Si_3N_4.

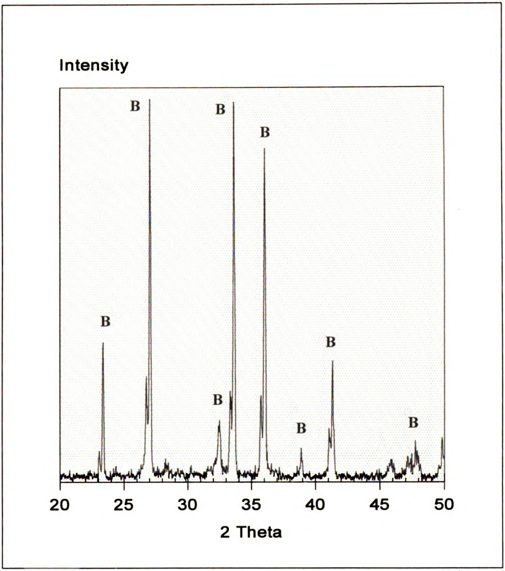

Figure 49 X-ray diffraction results for monolithic Si_3N_4 ball-milled at pH 3. Sintered 4 hours. B = β-Si_3N_4.

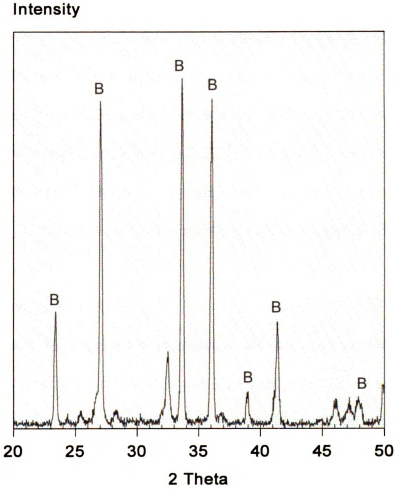

Figure 50 X-ray diffraction results for monolithic Si_3N_4 ball-milled at pH 7. Sintered 4 hours. B = β-Si_3N_4.

and remains uncharacterized (Figures 45 - 46). Like the composite specimens, the unmilled sintered compacts at pH 3 and 7 also show very similar results, but with yet another different uncharacterized crystalline phase present (Figures 47 - 48). Ball-milling at these pHs reveals yet another set of unique x-ray results (Figures 49-50), with both pH 7 and pH 3 yielding different uncharacterized results. The diffraction peaks at pH 3 are especially unique in that the β-Si_3N_4 peaks have split into doublets. This seems to indicate the substitution of a larger atom into the β-Si_3N_4 lattice. Al is known to be soluble in β-Si_3N_4 and may be responsible for the peak splitting. However, these peaks correspond only to a shift in β-Si_3N_4 and not to SiAlON, therefore, a solid solution of Al_2O_3 in β-Si_3N_4 is more likely.

SiC_w Toughening of Si_3N_4

Because the toughening mechanisms discussed earlier behave in a material dependent manner, SiC_w dispersed in a Si_3N_4 matrix may toughen in a different manner than when its dispersed in other matrix materials. In fact some studies have shown no appreciable toughening in Si_3N_4 systems due to the addition of SiC_w [82]. Summarizing possible toughening mechanisms, little toughening would be expected due to crack bowing because of the low shear strength of SiC_w [87]. Only minimal toughening could occur by crack deflection, because deflection is already prevalent in monolithic Si_3N_4 due to TEA and high aspect ratio beta-grains [76,86]. Therefore, SiC_w could only strengthen in an additive manner, or by some additional deflection due to E differences (511 and 297 GPa respectively for SiC_w and Si_3N_4) [103].

The addition of SiC_w could toughen by microcracking, due to the difference in thermal expansion coefficients (3.3 - $4.5x10^{-6}$ K^{-1} for SiC and $3.0x10^{-6}$ K^{-1} for Si_3N_4) [82], but again because Si_3N_4 is non-cubic, microcracking can be present without the addition of a second phase due to TEA. Microcracking is also highly dependent on grain size, therefore, this toughening mechanism will only occur for a narrow range of grain size materials. In addition, microcracking mechanisms of toughening have shown only 10% increase in toughness over the monolithic material [88]. SEM video films of *in situ* stressing of a crack indicates microcracking around the crack tip of both monolithic and whisker composite material, however, microcracking seems more pronounced when whiskers are present [82]. The relative thermal expansion coefficients suggest whiskers are in tension and Si_3N_4 is in compression giving rise to a tensile stress at the interface which is favorable for crack propagation through the interface and improved pull-out [82].

Finally, whisker pullout and bridging mechanisms could act to toughen Si_3N_4. While pullout has not been mentioned prevalently in many studies, bridging has been shown to be prevalent for both SiC_w reinforced, and monolithic β-Si_3N_4. Again, SiC_w would be strengthening in an additive manner, but if SiC_w aspect ratios are higher than beta-grains, bridging distances would be increased and the number of traction sites would be increased by the presence of SiC_w. However, when fracture toughness is evaluated by indentation techniques, a single value fracture toughness is generated. Because bridging and pullout mechanisms act at large distances from the crack tip, their toughening may be more easily assessed from examining R-curve behavior as opposed to single values of fracture toughness [76]. Experimental results seem to follow the above theories for SiC_w

reinforcement of Si_3N_4. Olagnon et al. [82] reports crack bridging to lead to the highest degree of toughening among all observable active toughening mechanisms.

Evidence of active fracture toughening mechanisms could be observed by SEM from secondary cracking on fracture surfaces and from polished and indented surfaces used to determine fracture toughness. Figure 51a and b indicate crack bridging occurring in both monolithic and whisker reinforced β-Si_3N_4. Optical micrographs of indentations also reveal crack deflection in both monolithic and SiC_w reinforced β-Si_3N_4. Therefore, there is evidence of toughening due to high aspect ratio constituents in both the monolithic and composite specimens. Other investigators have also reported little improvement of properties by the addition of SiC_w .

Olagnon et al. [82] sintered specimens at 1850°C under 1 MPa N_2 for 6 hours using varying amounts of Y_2O_3 and Al_2O_3 as sintering aids with 20 $^v/_o$ SiC_w. They reported K_{IC} of $\approx$ 7 MPam$^{1/2}$ for 20 $^v/_o$ SiC_w, however, were able to produce K_{IC} = 7.6 MPam$^{1/2}$ for monolithic Si_3N_4. The monolithic material exhibited more signs of debonding and a greater average grain size and aspect ratio. Therefore, it was concluded whiskers suppressed grain growth and rough surfaces of the whiskers allow less debonding to occur. Therefore, while SiC_w encourage some strengthening mechanisms, they suppress others active in the monolithic Si_3N_4.

Result of K_{IC} Determination for Si_3N_4 and SiC_w-Si_3N_4

Fracture toughness results from indentation testing are shown in Figure 52 as a function of whisker loading and whisker aspect ratio for monolithic and composite specimens produced at pH 11. The bars under 0 vol.% whisker loading compare ball-milled

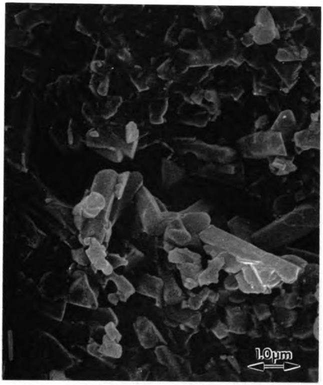

Figure 51a Micrograph taken from secondary crack found along the fracture surface. a) shows evidence of both crack deflection and crack bridging away from the crack tip in a monolithic Si_3N_4.

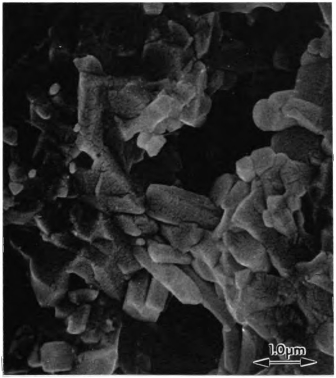

Figure 51b b) Micrograph shows a crack bridge in a secondary crack on a 10 $^{v}/o$ SiC_w specimen.

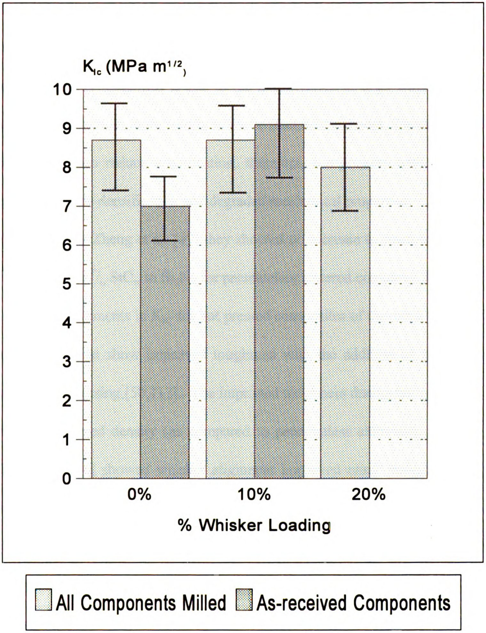

Figure 52 Fracture Toughness as a function of whisker loading and ball-milling for specimens processed at pH 11.

matrix to unmilled, with the ball-milled Si_3N_4 showing a higher fracture toughness. For 10% whisker loading, specimens containing as-received whiskers in a ball-milled Si_3N_4 show a slightly higher fracture toughness than specimens where all components were milled together. This higher toughness is due to the maintenance of high whisker aspect ratios which, as discussed earlier, more readily improve fracture toughness. However, high aspect ratio components also reduce densification, therefore, components with 20 $^v/_o$ unmilled whiskers showed little densification and degraded mechanical properties.

In a study by Zheng et al. [49] they showed no increase in fracture toughness with the addition of 10-30 $^v/_o$ SiC_w to Si_3N_4 for pressureless sintered compacts (K_{IC}=4 MPam$^{1/2}$), but did show improvements in K_{IC} for hot pressed composites of the same composition. In fact, most studies that show improved toughness with the addition of SiC_w consolidate specimens by hot pressing [50,112]. The improved toughness during hot pressing could be due either to improved density (as compared to pressureless sintering), or alignment of SiC_w. Liu et al. [66] showed whisker alignment improved crack deflection toughening. Aligned whisker planes can be modeled in 2d rather than the 3d analysis by Faber and Evans [89]. In the 2d analysis there is a contribution to toughening from crack front tilting and twisting, as opposed to the 3d model which shows most of the toughening should occur from twisting alone. Therefore, the toughness increase seen in hot pressing studies may not be the sole result of higher densities, but a result of whisker geometry.

Results of SiC_w reinforcement should also be compared to *in situ* reinforced Si_3N_4. As discussed above, Si_3N_4 shows evidence of all the major toughening mechanisms without the addition of a second phase. By optimizing beta-grain size and aspect ratio, Lange et al.

[55] showed fracture toughnesses of monolithic Si_3N_4 could be substantially improved. Current studies report toughnesses in the range of 8-11 $MPam^{1/2}$ [48, 91]. Which are of the same order as Si_3N_4 reinforced with SiC_w.

SEM Analysis of Fracture

SEM analysis can be used to characterize grain size as well as the degree of toughening from the microstructure and microstructural homogeneity. Ball-milled Si_3N_4 processed at pH 11 shows increased porosity with whisker loading (Figures 53 - 55). High levels of porosity are seen on 20 $^v/_o$ as-received SiC_w reinforced specimens. This surface shows little toughening with fracture occurring either transgranularly, or by a thick continuous glassy phase. Porosity is reduced by adding SiC_w before milling and toughening from the microstructure can be seen to substantially increase (Figures 56 - 57). When 10 $^v/_o$ SiC_w is added, the porosity and toughening differences due to ball-milling are not as obvious on the fracture surface. Both appear tough with little porosity, however, monolithic ball-milled Si_3N_4 also reveals a tough microstructure with virtually no porosity. Average grain size appears to decrease with added SiC_w, however, this difference is very slight. Green porosity had the most significant effect on grain size. Preferred grain growth is obvious in β-Si_3N_4 and all specimens exhibited this characteristic. β-Si_3N_4 grows to fill porosity and grain diameters of β-Si_3N_4 are substantially increased for grains growing into porosity as shown in Figure 58 a) and b). This abnormal grain growth is especially prevalent in ball-milled specimens processed at pH 3 (Figure 59 a) and b)). These pockets of larger grain size material may be due to large acicular pre-existing pores that were nearly filled by large precipitating β-Si_3N_4 grains. The pore structure for specimens produced

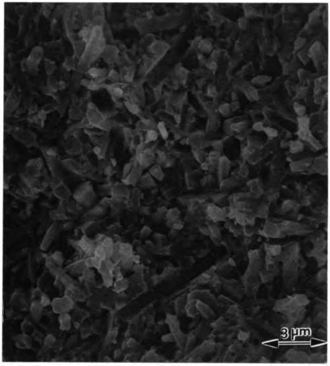

Figure 53 Fracture surface of monolithic ball-milled and ultrasonicated Si_3N_4 processed at pH 11.

Figure 54 Fracture surface of ball-milled and ultrasonicated Si_3N_4 with 10 $^v/_o SiC_w$ added after milling. Processed at pH 11.

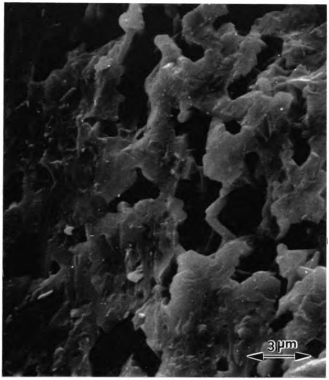

Figure 55 Fracture surface of ball-milled and ultrasonicated Si_3N_4 with 20 $^v/_o SiC_w$ added after milling. Processed at pH 11.

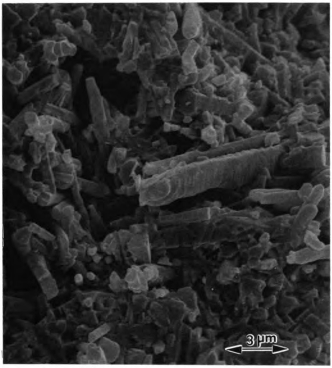

Figure 56 Fracture surface of 10 $^{v}/_{o}$ SiC_w reinforced Si_3N_4, all components ball-milled and ultrasonicated at pH 11.

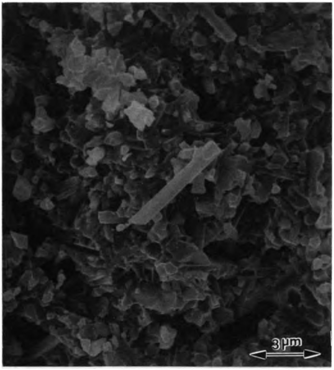

Figure 57 Fracture surface of 20 $^{v}/_{o}$ SiC_w reinforced Si_3N_4, all components ball-milled and ultrasonicated at pH 11.

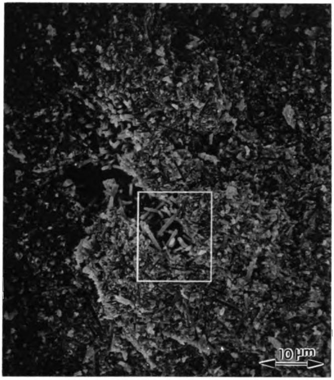

Figure 58a Image of typical porosity in sintered specimens. Shows elongated β-Si_3N_4 grains growing into and filling porosity.

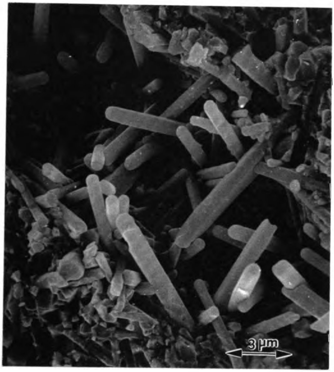

Figure 58b Insert showing irregular β-Si_3N_4 grain growth within the porosity.

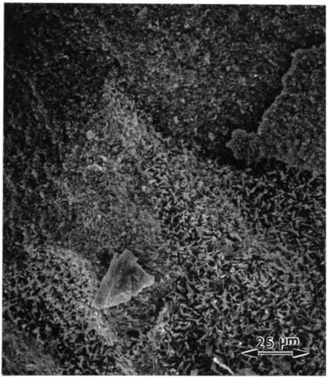

Figure 59a Micrograph showing a region of two distinct grain size regimes in monolithic Si_3N_4 processed and ball-milled at pH 3.

Figure 59b Higher magnification micrograph of the large grain size region. The morphology of β-Si_3N_4 appears much like that found in the porous regions of other sintered specimens.

from pH 3 ball-milled powders is unique to all the other specimens, as shown in Figure 60 a) and b). This is the only major difference between fracture surfaces as a function of pH. All specimens show evidence of glass rich regions and inhomogeneities regardless of processing history (Figure 61 a), b) and c).

It is extremely difficult to discern between β-Si_3N_4 and SiC_w on SEM fracture surfaces. Their diameters are similar, however, β-Si_3N_4 exhibits a hexagonal cross-section which is easy to identify when grains grow > 1μm (Figure 62). These larger grains are often associated with porous or glass rich areas in the microstructure as was demonstrated in Figure 58. Many toughening mechanisms are also evidenced on the fracture surfaces.

Monolithic and 10 $^v/_o$ reinforced materials show evidence of grain pull-out on their fracture surfaces. Pull-out seems to be more evident on monolithic specimens as opposed to whisker reinforced specimens. Areas of both crack bridging and crack deflection can be isolated on secondary cracks on the surface of both monolithic and composite fracture surfaces as was shown in Figure 51. These quantities can be more equivalently compared from indentation induced cracking however.

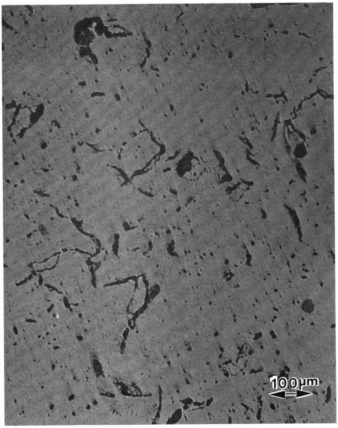

Figure 60a Changes in pore morphology with processing pH. Acicular pore morphology found in monolithic specimens ball-milled at pH 3.

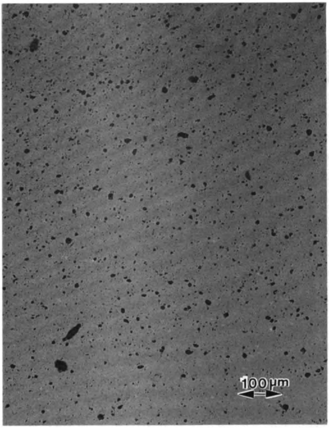

Figure 60b Typical pore morphology for all other processing conditions.

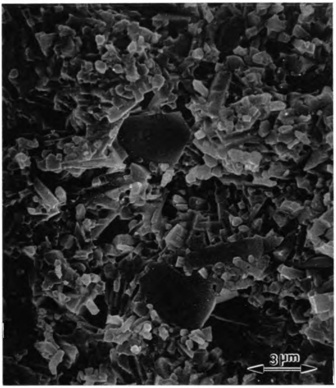

Figure 61a Figures a-c show regions of inhomogeneity found in specimens regardless of processing pH. a) shows either glass rich regions, or large β-Si_3N_4 grain cross-sections in a 10 ^{v}/o SiC_w specimen.

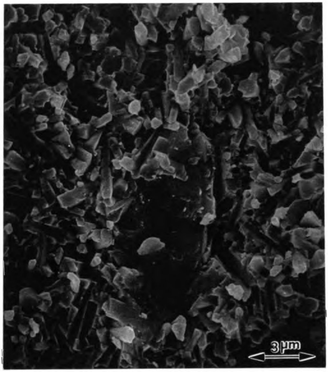

Figure 61b Shows glass rich-region in a monolithic specimen processed at pH 7.5. area.

Figure 61c Shows a large glass region associated with a large pore in a 10 $^{v}/_{o}$ SiC_w specimen.

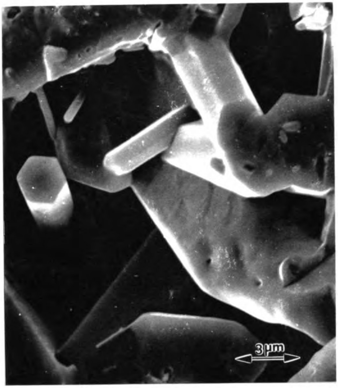

Figure 62 Micrograph showing large β-Si_3N_4 grains growing from a glass-rich region. The hexagonal morphology becomes more obvious as grains grow larger than 1 µm. The micrograph also evidences the growth of β-Si_3N_4 through the liquid phase as the β-Si_3N_4 grain appears to be precipitating out from a glass-rich

DISCUSSION

Green Processing of Si_3N_4/SiC_w Composites

The results of colloidal optimization are clearly demonstrated by sedimentation and Andreason pipette sizing of agglomerates. Agglomerate sizes are largest and sedimentation densities are lowest for pH 4-7 for Si_3N_4 and sedimentation densities are low for SiC_w for pH < 11 (Figures 10 - 11). It is interesting to note that these numbers match exactly the regions of homostability for Si_3N_4 and SiC_w as predicted by Suspension Stability© [10] and outlined in Figure 13. Stability predictions also correlate well with green density results for specimens pressed without sintering aids. Those pressed at pH 6, where Si_3N_4 and SiC_w are agglomerated, show the lowest green densities for monolithic and composite uni-axially pressed specimens. Monolithic specimens pressed from powders processed at pH 3 and 11, which showed the highest levels of stability, showed the highest green densities as well. This is due to removal of agglomeration and improved homogeneity of the suspension, which results in a freeze-dried powder with better pressing characteristics. Green densities are highest for composite powders produced at pH 11 because the enhanced stability of SiC whiskers provides fewer whisker agglomerates which impede green consolidation. From the above results, it's easy to see how applying colloidal stability theories (HHF/DLVO) can provide consistent, higher green densities. However, these theories apply to suspensions whose components are chemically inert with exception of the potential determining ions [1]. If components are soluble in the processing environment, such as Y_2O_3 in HNO_3 [105], the ability of these theories to predict suspension behavior begins to break down [101].

Reduction of agglomeration of colloidally produced ceramics can improve green homogeneity by reducing the number of flaws caused by deficient particle packing. Agglomeration can be reduced by manipulating particle charge to increase the double layer interaction between particles [1,99,104]. In order to do this, it's important to understand how changes in the suspension medium affect the surface of Si_3N_4.

The charges present on the Si_3N_4 are determined by the active chemical groups on the powder surface and how they change as aqueous suspension conditions change i.e.: changes in pH (H^+ and OH^- concentrations). Crimp [112] used infrared spectroscopy to characterize surface groups present on Ube SNE-10 Si_3N_4 powder. Results showed the presence of both silanol (acidic behavior) and amine groups (basic behavior). The i.e.p. of Si_3N_4 has been shown to decrease (or more closely resemble the behavior of SiO_2) as the surface O_2 content increases [7]. A silica rich surface layer is the result of thermodynamically unstable Si_3N_4 reacting with O_2 to form SiO_2.

$$Si_3N_4(s) + 3O_2(g) \Leftrightarrow 3SiO_2(s) + 2N_2(g)$$

Hackley et al. [101], however, reports a surface of hydrolyzed Si_3N_4 (Figure 63) comprised of acidic silanol and basic silazane (Si=NH). In aqueous solution, the silanol and silazane generate surface charge by adsorption of H^+ and OH^- which act as potential determining ions. In addition to the p.d.i.s, the surface of Si_3N_4 can react with hydrolysable metal

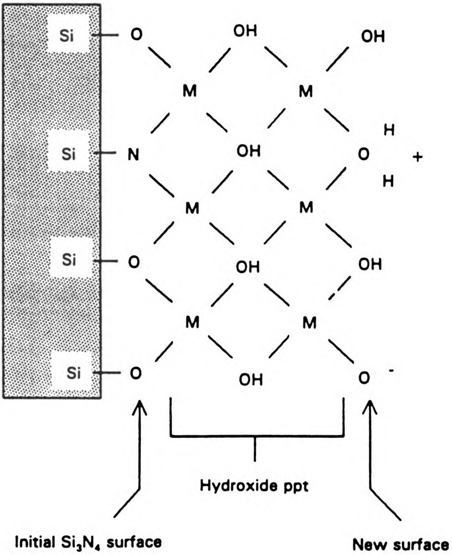

Figure 63 Schematic showing metal hydroxide interaction with the Si_3N_4-solution surface.

cations forming mono- and polynuclear complexes. Hackley suggests the following reactions my occur with metal ions such as Y^{3+} at pH < 9, the pK_a for $Si_2{=}NH_2^{+}$. At more alkaline pH, Si=NH may also

$$\equiv Si\text{-}OH + M^{Z+} \leftrightarrow \equiv Si\text{-}OM^{(Z-1)+} + H^{+}$$

or

$$2\equiv Si\text{-}OH + M^{Z+} \leftrightarrow (\equiv Si\text{-}O)_2\, M^{(Z-2)+} + 2H^{+}$$

become involved in complexation. Hackley simulates composite suspension conditions by electrokinetic titration of Si_3N_4 in the presence of $Y(NO_3)_3$ electrolyte. The surface of Si_3N_4 reacts with as little as 0.001M $Y(NO_3)_3$ at pH > 6 resulting in the precipitation of $Y(OH)_3$ on the surface of Si_3N_4. As precipitation continues, the electrokinetic behavior (ζ-potential) of Si_3N_4 changes to that of $Y(OH)_3$. While $Y(OH)_3$ appears a logical candidate for the precipitation that occurs during ball-milling at pH 7 and 11, it was not detected in the residue or in green ball-milled specimens. Green specimens were also checked for the presence of $Y(NO_3)_3$ revealing nothing. Therefore, while it is clear that Y_2O_3 is soluble in aqueous suspensions and especially in nitric acid solutions [101,105], it is still unclear what chemical complexes are being formed. Understanding the chemical state of the Y_2O_3, however, is important because it clearly has an effect on green density and may also have an effect on grain boundary phases in the sintered state.

Densification of SiC_w-Si_3N_4

Densities of fired specimens correlate well with composite green densities, showing decreased densification as whisker loading increases. The lowest composite sintered densities occurred at pH 7 despite the fact that the highest monolithic densities also occurred at pH 7 (Figure 34). This can be explained by examining what is happening to individual composite components at pH 7. First, SiC_w is agglomerated at pH 7 which will hamper liquid phase sintering and reduce final densities of the composite. It would also seem that because the Si_3N_4 matrix is also agglomerated at pH 7 that this should reduce sintered densities of the monolithic material. However, chemical effects during ball-milling may be hampering the densification of specimens produced at pH 3 and 11 more so than the agglomeration at pH 7. In order to see if the ball-milling residue had an adverse effect on densification, suspensions were milled and most of the skin that formed on top of the suspension was removed to lessen the relative amount in the freeze-dried powder. The effect this had on density, densification time, and fracture toughness is outlined in Figures 64 - 65. Specimens sintered more quickly and to higher densities when the ball-milling residue was reduced. However, fracture toughness decreased. While fracture toughness can be improved by reduction in flaw or porosity size and frequency, the K_{IC} of liquid phase sintered ceramics is highly dependent upon the interface between grains, both matrix /matrix, and matrix/whisker. Therefore, the fracture energy of the grain boundary phases present play a key role in the toughness properties of both monolithic and composite Si_3N_4.

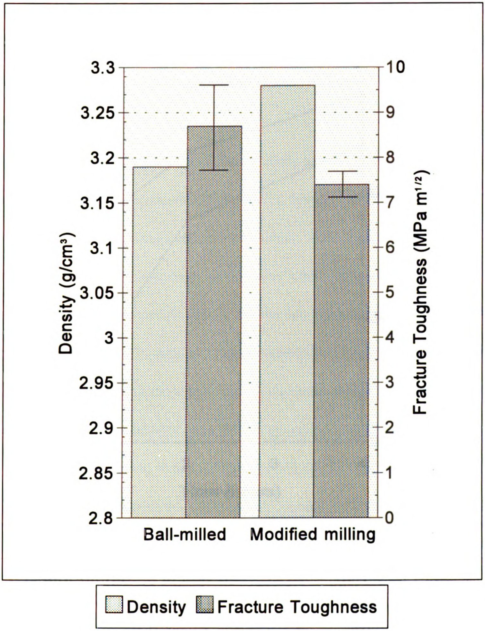

Figure 64 Comparison of density and fracture toughness for specimens freeze-dried with and without ball-milling skin.

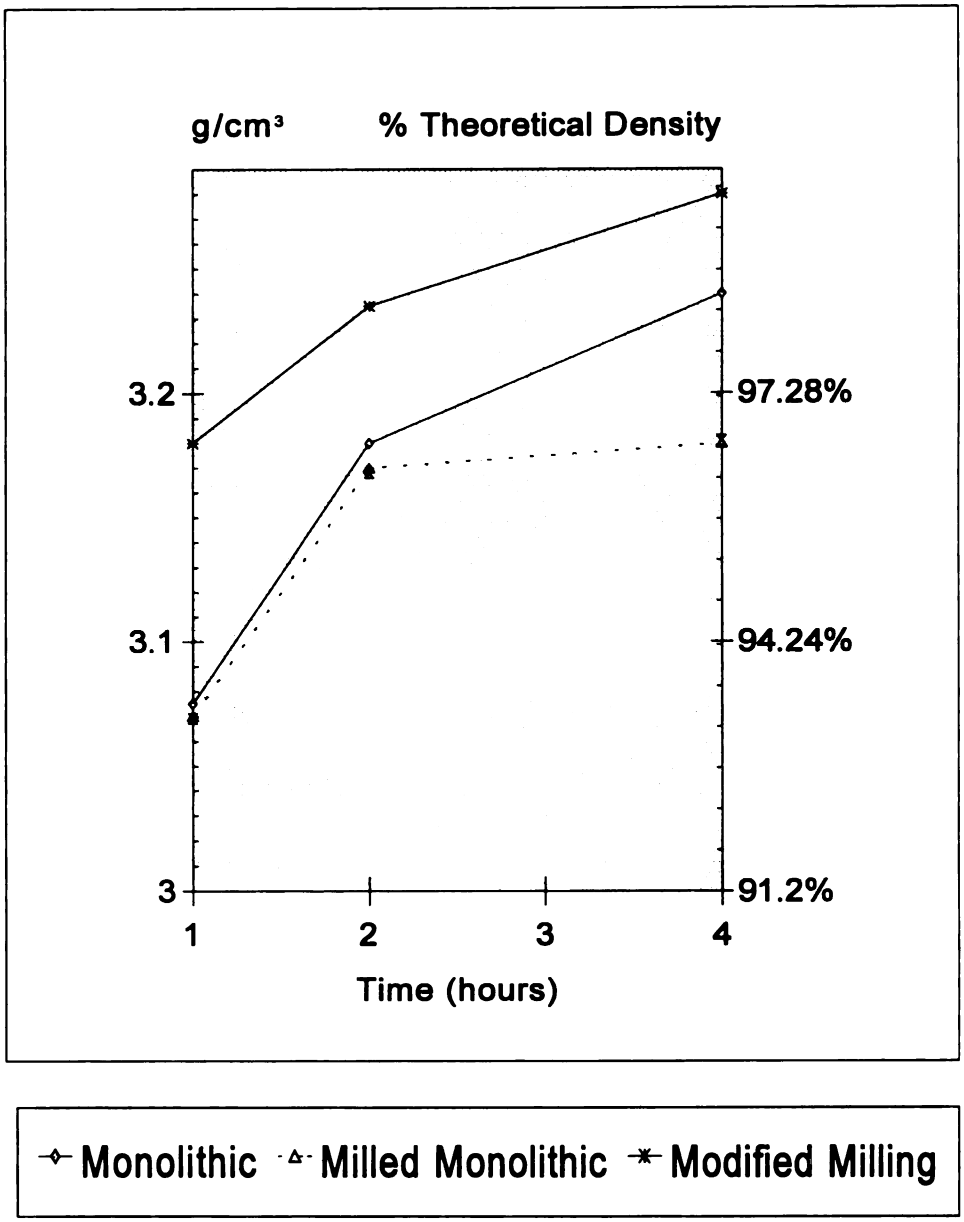

Figure 65 Comparison of densification with time for specimens freeze-dried with and without ball-milling skin. Standard deviation for each data point is too small to be seen clearly on the plot.

CONCLUSIONS

The suspension behavior of as-received Si_3N_4 and SiC_w powders can be accurately modeled using a modified version of DLVO/HHF theory [10] to predict the stability of both monolithic and composite suspensions. However, when hydrolysable metal ions are introduced into the suspension, such as the case when Y_2O_3 is added to suspensions, changes to the surface chemistry [101], and hence, surface charge of constituents in suspension become difficult to predict. As a consequence, green density no longer has a direct correlation with suspension stability. Y_2O_3 may react in suspension to produce currently uncharacterized compounds in the green state. Thus, hampering the ability to isolate the variables that most directly effect the sinterability and toughness of Si_3N_4 and SiC_w-Si_3N_4. HNO_3 acid solutions are capable of completely solutionizing Y_2O_3 during green processing, and basic solutions produce a residue during milling which hampers densification, but may produce a grain boundary phase that enhances fracture toughness. The addition of SiC_w to Si_3N_4 also has an effect on grain boundary phases. Compacts produced from powders at pH 11 with SiC_w produce crystalline $Y_2O_3 \bullet Si_3N_4$ which is not present in their monolithic counterparts.

Ball-milled Si_3N_4 specimens reinforced with 10% as-received (high aspect ratio) SiC_w produced the highest fracture toughness value of 9.1 $MPam^{1/2}$ slightly higher than monolithic Si_3N_4. However, both toughness values could be improved with larger grain size [65]. SEM analysis of fracture surfaces not only evidenced crack deflection, pull-out, and bridging for both monolithic and composite specimens, but shows wide spread inhomogeneities in specimens produced at all pH values (Figures #61 a-c). Finally, chemical reactions occurring during colloidal processing can impact the final properties of sintered compacts by affecting liquid formation during sintering, and adding to the already large number of parameters that must be taken into account when sintering any ceramic composite.

RECOMMENDATIONS

In order to gain more control over the final sintered microstructure, sintering aids could be added as Y-Al-Silicate glasses. Pre-prepared glasses (or crystalline phases such as YAG) could be made with varying composition and added to Si_3N_4 in a powder form. Materials prepared as sintering aids could also be mechanically tested to determine which compositions may have the greatest toughening effect, or perhaps the greatest high temperature strength. Colloidal processing and optimization could still be carried out with these sintering aids though ζ-potential testing and stability prediction. Solubility testing could also be carried out to determine the compositions most suitable for colloidal processing. In addition, changes in the sintering schedule could be made to vary the final grain size of both monolithic and composite specimens to evaluate further toughening.

BIBLIOGRAPHY

BIBLIOGRAPHY

1. Paul C. Hiemenz, Principles of colloid and Surface Chemistry, Marcel Dekker, New York, New York, 1986

2. E.M. Elimelech, "Kinetics of Capture of Colloidal Particles in Packed Beds Under Attractive Double Layer Interactions", *J. Col. Int. Sci.*, **[146]**, p.337, 1991.

3. E.M. Lifshitz, *Soviet Phys. JETP*, **[2]**, p. 73, 1956.

4. Alan Bleier, "Fundamentals of Preparing Suspensions of Silicon and Related Ceramic Powders", *J. Amer. Ceram. Soc.*, **[66]**, pp. C79-C81.

5. Duncan J. Shaw, Introduction to Colloid and Surface Chemistry, Butterworth-Heinemann, Oxford, 1992.

6. Michael James, Robert J. Hunter, and Richard W. O'Brien, "Effect of Particle Size Distribution and Aggregation on Electroacoustic Measurements of ζ Potential", *Langmuir*, **[8]**, pp. 420-23, 1992.

7. Egon Matijevic, "Colloid Science of Composite systems", Science of Ceramic Chemical Processing, Larry L. Hench and Donald R. Ulrich eds., pp. 463-81, John Wiley and Sons, New York 1986.

8. R.W. O'Brien, "Electro-Acoustic Effects in a Dilute suspension of Spherical Particles", *J. Fluid Mech.,* **[190]**, pp. 71-86, 1988.

9. M.J. Crimp, Masters Thesis, Case Western University, 1985.

10. B.A. Wilson and M.J. Crimp, "Prediction of Composite Colloidal Suspension Stability Based upon the Hogg, Healy, and Fuerstenau Interpretation", *Langmuir*, **[9]**, pp. 2836-43, 1993.

11. Derjaguin, *Kolloid-Z.*, **[69]**, p. 155, 1934; *Acta Physiochim.*, **[10]**, p. 333, 1939.

12. R. Hogg, T.W. Healy, and D.W. Fuerstenau, "Mutual Coagulation of Colloidal Dispersions",*Trans. Faraday Soc.*, **[62]**, pp. 1638-50, 1960.

13. Verwey and Overbeek, Theory of Lyophobic Colloids, Elsevier, New York, 1948.

14. Fuchs, *Z. Physik*, **[89]**, p. 736, 1934.

15. J.T.G. Overbeek, "Kinetics of Flocculation" in Colloid Science Volume I: Irreversible Systems, H.R. Kruyt Ed., pp. 278-301, Elsevier, New York, 1952.

16. M.W. Real, "Freeze Drying Alumina Powders", *Proc. Brit. Ceram. Soc.*, **[38]**, p. 59-66, 1986.

17. J.D. Mellor, Fundamentals of Freeze Drying, Academic Press, London, 1978.

18. Labconco Industry Service Publication, A Guide to Freeze Drying for the Laboratory, 1993.

19. P.E. Zovas, R.M. German, K.S. Hwang, and C.J. Li, "Activated and Liquid-Phase Sintering--Progress and Problems", *J. Metals*, **[35]**, p. 28-33, 1983.

20. W.D. Kingery, "Densification During Sintering in the Presence of a Liquid Phase. 1. Theory", *J. Appl. Phys.* **[30]**, p. 301-306, 1959.

21. R.M. German, Liquid Phase Sintering, Plenum press, New York and London, 1985.

22. W.D. Kingery, E. Niki, and M.D. Narasimhan, "Sintering of Oxide and Carbide-Metal Compositions in Presence of a Liquid Phase", *J. Amer. Ceram. Soc.*, **[44]**, p. 29-35, 1961.

23. W.D. Kingery and M.D. Narasimhan, "Densification During Sintering in the Presence of a Liquid Phase. 2. Experimental", *J. Appl. Phys.*, **[30]**, p. 307-310, 1959.

24. Yu. V. Naidich, I.A. Lavrinenko, and V.A. Evdokimov, "Densification During Liquid-Phase Sintering in Diamond-Metal Systems", *Soviet Powder Met. Metal Ceram.*, **[11]**, p.715-718, 1972.

25. V. Smolej, S. Pefovnik, and W.A. Kaysser, "Rearrangement During Liquid Phase Sintering of Large Particles", *Powder Met. Inter.*, **[14]**, p. 34-36, 1982.

26. W.J. Huppmann, W.A. Kaysser, D.N. Yoon, and G. Petzow,"Progress in Liquid Phase Sintering", *Powder Met. Inter.*,**[11]**, p. 50-51, 1979.

27. Duk N. Yoon and Winfried J. Huppmann, "Grain Growth and Densification During Liquid Phase Sintering of W-Ni", *Acta Met.*, **[27]**, p. 693-98, 1979.

28. G.H. Gessinger, H.F. Fischmeister, and H.L. Lukas, "A Model for Second-Stage Liquid-Phase Sintering with A Partially Wetting Liquid", *Acta Met.*, **[21]**, p. 715-24, 1973.

29. W.A. Kaysser, M. Zivkovic, and G. Petzow, "Shape accomodation during grain growth in the presence of a liquid phase", *J. of Mat. Sci.*, **[20]**, p. 578-84, 1985.

30. Rishi Raj, "Morphology and Stability of Glass Phase in Glass-Ceramic Systems", *J. Amer. Ceram. Soc.*, **[64]**, p. 245-48, 1981.

31. L.K.V. Lou, T.E. Mitchell, and A.H. Heuer, "Impurity Phases in Hot-Pressed Si_3N_4", *J. Amer. Ceram. Soc.*, **[61]**, p. 392-96, 1978.

32. T.H. Courtney, "Densification and Structural Development in Liquid Phase Sintering", *Met. Trans. A*, **[15A]**, p.1065-74, 1984.

33. Hyo-Hoon Park, Seong-Jai Cho, and Duk N. Yoon, "Pore Filling Process in Liquid Phase Sintering", *Met. Trans. A*, **[15A]**, p.1075-80, 1984.

34. H. Dean Batha and E. Dow Whitney, "Kinetics and Mechanism of the Thermal Decomposition of Si_3N_4", *J. Amer. Ceram. Soc.*, **[57]**, p. 365-69, 1973.

35. F.W. Dynys and J.W. Halloran, "Influence of Aggregates on Sintering", *J. Amer. Ceram. Soc.*, **[67]**, p. 596-601, 1984.

36. F.F. Lange, "Sinterability of Agglomerated Powders", *J. Amer. Ceram. Soc.*, **[67]**, p. 83-89, 1983.

37. S.S. Kang and D.N. Yoon, "Kinetics of Grain Coarsening During Sintering of Co-Cu and Fe-Cu Alloys wiht Low Liquid Contents", *Metall. Trans. A*, **[13A]**, p. 1405-11, 1982.

38. J. XinXiang and R. Taylor, "Dispersion of SiC Whiskers in SiC Whisker Reinforced Si_3N_4 Composite and Related Microstructural Characteristics", *Brit. Ceram. Trans.*, **[93]**, p. 11-15, 1994.

39. C.J. Shih, J.M. Yang, and A. Ezis, "Microstructure and Properties of Reaction-Bonded/Hot-Pressed SiC_w/Si_3N_4 Composites", *Composites Sci. and Tech.,* **[43]**, pp. 13-23, 1992.

40. W.H. Rhodes, "Agglomerate and Particle Size Effects on Sintering Yttria-Stabilized Zirconia", *J. Amer. Ceram. Soc.*, **[64]**, p. 19-22, 1981.

41. J.N. Brecker, "Analysis of Bond Formation in Vitrified Abrasive Wheels", *J. Amer. Ceram. Soc.*, **[57]**, p. 486-89, 1974.

42. G.M. Crosbie, J.M. Nicholson, and E.D. Stiles, "Sintering Factors for a Dry-Milled Silicon Nitride-Yttria-Alumina Compostion", *Ceram. Soc. Bull.*, **[68]**, p. 1202-06, 1989.

43. M. Kramer, "Rate-Controlled Sintering of Si_3N_4: Densification Kinetics and Microstructural Development", *J. Mat. Sci. Letters*, **[14]**, p. 778-80, 1995.

44. M.K. Cinibulk, G. Thomas, and S.M. Johnson, "Grain-Boundary-Phase Crystallization and Strength of Silicon Nitride with a YSiAlON Glass", *J. Amer. Ceram. Soc.*, **[73]**, p.1606-12, 1990.

45. G.R. Terwilliger and F.F. Lange, "Pressureless Sintering of Si_3N_4", *J. of Mat. Sci.*, **[10]**, p. 1169-74, 1975.

46. R.M. German and K.S. Churn, "Sintering Atmosphere Effects on the Ductility of W-Ni-Fe Heavy Metals", *Metall. Trans. A*, **[15A]**, p. 747-54, 1984.

47. C.J. Shih, J.M. Yang, and A. Ezis, "Microstructure and Properties of Reaction-Bonded/Hot-Pressed SiC_w/Si_3N_4 Composites", *Composites Sci. and Tech.*, **[43]**, pp. 13-23, 1992.

48. Murat Bengisu and Osman T. Inal, "Whisker Toughening of Ceramics: Toughening Mechanisms, Fabrication and Composite Properties", Annual Review of Materials Science, M.C. Flemmings, J.B. Watchman, Jr., E.N. Kaufmann, and J.A. Gioordmaine, Eds., **[24]**, p. 83-124, Annual Reviews Inc., Palo Alto, Ca., USA.

49. X.Y. Zheng, F.P. Zeng, M.J. Pomeroy, and S. Hampshire, "Reingorcement of Silicon Nitride Ceramics with Whiskers and Platelets", British Ceramic Proceedings Fabrication Technology, R.W. Davidge and D.P. Thompson Eds., **[45]** p. 187-98, The Institute of Ceramics Shelton, Stoke-on-Trent, Staffs. U.K., 1990.

50. S.T. Buljan, J.G. Baldoni, and M.L. Huckabee, "Si_3N_4-SiC Composites", *Am. Ceram. Soc. Bull.*, **[66]**, pp. 347-52, 1987.

51. H.F. Priest, G.L. Priest, and G.E. Gazza, "Sintering of Si_3N_4 Under High Nitrogen Pressure", *J. Amer. Ceram. Soc*, **[60]**, p. 81, 1977.

52. O. Abe, "Sintering Process of Y_2O_3 and Al_2O_3-doped Si_3N_4", *J. Mat. Sci.*, **[25]**, pp. 4018-26, 1990.

53. M. Mitomo, M. Tsutsumi, E. Bannai, and T. Tanaka, "Sintering of Si_3N_4", *Ceram. Soc. Bull.*, **[55]**, p. 313, 1976.

54. G.R. Terwilliger, “Properties of Sintered Si_3N_4”, *J. Amer. Ceram. Soc.*, **[57]**, p. 48-49, 1973.

55. F.F. Lange, "Fabrication and Properties of Dense Polyphase Silicon Nitride", *Ceram. Soc. Bull.*, **[63]**, p.1369-74, 1983.

56. G.E. Gazza, "Hot-Pressed Si_3N_4", *J. Amer. Ceram. Soc.*, **[56]**, p. 662, 1973.

57. C. Greskovich and C. O’Clair, “Effect of Impurities on Sintering Si_3N_4 Containing MgO or Y_2O_3 Additives”, *Ceram. Soc. Bull.*, **[57]**, p. 1055-56, 1978.

58. K. Ueno, S. Sodeoka, and J. Hirooka, “Influence of Sintering Conditions on the Mechanical Properties of SiC Whisker/Si_3N_4 Ceramic Composite”,*Journal of Ceramic Society of Japan, Int. Ed.,* **[100]**, p. 525-29, 1992.

59. R.E. Loehman and D.J. Rowcliffe, "Sintering of Si_3N_4-Y_2O_3-Al_2O_3", *J. Amer. Ceram. Soc.*, **[63]**, p. 144-48, 1980.

60. G.Q. Weaver and J.W. Lucek, “Optimization of Hot-Pressed Si_3N_4-Y_2O_3 Materials”, *Ceram. Soc. Bull*, **[57]**, p. 1131-36, 1978.

61. M. Mitomo, “Thermodynamics, Phase Relations, and Sintering Aids of Si_3N_4”, Silicon Nitride, S. Somiya, M. Mitomo, and M. Yoshimura, Eds., p. 1-11, Elsevier Applied Science, New York, 1990.

62. K. Kato, Z. Inoue, K. Kijima, I. Kawada, H. Tanaka, and T. Yamane, “Structural Approach to the Problem of Oxygen Content in Alpha Silicon Nitride”, *J. Amer. Ceram. Soc.*, **[58]**, p. 90-91, 1975.

63. K. Ichikawa, “The Influence of Si_3N_4 Powder Characteristics on Sintering Behavior”, Silicon Nitride, S. Somiya, M. Mitomo, and M. Yoshimura, Eds., pp. 107-16, Elsevier Applied Science, New York, 1990.

64. G. Wotting and G. Ziegler, "Powder Characteristics and Sintering Behavior of Si_3N_4-Powders", *Powder Met. Int.*, **[18]**, no.1, p. 25-32, 1986.

65. A.J. Pyzik and D.F. Carroll, "Technology of Self-Reinforced Silicon Nitride", Annual Review of Materials Science, M.C. Flemmings, J.B. Watchman, Jr., E.N. Kaufmann, and J.A. Gioordmaine, Eds., **[24]**, p. 189-214, Annual Reviews Inc., Palo Alto, Ca., USA, 1995.

66. H. Liu, Karl-L. Weisskopf, and G. Petzow, "Crack Deflection Process for Hot-Pressed Whisker-Reinforced Ceramic Composites", *J. Amer. Ceram. Soc.*, **[72]**, p. 559-63, 1989.

67. D.B. Marshall and J.E. Ritter, "Reliability of Advanced Structural Ceramics and Ceramic Matrix Composites-A Review", *Am. Ceram. Soc. Bull.*, **[66]**, p. 309-17, 1987.

68. J.E. Weston, P.L. Pratt, and B.C.H. Steele, "Crystallization of Grain boundary Phases in Hot-Pressed Silicon Nitride Materials", *J. Mat. Sci.*, **[13]**, p. 2137-46, 1978.

69. A. Tsuge, K. Nishida and M. Komatsu, "Effect of Crystallizing the Grain-Boundary Glass Phase on the High-Temperature Strength of Hot-Pressed Si_3N_4 Containing Y_2O_3", *J. Amer. Ceram. Soc.*, **[58]**, p. 323-26, 1975.

71. R.E. Loehman, "Preparation and Properties of Yttrium-Silicon-Aluminum Oxynitride Glasses", *J. Amer. Ceram. Soc.*, **[62]**, p. 491-94, 1979.

72. R.K. Bordia, R. Raj, "Analysis of Sintering of a Composite with a Glass or Ceramic Matrix", *J. Amer. Ceram. Soc.*, **[69]**, p.C55-C58, 1986.

73. A.J. Whitehead, T.F. Page, and I. Higgins, "Degradation of SiC Whiskers at Elevated Temperatures", *Ceram. Eng. Sci. Proc.*, **[10]**, pp. 986-97, 1989.

74. P.D. Shalek, J.J. Petrovic, G.F. Hurley, and F.D. Gac, "Hot-Pressed SiC Whisker/ Si_3N_4 Matrix Composites", *Ceram. Soc. Bull.*, **[65]**, p. 351-56, 1986.

75. S.M. Smith, R.O. Scattergood, J.P. Singh, and K. Karasek, "Effect of Silica and Processing Environment on the Toughness of Al_2O_3 Composites", *J. Amer. Ceram. Soc.*, **[72]**, pp. 1252-55.

76. Stephen W. Freiman, "Brittle Fracture Behavior of Ceramics", *Ceram. Soc. Bull.*, **[67]**, p. 392-402, 1988.

77. G.R. Anstis, P. Chantikul, B.R. Lawn, and D.B. Marshall, "A Critical Evaluation of Indentation Techniques for Measuring Fracture Toughness: I, Direct Crack Measurements", *J. Amer. Ceram. Soc.*, **[64]**, p. 533-538, 1981.

78. S. Palmqvist, "Occurrence of Crack Formation During Vickers Indentation as a Measure of the Toughness of Hard Metals", *Arch. Eisenhuttenwes.*, **[33]**, p. 629-633, 1962.

79. A.G. Evans, Fracture Mechanics Applied to Brittle Materials, Ed. S.W. Freiman, ASTM Spec. Tech. Publ., **No. 678**, Philadelphia, pp. 112-35, 1979.

80. R.F. Cook and G.M. Pharr, "Direct Observation and Analysis of Indentation Cracking in Glasses and Ceramics", *J. Amer. Ceram. Soc.*, **[73]**,pp. 787-817, 1990.

81. M.S. Kaliszewski, G. Behrens, A.H. Heuer, M.C. Shaw, D.B. Marshall, G.W. Dransmann, R.W. Steinbrech, A.Pafares, F. Guiberteau, F.L. Cumbrera, and Arturo Dominguez-Rodriguez, "Indentation Studies on Y2O3-Stabilized ZrO2: I, Development of Indentation- Induced Cracks", *J. Amer. Ceram. Soc.*, **[77]**, p. 1185-93, 1994.

82. C. Olagnon, E. Bullock, and G. Fantozzi, "Properties of Sintered SiC Whisker-Reinforced Si_3N_4 Composites", *J. Euro. Ceram. Soc.*, **[7]** p. 265-73, 1991.

83. International Encyclopedia of Composites Vol. #1, Stuart M. Lee, Ed., VHC, New York, New York, 1990.

84. A.G. Evans, "Perspective on the Development of High-Toughness Ceramics", *J. Amer. Ceram. Soc.*, **[73]**, p. 187-206, 1990.

85. D.H. Carter and G.F. Hurley, "Crack Deflection as a Toughening Mechanism in SiC-Whisker-Reinforced $MoSi_2F$", *J. Amer. Ceram. Soc.*, **[70]**, p. C79-C81, 1987.

86. K.T. Faber and A.G. Evans, "Crack Deflection Processes-I. Theory & II. Experiment", *Acta Metall.*, **[31]**, p. 565-84, 1983.

87. G.H. Campbell, M. Ruhle, B.J. Dalgleish, and A.G. Evans, "Whisker Toughening: A Camparison Between Aluminum Oxide and Silicon Nitride Toughened with Silicon Carbide", *J. Amer. Ceram. Soc.*, **[73]**, p. 521-30, 1990.

88. A.G. Evans and Y. Fu, "Some Effects of Microcracks on the Mechanical Properties of Brittle Solids-II. Microcrack Toughening", *Acta Met.*, **[33]**, p. 1525-31, 1985.

89. A.G. Evans and K.T. Faber, "Crack-Growth Resistance of Microcracking Brittle Materials", *J. Amer. Ceram. Soc.*, **[67]** p.255-60, 1984.

90. M.D. Thouless and A.G. Evans, "Effects of Pull-Out on the Mechanical Properties of Ceramic-Matrix Composites", *Acta Met.*, **[36]**, p. 517-22, 1988.

91. P. Sajgalik, J. Dusza, and M.J. Hoffmann, "Relationshop between Microstructure, Toughening Mechanisms, and Gracture Toughness of Reinforced Silicon Nitride Ceramics", *J. Amer. Ceram. Soc.*, **[78]** p. 2619-24, 1995.

92. P.F. Becher, E.R. Fuller Jr., and Peter Angelini, "Matrix-Grain-Bridging Contributions to the Toughness of Whisker-Reinforced Ceramics", *J. Amer. Ceram. Soc.*, **[74]**, p. 2131-35, 1991.

93. Paul F. Becher and George C. Wei, “Toughening Behavior in SiC-Whisker-Reinforced Alumina”, *J. Amer. Ceram. Soc.*, **[67]**, p. C267-C269, 1984.

94. P.F. Becher, Chun-Hway Hsueh, P. Angelini, and T.N. Tiegs, "Toughening Behavior in Whisker-Reinforced Ceramic Matrix Composites", *J. Amer. Ceram. Soc.*, **[71]**, p. 1050-61, 1988.

95. A.A. Morrone, S.R. Nutt, and S. Suresh, “Fracture Toughness and Fatigue Crack Growth behavior of an Al_2O_3-SiC Composite”, *J. Mat. Sci.*, **[23]**, pp. 3206-13, 1988.

96. J. Homeny, W.L. Vaughn, and M.K. Ferber, “Silicon Carbide Whisker/Alumina Matrix Composites: Effect of Whisker Surface Treatment on Fracture Toughness”, *J. Amer. Ceram. Soc.*, **[73]**, pp. 394-402, 1990.

97. Personal Communication with Brett Wilson

98. M.J. Crimp and R.F. Preston, “Evaluation of Sidimentation as a Technique for the Separation of Sub-Micron Diameter Silicon Carbide Whiskers”, British Ceramic Proceedings Fabrication Technology, R.W. Davidge and D.P. Thompson Eds., **[45]** p. 187-98, The Institute of Ceramics Shelton, Stoke-on-Trent, Staffs. U.K., 1990.

99. R.J. Hunter, Foundations in Colloid Science: Volume 1, Oxford University Press, Oxford, 1986.

100. Z. Yeh, P.R. Sneary, and M.J. Crimp, “Deagglomeration of Si_3N_4-SiC_w Colloidal Systems”, submitted to *J. Amer. Ceram. Soc*, May, 1996.

101. V.A. Hackley and S.G. Malghan, “The Surface Chemistry of Silicon Nitride Powder in the Presence of Dissolved Ions”, *J. Mat. Sci.*, **[29]**, pp. 4420-30, 1994.

102. ASTM C 373-88, “Strandard Test Method for Water Adsorption, Bulk Density, Apparent Porosity, and Apparent Specific Gravity of Fired Whiteware Products”, 1988.

103. C.P. Gazzara and D.R. Messier, “Determination of Phase content of Si_3N_4 by X-Ray Diffraction Analysis”, *Amer. Ceram. Soc. Bull.*, **[56]**, pp. 777-80, 1977.

104. Robert J. Hunter, Zeta Potential in Colloid Science, Academic Press, London, 1981.

105. William R. Linke, Solubilities of Inorganic and Metal-Organic Compounds: K-Z, American Chemical Society, Washington, D.C., 1965.

106. M. Yang and R. Stevens, "Fabrication of SiC Whisker Reinforced Al_2O_3 Composites", *J. Mat. Sci.*, **[25]**, pp. 4658-66, 1990.

107. Robert R. Thompson, "Mechanics of Powder Pressing: II, Finite-Element Analysis of End-Capping in Pressed Green Powders", *Amer. Ceram. Soc. Bull.*, **[60]**, pp. 244-51, 1981.

108. P.D. Shalek, J.J. Petrovic, G.F. Hurley, and F.D. Gac, "Hot-Pressed SiC Whisker/Si_3N_4 Matrix Composites", *Amer. Ceram. Soc. Bull.*, **[65]**, pp. 351-56, 1986.

109. S.T.J. Chen and J.M. Yang, "Quantitative Determination of the Stability of SiC Whisker in Reaction-Bonded/Hot Pressed Si_3N_4 Composites by X-Ray Diffraction", *J. Mat. Sci.*, **[27]**, pp. 5123-32, 1992.

110. A.W.J.M. Rae, D.P. Thompson, and K.H. Jack, "The Role of Additives in the Densification of Nitrogen Ceramics", in Ceramics For High Performance Applications-II, John J. Burke, Edward N. Lenoe, and R. Nathan Katz, Eds., pp. 1039-67, Brook Hill Publishing Co., Chestnut Hill, Mass., 1978.

111. C.J. Shih, J.M. Yang, and A. Ezis, "Processing of SiC Whisker-Reinforced Si_3N_4 Composites", *Ceram. Eng. Sci. Proc.*, **[10]**, pp. 1064-71, 1989.

112. Byong-Taek Lee and K. Hiraga, "Microstructure and Micro-Indentation Fracture of SiC-Whisker-Reinforced Si_3N_4 Composite Studied by High-Resolution Electron Microscopy", *Materials Transactions, JIM*, **[34]**, pp. 930-36, 1993.